

AN ABSTRACT OF THE DISSERTATION OF

Abdollah T. Farsoni for the degree of Doctor of Philosophy in Radiation Health Physics presented on December 1, 2006.

Title: Simultaneous Beta/Gamma Digital Spectroscopy.

Abstract approved:

David M. Hamby

A state-of-the-art radiation detection system for simultaneous spectroscopy of beta-particles and gamma-rays has been developed. The system utilizes a triple-layer phoswich detector and a customized Digital Pulse Processor (DPP) built in our laboratory. The DPP board was designed to digitally capture the analog signal pulses and, following several digital preprocessing steps, transfer valid pulses to the host computer for further digital processing. A MATLAB algorithm was developed to digitally discriminate beta and gamma events and reconstruct separate beta and gamma-ray energy spectra with minimum crosstalk. The spectrometer proved to be an effective tool for recording separate beta and gamma-ray spectra from mixed radiation fields. The system as a beta-gamma spectrometer will have broad-ranging applications in nuclear non-proliferation, radioactive waste management, worker safety, systems reliability, dose assessment, and risk analysis.

©Copyright by Abdollah T. Farsoni
December 1, 2006
All Rights Reserved

SIMULTANEOUS BETA/GAMMA DIGITAL SPECTROSCOPY

by
Abdollah T. Farsoni

A DISSERTATION

submitted to

Oregon State University

in partial fulfillment of
the requirements for the
degree of

Doctor of Philosophy

Presented December 1, 2006
Commencement June 2007

Doctor of Philosophy dissertation of Abdollah T. Farsoni

presented on December 1, 2006.

APPROVED:

Major Professor, representing Radiation Health Physics

Head of the Department of Nuclear Engineering and Radiation Health Physics

Dean of the Graduate School

I understand that my dissertation will become part of the permanent collection of Oregon State University libraries. My signature below authorizes release of my dissertation to any reader upon request.

Abdollah T. Farsoni, Author

DEDICATION

This dissertation is dedicated to the memory of my grandparents,
Masoumeh and Abdol Ali Dalvand.

ACKNOWLEDGEMENTS

This research was made possible through a U. S. Department of Energy (NEER) grant. The author is grateful for the opportunity made possible by this grant.

I am particularly aware of the invaluable personal support of my wife, Zahra. I like to express my appreciation, for believing in and encouraging me during the difficult times; for patiently enduring long hours spent at the lab; and for being my constant companion during the PhD process. I also owe a great debt of thanks to my parents Homa and Mohammad for their determination to provide me with a good education.

My deepest gratitude is to my advisor, Dr. David Hamby. I have been remarkably fortunate to have an advisor who gave me the freedom to explore on my own and at the same time the guidance to recover when my steps faltered. He taught me how to question thoughts and express ideas. His patience and full support helped me overcome many problems and finish this dissertation. I hope that one day I would become as good an advisor to my students as Dr. Hamby has been to me. I am also very grateful for having an exceptional doctoral committee and wish to thank Dr. K. Higley, Dr. T. Palmer, Dr. L. Lucchese and Dr. H. Jansen for their continual support and encouragement.

TABLE OF CONTENTS

	<u>Page</u>
1 Introduction.....	1
1.1 Overview.....	1
1.2 Goals and Objectives.....	3
1.3 Applications and Significance.....	5
2 Review of the Literature.....	7
2.1 Beta Particle Sources and Interactions.....	7
2.1.1 Beta Particle Sources.....	7
2.1.2 Interaction of Beta Particle with Matter.....	9
2.2 Gamma-ray Sources and Interactions.....	13
2.2.1 Gamma-Ray Sources.....	13
2.2.2 Interaction of Gamma-Rays with Matter.....	14
2.3 Scintillation Detector Principles.....	18
2.3.1 Scintillation Theory.....	18
2.3.2 Scintillation Detectors.....	20
2.3.3 Scintillation Pulse-Shape Analysis.....	22
2.4 Phoswich Detectors.....	24
2.4.1 Radiation Detection Using Phoswich Detectors.....	25
2.4.2 Methods For Pulse Shape Discrimination.....	29
2.5 Classical and Digital Spectroscopy.....	31

TABLE OF CONTENTS (Continued)

	<u>Page</u>
3 Materials and Methods.....	34
3.1 Triple-Layer Phoswich Detector.....	34
3.1.1 Design and Materials.....	34
3.1.2 MCNP Study and Simulations.....	38
3.2 Data Acquisition System.....	44
3.2.1 Digital Pulse Processor.....	44
3.2.2 Analog Circuitry.....	47
3.2.3 Digital Circuitry.....	50
3.3 MATLAB Algorithm.....	61
4 Results.....	65
4.1 Measurements Using a Digital Oscilloscope.....	65
4.2 Measurements Using the Digital Pulse Processor.....	71
4.2.1 Determination of FR_Th and SR_Th.....	71
4.2.2 Energy Calibration.....	77
4.2.3 Beta and Gamma-Ray Spectroscopy.....	82
5 Discussion.....	91
5.1 Simultaneous Spectroscopy.....	91
5.1.1 Gamma Response.....	91
5.1.2 Beta Response.....	92
5.1.3 Mixed Gamma/Beta Field.....	94

TABLE OF CONTENTS (Continued)

	<u>Page</u>
5.2 Study of Factors Affecting the Results.....	95
5.2.1 Phoswich Detector Design and Configuration.....	95
5.2.2 Digital Pulse Processor.....	98
5.2.3 Resolving Algorithm.....	99
5.2.4 Background Radiation.....	101
6 Conclusions.....	102
6.1 System Performance.....	102
6.2 Future Work.....	104
Bibliography.....	107
Appendices.....	114
Appendix A MCNP input file for Modeling Photon Transport.....	114
Appendix B MATLAB Algorithm.....	116

LIST OF FIGURES

<u>Figure</u>	<u>Page</u>
1.1 Two steps for measuring beta spectra in a mixed beta/gamma field.....	1
2.1 Decay scheme of ^{14}C to its transformation product ^{14}N (taken from Martin 2000).....	8
2.2 Continuous spectrum of beta particle emission from ^{14}C (taken from Martin 2000).....	8
2.3 Transformation of ^{60}Co and ^{137}Cs to stable nuclides by beta decay and their immediate gamma-ray emissions (taken from Martin2000).....	14
2.4 The relative importance of the three major types of gamma-ray interaction (taken from Evans 1955).....	15
2.5 Recoil electron and scattered photon from Compton scattering (taken from Knoll 2000).....	16
2.6 Pair production interaction (taken from Martin 2000).....	17
2.7 Simplified schematic of a scintillation detector.....	20
2.8 Basic elements of a Photomultiplier Tube (PMT) (taken from Knoll 2000).....	21
2.9 Voltage pulse for the two extremes of large and small anode time constant (modified from Knoll 2000).....	23
2.10 A phoswich detector designed by Usuda (1997) for simultaneous counting of alpha, beta (gamma), thermal and fast neutrons.....	26
2.11 The rise-time distribution measurement for discrimination of different radiation types(Usuda et al. 1997).....	26
2.12 The rise-time measurement using traditional laboratory modules.....	30
2.13 The architecture of (a) classical and (b) digital spectrometers (taken from Simoes et al. 1999).....	32

LIST OF FIGURES (Continued)

<u>Figure</u>	<u>Page</u>
3.1 Schematic arrangement of the phoswich detector.....	36
3.2 Phoswich detector schematic sketch provided by Saint-Gobain.....	36
3.3 Triple-Layer phoswich detector constructed by Saint-Gobain.....	37
3.4 Simulated detector response from 1.0 MeV gamma-ray in all three Scintillation layers.....	39
3.5 Simulated detector response from (a) 0.1 MeV (b) 0.5 MeV (c) 1.0 MeV and (d) 2.0 MeV monoenergetic electrons in Mylar, BC400 and CaF ₂ :Eu layers.....	40
3.6 Simulated detector response from different monoenergetic electrons in BC400.....	41
3.7 A typical anode pulse from: (a) beta absorption in both BC-400 (fast component) and CaF ₂ (Eu) (slow component), and (b) gamma absorption in NaI(Tl).....	43
3.8 A simplified block diagram of the data acquisition system including the Digital Pulse Processor unit, host PC and the MATLAB software.....	45
3.9 Schematic of the preamplifier, Nyquist filter and differential ADC driver.....	48
3.10 Preamplifier and Nyquist filter assembled on a small daughter board.....	49
3.11 A simplified schematic of the digital circuitry.....	51
3.12 Solder Mount boards were used to solder and assemble digital and analog parts on the mother board.....	53
3.13 DPP mother board, XEM3001 and preamplifier.....	54
3.14 Block diagram of XEM3001.....	56

LIST OF FIGURES (Continued)

<u>Figure</u>	<u>Page</u>
3.15 ISE 8.1i Webpack for the FPGA design and programming.....	59
3.16 FPGA behavioral simulation using ISE 8.1i Webpack.....	60
3.17 Four parameters, Baseline, P, M1 and M2 used for analyzing the anode pulses.....	62
3.18 Sums A and B used for calculating the energy absorption in each layer of the phoswich detector.....	62
3.19 The algorithm developed to collect separate gamma and beta energy-deposition spectra.....	64
4.1 Fast Ratio (FR) distribution from four beta and gamma sources.....	66
4.2 Fall Time (FT) distribution from (a) ^{60}Co and (b) ^{137}Cs gamma sources...	67
4.3 Percentage of events when the detector was exposed separately to (a) shielded gamma ^{137}Cs (b) pure beta ^{14}C and (c) $^{90}\text{Sr}/^{90}\text{Y}$ sources.....	68
4.4 Simultaneous beta (a) and gamma (b) energy spectra from 15,000 anode pulses when the detector was exposed to both $^{90}\text{Sr}/^{90}\text{Y}$ and ^{137}Cs sources.....	70
4.5 (a) Fast and (b) Slow Ratio distributions from ^{137}Cs shielded gamma-ray source.....	72
4.6 (a) Fast and (b) Slow Ratio distributions from ^{60}Co shielded gamma-ray source.....	73
4.7 (a) Fast and (b) Slow Ratio distributions from ^{14}C pure beta particle source.....	74
4.8 (a) Fast and (b) Slow Ratio distributions from ^{36}Cl pure beta particle source.....	75

LIST OF FIGURES (Continued)

<u>Figure</u>	<u>Page</u>
4.9 Beta particles (E_{\max}) from (a) ^{14}C and (b) ^{99}Tc were used for BC400 calibration.....	77
4.10 The Compton edge and photopeak of ^{137}Cs were used for $\text{CaF}_2\text{:Eu}$ calibration.....	79
4.11 The 662 keV and 1332 keV photopeaks, respectively from ^{137}Cs and ^{60}Co , were used for NaI(Tl) calibration.....	81
4.12 (a) percentage of events and (b) simultaneous beta and gamma-ray energy deposition spectra from shielded ^{137}Cs gamma source.....	84
4.13 (a) percentage of events and (b) simultaneous beta and gamma-ray energy deposition spectra from shielded ^{60}Co gamma source.....	85
4.14 (a) percentage of events and (b) simultaneous beta and gamma-ray energy deposition spectra from ^{14}C , a pure beta emitter.....	86
4.15 (a) percentage of events and (b) simultaneous beta and gamma-ray energy deposition spectra from ^{99}Tc , a pure beta emitter.....	87
4.16 (a) percentage of events and (b) simultaneous beta and gamma-ray energy deposition spectra from $^{90}\text{Sr}/^{90}\text{Y}$, a pure beta emitter.....	88
4.17 Simultaneous beta and gamma-ray energy deposition spectra from ^{14}C and shielded ^{137}Cs	89
4.18 Simultaneous beta and gamma-ray energy deposition spectra from ^{99}Tc and shielded ^{60}Co	89
4.19 Simultaneous beta and gamma-ray energy deposition spectra from $^{90}\text{Sr}/^{90}\text{Y}$ and shielded ^{137}Cs	90

LIST OF TABLES

<u>Table</u>	<u>Page</u>
3.1 Physical properties for the scintillators used in the phoswich detector.....	34
3.2 Pulse acceptance/rejection criteria calculated using MCNP simulation.....	43

SIMULTANEOUS BETA/GAMMA DIGITAL SPECTROSCOPY

1 Introduction

1.1 Overview

Generally, spectrometers developed to measure beta-particle energy distributions possess an inherent sensitivity to gamma-ray interactions that result in distortions of the measured distributions (Simons et al. 1990). The design of a beta spectrometer depends largely on the measuring task (Vasil'ev et al. 1996, Usuda et al. 1992a, Mangun Panitra et al. 2001); if a beta spectrum is to be measured in a mixed beta/gamma field, a separation of the beta energy from that of the gamma rays has to be carried out (Hajnal et al. 1986).

In an attempt to minimize this distortion, a general technique of data collection has evolved over the years whereby two separate energy distributions are measured (Fig. 1.1) for each mixed beta/gamma source (ICRU Report 56/1997, Martz et al. 1986).

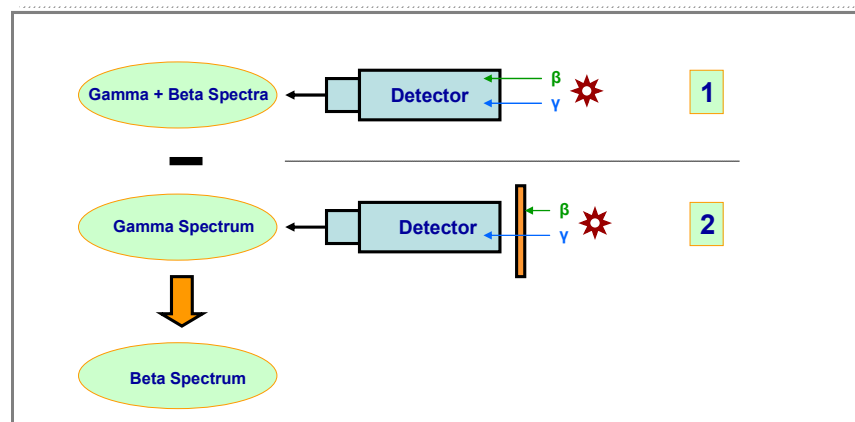


Fig. 1.1: Two steps for measuring beta spectra in a mixed beta/gamma field.

The first measurement provides the spectrometer “open window” response to both beta particles and gamma rays. A filter, of sufficient thickness to stop incident beta particles, is then placed around the spectrometer and the gamma-ray response is measured. The incident beta-particle energy distribution is determined by stripping the second measured distribution from the first. The disadvantages of this method are that the ambient gamma-ray field must remain constant during the measurement of the two distributions, the method doubles the time required to collect data, and instabilities in the spectrometer can lead to discrepancies between the gamma-ray-induced pulse-height distributions.

In the same way, a gamma detector is not immune to the beta interferences or “crosstalk” when the detector is exposed to a mixed beta/gamma field. Although gamma-rays and beta particles undergo different mechanisms to release their energies in matter, the gamma-ray energy will be absorbed in the form of energetic electrons. Because of this similarity, difficulties arise in attempting to separate energy deposition events originating from beta or gamma interactions.

To address these problems and based on previous measurements and MCNP analyses of a prototypic phoswich detector (Farsoni and Hamby 2005), a triple-layer phoswich detector has been modeled, designed and constructed. The phoswich detector, in conjunction with a customized Digital Pulse Processor (DPP), will be able to simultaneously record beta and gamma energy spectra with minimal crosstalk.

As part of this research, the DPP unit has been designed and constructed using a fast Analog-to-Digital Converter (ADC) with a 100 MHz sampling rate and 12-bit resolution. A MATLAB¹ algorithm has been developed to control the DPP and also separate beta/gamma induced pulses. The algorithm also generates two separate energy spectra, one for gamma and one for beta. All communications such as control commands and data transfers between MATLAB and the DPP board are performed via a high-speed USB (2.0) port. Digital and logic functions such as trigger control, over-range and pile-up rejection, and also the circular buffer are implemented in a Field Programmable Gate Array (FPGA). The FPGA configuration code has been developed in our laboratory using the high-level language VHDL (Very-high-speed integrated circuit Hardware Descriptive Language). All the FPGA design processes such as behavior simulations, synthesis, implementation and generation of the FPGA configuration file were executed using the ISE 8.1i design tools from Xilinx Inc².

1.2 Goals and Objectives

The objective of this work is to design and construct a complete detection system for simultaneous gamma and beta spectroscopy with minimal interference. The system will utilize a triple-layer phoswich detector, a dedicated digital pulse

¹ The MathWorks, Inc. 3 Apple Hill Drive Natick, MA 01760-2098.

² Xilinx, Inc. 21100 Logic Drive, San Jose, CA 95124.

processor (DPP) and its appropriate data acquisition software, algorithms and firmware codes.

Certain layers of the phoswich detector will be assigned for detection of each radiation type. The phoswich configuration and geometry will be designed to accommodate radiations from common beta and gamma sources. The Monte Carlo N-Particle (MCNP) code will be used to simulate energy deposition from gamma-rays and monoenergetic electrons in each layer of the phoswich detector. The MCNP results will provide the criteria for accepting or rejecting a radiation pulse via the MATLAB algorithm.

Classical and analog spectroscopy systems are not capable of analyzing fast anode pulses from this type of detector; therefore, a customized digital pulse processor will be designed and constructed. The sampling rate and resolution of this system will be chosen to meet the dynamic range and timing profile of the detector output pulses. Separating beta and gamma events, and collecting beta and gamma energy spectra, will be performed using an algorithm developed in the MATLAB environment. This algorithm also controls the DPP unit.

And finally, to evaluate how well the algorithm separates gamma and beta events, the phoswich detector will be exposed on separate occasions to beta particle, gamma-ray and mixed beta/gamma sources.

1.3 Applications and Significance

By utilizing the phoswich technology, many researchers have been involved in developing detection systems, capable of discriminating radiation types (Usuda et al. 1992, 1994 and 1997, Takada et al. 1996, Hsu et al. 1998, Childress et al. 2002, Bardelli et al. 2002, Ely et al. 2005 and Hennig et al. 2006).

In a phoswich detector, two or three scintillation layers are optically coupled to a single photomultiplier and, by analyzing the anode pulse shape, it can be determined in which layer the radiation interaction has occurred.

Two important features can be identified for a useful multi-radiation spectrometer system:

1. efficiently discriminating among different radiation types, and
2. reconstructing the spectral information for each radiation type with minimal crosstalk and reasonable energy resolution.

Usuda et al. (1997) developed a phoswich detector for simultaneous counting of alpha, beta and gamma rays. The separation of pulses induced from different radiation types was carried out by using the rise time measurement technique. However, a difficulty arises in the separation between beta and gamma rays because of the similarity of radiation interactions within the scintillators. Childress et al. (2002) also developed a triple crystal phoswich detector for simultaneous detection of alpha, beta and gamma radiation. In this design, a CaF₂:Eu crystal was used for both gamma and beta interactions but the problem of gamma/beta mischaracterization was left unsolved.

In both designs above, the beta/gamma-sensitive layer of the detector is not optimized for beta spectroscopy. This leads to partial beta energy absorption and the loss of spectroscopic information necessary for reconstructing a useful beta spectrum.

In the current research, however, a triple-layer phoswich detector is developed to minimize spectroscopic interferences. Since gamma and beta radiations from a mixed source can be simultaneously detected and measured, the radionuclide identification task may be more easily accomplished when two useful signatures, gamma and beta energy spectra, are used. The detection system as a general purpose simultaneous beta/gamma spectrometer will have broad-ranging applications in radioactive waste management, worker safety, systems reliability, dose assessment, and risk analysis.

Moreover, by some modification of the FPGA code and assigning memory locations to store the energy histogram data (energy spectra) on board, the DPP system can be converted to a general purpose digital spectrometer. This will provide a useful tool for future research in which digital pulse processing of radiation signal pulses are required.

2 Review of the Literature

2.1 Beta Particle Sources and Interactions

2.1.1 Beta Particle Sources

Nuclei having an excess of neutrons tend to emit an electron, i.e. beta particle, thus leaving the nucleus with one less neutron and one more proton. Conversely, nuclei with excess protons usually emit a positron. In either case, the total number of nucleons remains constant. Beta emission leaves many nuclei in an excited state, and one or more gamma-rays are then emitted to reach the ground state (Attix 1986).

For beta emission to be energetically possible, the exact nuclear mass of the parent must be greater than the sum of the exact masses of the daughter nucleus plus the beta particle:

$$M_p = M_d + M_e + Q \quad [2.1]$$

where the Q-value represents the energy balance.

Because a unit negative charge is lost during beta decay and the mass of the beta particle is very much less than 1 atomic mass unit, the daughter nucleus is one atomic number higher than its parent, but retains the same atomic mass number as the parent.

For example, the transformation of ^{14}C by beta-particle emission can be shown by the reaction equation:



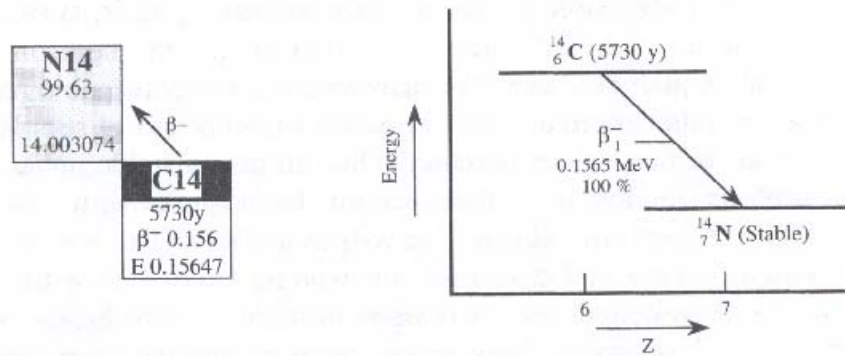


Fig. 2.1: Decay scheme of ^{14}C to its transformation product ^{14}N (taken from Martin 2000).

where $\bar{\nu}$ represents the *antineutrino*. The decay scheme of this transformation is shown in Fig. 2.1. The Q-value is 0.156 MeV and is positive, which is required for the reaction to be spontaneous. This energy is distributed between the recoiling product nucleus (negligible), the ejected electron and the antineutrino (Martin 2000). Beta particles are emitted with a range of energies from just above zero to the maximum energy (E_{max}). The beta particle energy spectrum from ^{14}C is depicted in Fig. 2.2.

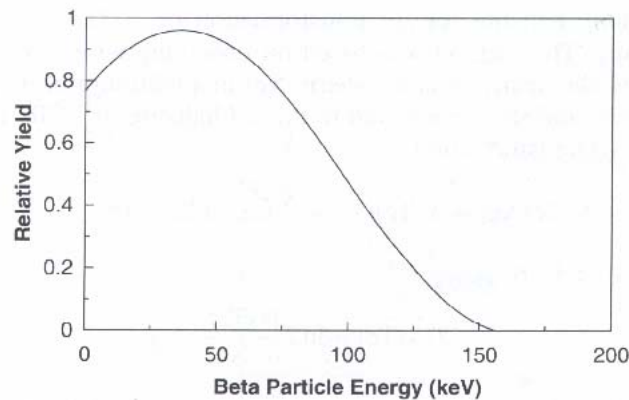


Fig. 2.2: Continuous spectrum of beta particle emission from ^{14}C (taken from Martin 2000).

The fact that beta radiation is emitted with a continuous energy distribution up to a definite maximum seems to violate the established energy-mass conservation laws. To prevent violation of the conservation laws, it was postulated that the beta particle is accompanied by another particle, called an *antineutrino*, whose energy is equal to the difference between the kinetic energy of the accompanying beta particle and the maximum energy of the spectral distribution.

2.1.2 Interaction of Beta Particles With Matter

Upon entering any absorbing medium, a charged particle immediately interacts simultaneously with many electrons. In any one such encounter, the electron experiences an impulse from the attractive Coulomb force as the particle passes its vicinity. Depending on the proximity of the encounter, this impulse may be sufficient either to raise the electron to a higher-lying shell within the absorber atom (*excitation*) or to completely remove the electron from the atom (*ionization*). At any given time, the particle is interacting with many electrons, so the net effect is to decrease its velocity continuously until the particle is stopped (Knoll 2000).

Generally, the mechanisms by which a charged particle, such as a beta particle, loses its kinetic energy, or is deflected from its original path, involve four principal types of interaction (Evans 1955):

1. *Inelastic collision with atomic electrons.* This is the predominant mechanism by which a beta particle loses kinetic energy in an absorber. As a result of each such collision, one or more atomic electrons experience a transition to an excited state (excitation) or to an unbound state (ionization).
2. *Inelastic collision with a nucleus.* In this case, the incident beta particle experiences a deflection in the field of the nucleus. With this deflection, a quantum of radiation is emitted (bremsstrahlung photons), and a corresponding amount of kinetic energy is lost by the colliding particle.
3. *Elastic collision with nucleus.* The incident particle, in this case, is deflected but does not radiate, nor does it excite the nucleus. The incident particle loses only the kinetic energy required for conservation of momentum between the two particles.
4. *Elastic collision with atomic electrons.* An incident charged particle may be elastically deflected in the field of the atomic electrons of an atom. Such collisions are significant only for the case of very low-energy incident electrons (<100 eV).

When compared with heavy charged particles, beta particles lose energy at a lower rate and follow a much more tortuous path through absorbing materials. Large deviations in the beta particle path are possible because its mass is equal to that of the orbital electrons with which it is interacting, and a much larger fraction of its energy can be lost in a single encounter.

The *linear stopping power*, S , for charged particles in a given absorber is simply defined as the differential energy loss (dE) for that particle within the material divided by the corresponding differential path length (dx):

$$S = - \left(\frac{dE}{dx} \right) \quad [2.1]$$

This value is also called the *specific energy loss*. For fast electrons, Equation 2.2 has been derived (Knoll 2000) to describe the specific energy loss due to ionization and excitation (the “collisional losses”).

$$\begin{aligned} - \left(\frac{dE}{dx} \right)_c &= \frac{2\pi e^4 NZ}{m_0 v^2} \left[\ln \left(\frac{m_0 v^2 E}{2I^2 (1 - \beta^2)} - (\ln 2)(2\sqrt{1 - \beta^2} - 1 + \beta^2) \right) \right. \\ &\quad \left. + (1 - \beta^2) + \frac{1}{8} (1 - \sqrt{1 - \beta^2})^2 \right] \end{aligned} \quad [2.2]$$

In the equation, v and e are the velocity and charge of an electron, N and Z are the number density and atomic number of the absorber atoms, m_0 is the electron rest mass, β is the ratio of v/c (c is the speed of light), and the parameter I represents the average excitation and ionization potential of the absorber and is normally treated as an experimentally determined parameter for each element (Knoll 2000).

The linear specific energy loss through radiative processes identified by subscript “r” (bremsstrahlung) is,

$$-\left(\frac{dE}{dx}\right)_r = \frac{NEZ(Z+1)e^4}{137m_0^2c^4} \left[4 \ln \frac{2E}{m_0c^2} - \frac{4}{3} \right] . \quad [2.3]$$

The yield from heavy charged particles is negligible as indicated by the presence of the m_0^2 factor in the dominator of the multiplicative term in Equation [2.3]. The factors of E and Z^2 in the numerator show that radiative losses are most important for high electron energies and for absorber materials of large atomic number. The total linear stopping power for electrons is the sum of the collisional and radiative losses:

$$\frac{dE}{dx} = \left(\frac{dE}{dx}\right)_c + \left(\frac{dE}{dx}\right)_r . \quad [2.4]$$

And the ratio of the specific energy losses is approximately given by:

$$\frac{(dE/dx)_r}{(dE/dx)_c} \cong \frac{EZ}{700} . \quad [2.5]$$

Therefore, radiative losses from typical-energy beta particles in absorbers of low atomic number are always a small fraction of the total energy loss.

Beta particles often undergo large-angle deflections along their paths. This leads to the phenomenon of *backscattering*. This effect could remove an entering beta particle from the surface through which it entered. Because these backscattered electrons do not deposit all their energy in the medium (detector), backscattering

can have a significant effect on the response of detectors which have been designed to collect electron energy spectra. Beta particles with high incident energy and absorbers with low atomic number have the lowest probability for the backscattering effect (Knoll 2000).

2.2 Gamma-Ray Sources and Interactions

2.2.1 Gamma-Ray Sources

Radioactive transformations, such as beta decay, often leave the transforming nucleus in an excited state in which the protons and neutrons in the energy shells of the nucleus are not in the most tightly-bound state possible (Martin 2000). As the protons and neutrons in the nucleus rearrange themselves to the desired lowest-energy state, this excitation energy will be emitted as electromagnetic radiation. The gamma-ray energy is essentially equal to the difference in energy between the initial and final nuclear states. The gamma rays therefore appear with a half-life characteristic of the parent nucleus, but with energy that reflects the energy level structure of the daughter (Knoll 2000). Nuclear states have quantized energy levels; therefore, gamma rays energies are very specific and are characteristic of that particular nucleus. Because gamma-rays are produced only to relieve excitation energy, it is incorrect to refer to this process as gamma decay (Martin 2000). Examples of gamma emission after beta decay from ^{60}Co and ^{137}Cs radionuclides are depicted in Fig. 2.3.

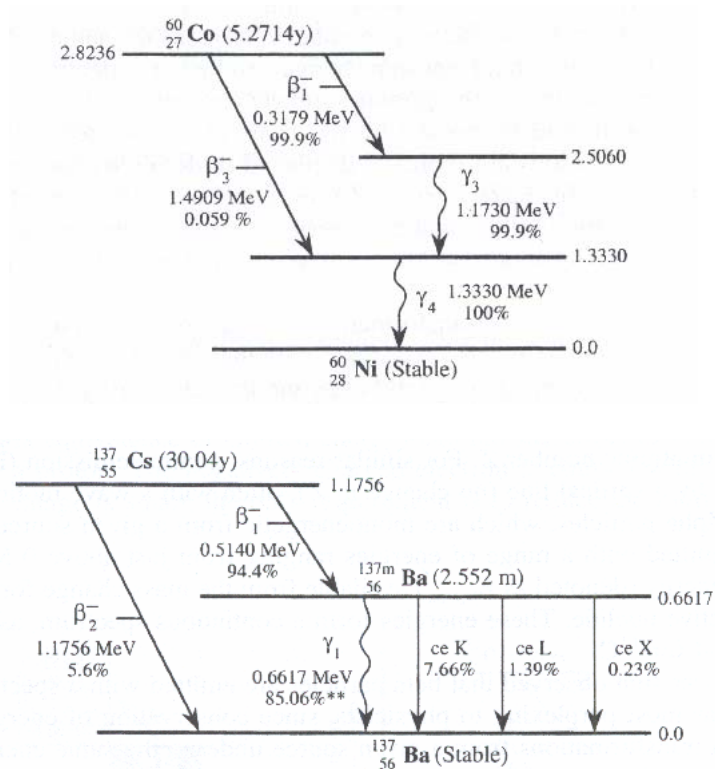


Fig. 2.3: Transformation of ^{60}Co and ^{137}Cs to stable nuclides by beta decay and their immediate gamma-ray emissions (taken from Martin 2000).

2.2.2 Interaction of Gamma-Rays With Matter

For detection and spectroscopy purposes, three major mechanisms for the interaction of gamma-rays are considered significant. Two of these mechanisms, *photoelectric absorption* and *Compton scattering*, predominate in the case where the energy of the gamma-ray does not greatly exceed 1.02 MeV. In the case of higher-energy photons, *pair production*, which is a direct conversion of electromagnetic energy into mass, occurs. These three gamma-ray interaction

mechanisms result in the release of electrons in the absorber. The relative importance of the three interactions for different absorber materials and gamma-ray energies (Evans 1955) is illustrated in Fig. 2.4.

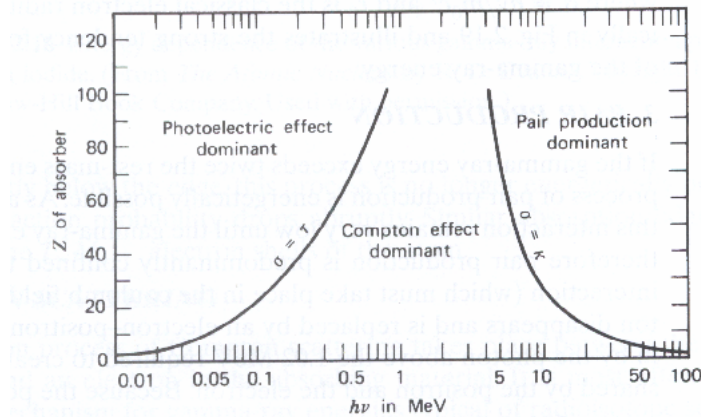


Fig. 2.4: The relative importance of the three major types of gamma-ray interaction (taken from Evans 1955).

a) **Photoelectric Absorption.** In this interaction, a photon interacts with an absorber atom and the photon completely disappears. The photon energy dislodges a *photoelectron* from one of the atom's bound shells. The interaction is with the atom as a whole or with an individual electron, but one that is tightly bound, and cannot take place with free electrons. The most probable origin of the photoelectron is from the most tightly bound K shell. The photoelectron energy is given by,

$$E_{e^-} = h\nu - E_b \quad [2.6]$$

where E_b is the binding energy of the photoelectron in its original shell. Moreover, the photoelectric interaction leaves an ionized absorber atom with a vacancy in one

of its orbital shells. By capturing a free electron from the medium or rearrangement of electrons from other shells of the atom, this vacancy is rapidly filled. The rearrangement of electrons may generate one or more characteristic X-rays. From Fig. 2.4, it is evident that for gamma-rays of relatively low energy, the photoelectric interaction is the predominant process. Additionally, the probability of this interaction increases for absorber materials of high atomic number.

b) Compton Scattering. In this interaction mechanism, the incident gamma-ray photon is scattered, by interacting with an electron, through an angle θ with respect to its original direction (Fig. 2.5).

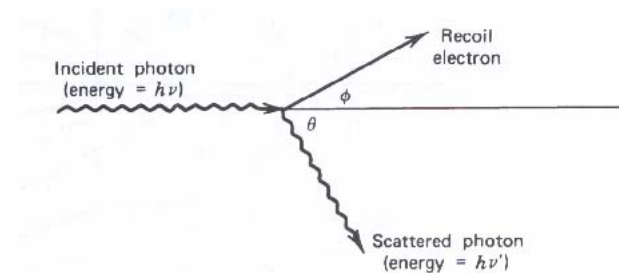


Fig. 2.5: Recoil electron and scattered photon from Compton scattering (taken from Knoll 2000).

Differing from the photoelectric process, only a portion of the photon's energy is transferred to the electron, in this case known as a recoil electron. The energy transferred to the recoil electron can vary from zero to a large fraction of the

incident gamma-ray energy. By writing simultaneous equations for conservation of energy and momentum, Equation [2-7] can be derived:

$$hv' = \frac{hv}{1 + \frac{hv}{m_0c^2}(1 - \cos\theta)} \quad , \quad [2.7]$$

where m_0c^2 is the rest-energy of the electron (0.511 MeV). From the above equation, the scattered photon has its maximum energy at $\theta = 0$ where $hv' = hv$, and has its minimum energy at $\theta = \pi$ where $hv' = hv/(1+2hv/m_0c^2)$.

c) Pair Production. Based on Einstein's special theory of relativity, when a high-energy (>1.022 MeV) photon interacts with the strong electromagnetic field surrounding a nucleus, as illustrated in Fig. 2.6, the photon's energy can be converted into a pair of electron masses, one of which is negatively charged (the electron) and the other is positively charged (the positron).

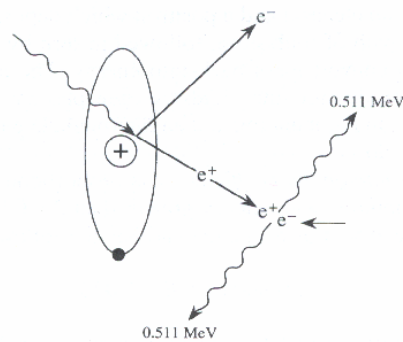


Fig. 2.6: Pair production interaction (taken from Martin 2000).

The positron and electron share the energy remaining after the electron masses have been formed ($h\nu - 1.022$). As a practical matter, the probability of this interaction remains very low until the gamma-ray energy approaches several MeV, and therefore pair production is predominantly confined to high-energy gamma rays (Knoll 2000). Eventually, the energy of the positron and electron will be absorbed in the medium and, because the positron will subsequently annihilate after slowing down in the absorbing medium, two annihilation photons (0.511 MeV) with opposite direction are produced.

2.3 Scintillation Detector Principles

2.3.1 Scintillation Theory

Scintillators are materials that produce visible or ultraviolet photons upon absorption of ionizing radiant energy. Using a photomultiplier tube (PMT), these light photons are converted to a detectable signal pulse. An ideal scintillator is transparent to its own light, possesses fast light-emission times, has a high degree of scintillation efficiency, has light emission properties that are linear with deposited energy, and has good optical qualities (Knoll 2000). There are several types of scintillators in various physical and chemical states. These include organics as polymers, crystals, thin films, loaded scintillants, and liquids; inorganics as crystals (e.g., NaI, CsI, LiI, ZnS, CaF₂, CsF); silicate glasses

containing lithium or cerium; and noble gases. Fluorescence in the organic scintillators originates from energy-level transitions within the structure of a single molecule, whereas fluorescence in inorganic crystals takes place in the lattice structure.

The excitation and de-excitation processes in organic scintillators can be described adequately by simple exponential rise and decay times. Rise times are typically very short (on the order of hundreds of picoseconds) and decay times are typically on the order of 1-4 nanoseconds, dependent on the molecular energy-state structure of the organic. The light output from an organic scintillator can be described by the expression (Knoll 2000)

$$I = I_0(e^{-t/\tau} - e^{-t/\tau_1}) \quad [2.8]$$

where τ is the decay time constant and τ_1 is the excitation time constant. Even though their light output is relatively low, organic scintillators, because of their lower atomic numbers, are most commonly used for electron or beta spectroscopy.

The light emission processes of inorganic crystals are based on excitation and de-excitation of energy states in the lattice structure. Excited states essentially are all formed at once and then decay exponentially. Although other processes, like afterglow and quenching do occur, the light emission timing characteristics are adequately described by a single exponential. The inorganics tend to have greater light yield and scintillation linearity with energy deposition, but have longer decay

times relative to the organics, on the order of hundreds to thousands of nanoseconds. Inorganics generally have a higher Z than the organics and, therefore, will be more susceptible to low-energy gamma interference and more likely to cause backscatter of incident betas. Many of the inorganic scintillators are specifically used for gamma spectroscopy because of their higher density. Most inorganic scintillators are hygroscopic and, therefore, require encasement to prevent breakdown from atmospheric moisture.

2.3.2 Scintillation detectors

As illustrated in Fig. 2.7, scintillation detectors generally consist of a scintillation material and a device, such as a photomultiplier (PM) tube or photodiode, to convert scintillation light to an electrical signal pulse.

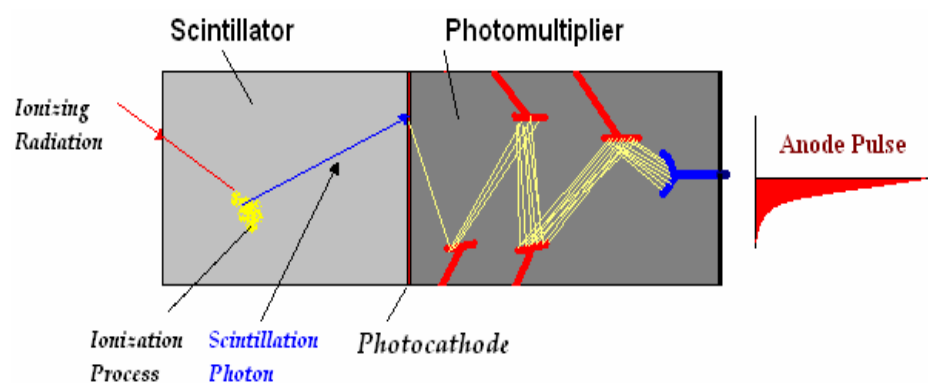


Fig. 2.7: Simplified schematic of a scintillation detector.

The basic elements of a typical PM tube are depicted in Fig. 2.8. The first step to be performed by the PM tube is the conversion of incident scintillation light photons into photoelectrons. Because only a few hundred photoelectrons may be involved in a typical pulse, their charge is too small at this point to serve as a convenient electrical signal. The electron multiplier section in a PM tube provides an efficient collection geometry for the photoelectrons as well as serving as a near-ideal amplifier to greatly increase their number. After amplification through the multiplier structure, a typical scintillation pulse will possess $10^7 - 10^{10}$ electrons, sufficient to serve as the charge signal for the original scintillation event. This charge is easily collected at the anode or output stage of the PM tube.

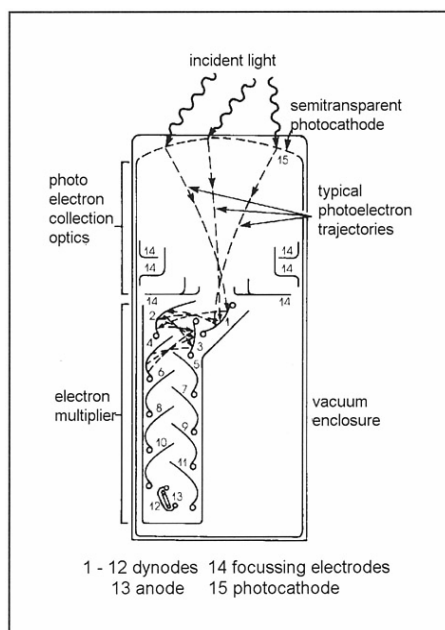


Fig. 2.8: Basic elements of a Photomultiplier Tube (PMT) (taken from Knoll 2000).

2.3.3 Scintillation Pulse-Shape Analysis

The pulse shape of the electrical signal following a scintillation event depends on the time constant of the anode circuit. The rate of electron collection at the PM anode, $i(t)$, is illustrated in Fig. 2.9a. It can be shown (Knoll 2000) that the voltage pulse at the anode follows the expression,

$$V(t) = \frac{1}{\lambda - \theta} \frac{\lambda Q}{C} (e^{-\theta t} - e^{-\lambda t}), \quad [2.9]$$

where λ is the scintillation decay constant, $\theta = 1/RC$, is the reciprocal of the anode time constant, and Q is the total charge collected over the entire pulse. Two cases can be identified depending on the length of the anode time constant:

Case 1. Large time constant: if $\theta \ll \lambda$, Eq. [2.9] can be approximated as

$$V(t) = \frac{Q}{C} (e^{-\theta t} - e^{-\lambda t}). \quad [2.10]$$

With this condition, $V(t)$ will have a shape as illustrated in Fig. 2.9b. The tail of this pulse has the time behavior $e^{-\theta t}$ and therefore decays at a rate determined by the anode circuit time constant, RC . The maximum amplitude of this pulse is Q/C which is proportional to the energy of the original incident radiation. Most

scintillation detectors are based on this configuration because the pulse height is maximized and subsequent sources of noise will have minimal degrading effects on pulse-height resolution.

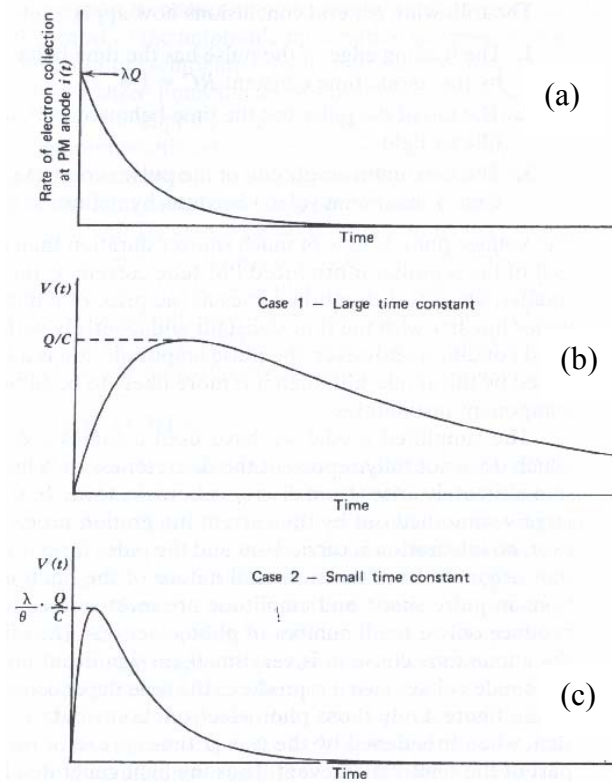


Fig. 2.9: Voltage pulse for the two extremes of large and small anode time constant (modified from Knoll 2000).

Case 2. Small time constant: if $\theta \gg \lambda$, Eq. [2.9] becomes

$$V(t) = \frac{\lambda}{\theta} \frac{Q}{C} (e^{-\lambda t} - e^{-\theta t}) \quad [2.11]$$

As seen in Fig. 2.9c, the tail of this type of pulse has the behavior $e^{-\lambda t}$ and therefore decays at a rate determined by the scintillator decay constant. The maximum amplitude of the pulse is now $\lambda Q / \theta C$, a great deal smaller than in Case 1. This configuration is very useful in specific applications where analyzing the time profile of pulses is the first priority in the radiation detection process. In the current research, since gamma- and beta-induced pulses are discriminated by their pulse shapes, this configuration will be employed.

2.4 Phoswich Detectors

The combination of two dissimilar scintillators optically coupled to a single photomultiplier tube is often called a phoswich (or phosphor sandwich) detector. The scintillators are chosen to have different decay times so that the shape of the output pulse from the photomultiplier tube is dependent on the relative contribution of scintillation light from the two scintillators. Generally, phoswich detectors are designed either for simultaneous detection of different radiation types (White et al. 1999, Usuda et al. 1997) or for minimizing the recording of background radiation in a radiation field of interest (Erkkila et al. 1985, Hsu et al. 1998). In both applications, each scintillation layer is chosen to be sensitive to a particular radiation type. Independent measurements of the energy deposited in each scintillator can then be obtained without the need for a second PM tube (Farsoni and Hamby 2005).

2.4.1 Radiation Detection Using Phoswich Detectors

Many researchers have been involved in developing detection systems capable of differentiating between radiation types (Langenbrunner et al. 1992, Usuda et al. 1992a, 1992b, 1994a, 1994b, 1997, Takada et al. 1996, Childress et al. 2002, Bush-Goddard 2002, Bardelli et al. 2002, Ely et al. 2003 and Hennig et al. 2006).

Bardelli et al. (2002) developed a triple-layer phoswich detector for identification of fast charge particles. The detector was built using three different scintillators, BC404, BC444 and CsI(Tl) coupled to a single photomultiplier tube (PMT): the corresponding decay times were equal to 1.8 ns, 180 ns and ~1000 ns, respectively. The anode signal of the phoswich detector results from the sum of three signals, their relative amplitudes being determined by the energy loss of the impinging particle in each detected event, and can be used for identification purposes. A fast digitizing system was used to sample signals from the phoswich detector and analyze their shape.

Usuda et al. (1997) developed a triple-layer phoswich detector for simultaneous counting of alpha, beta (gamma), thermal and fast neutrons. The phoswich detector is shown in Fig. 2.10. The separation of pulses induced from different radiation types was carried out by using an analog pulse-shape discrimination technique. The first layer, ZnS(Ag), is sensitive to alpha particles and is relatively transparent to the other radiation types.

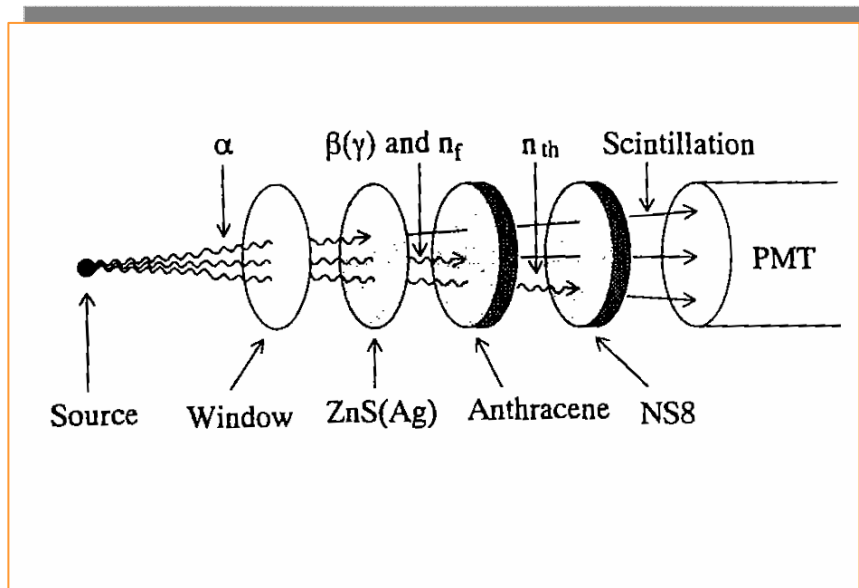


Fig. 2.10: A phoswich detector designed by Usuda (1997) for simultaneous counting of alpha, beta (gamma), thermal and fast neutrons.

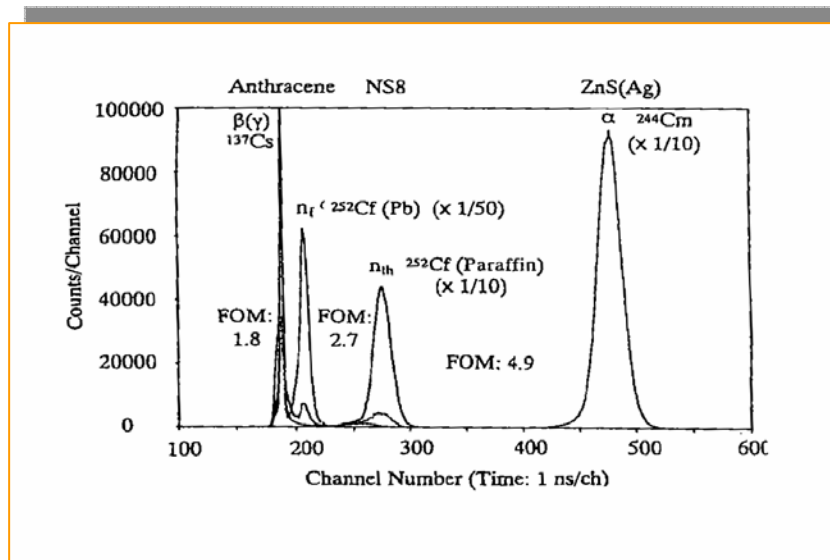


Fig 2.11: The rise-time distribution measurement for discrimination of different radiation types (Usuda et al. 1997).

The second layer, Anthracene, is sensitive to gamma, beta and fast neutrons, but is relatively transparent to thermal neutrons. After passing through the first two layers, thermal neutrons are absorbed in the NS8 scintillator. The rise-time distribution measurement, when the phoswich detector was exposed to different radiation types, is illustrated in Fig. 2.11.

From Fig. 2.11, except for gamma-rays and beta particles from ^{137}Cs (the first peak with the shortest rise-time), all other radiation types can be discriminated through their corresponding rise-times. In Usuda's work, the difficulty arises in separation between beta and gamma rays because of the similarity of radiation interactions within the scintillators, resulting in the same amount of rise time for both radiations.

Childress et al. (2002) developed a triple-crystal phoswich detector that also allows for simultaneous detection of alpha, beta and gamma radiation. In this design, a $\text{CaF}_2:\text{Eu}$ crystal was used for both gamma and beta interactions, but the problem of gamma/beta mischaracterization was left unsolved. In addition to this "crosstalk", typical phoswich detectors are only able to discriminate between different types of radiations at the expense of losing spectroscopic information. Therefore, this makes them useful only for "particle identification" rather than "radionuclide identification" in which the need for collecting the spectroscopic data from each radiation component in the field is vital.

Bubble Technology Industries (BTI)¹ has developed a new product, MICROSPEC-2, which contains a small, portable computer with multichannel analyzer and four spectroscopic probes for gamma, X-ray, beta and neutron detection (Hsu, H. and others 1998). The beta probe is a phoswich detector containing two scintillation layers. Although the distortion of the beta energy spectra, due to gamma-rays present in the field, is eliminated, beta and gamma-ray measurements still must be performed in two separate measurements with the appropriate probe.

A phoswich detector developed recently by Ely et al. (2005) consists of two scintillation layers, a $\text{CaF}_2(\text{Eu})$ layer (decay constant 940 nsec) and a $\text{NaI}(\text{Tl})$ layer (decay constant 230 nsec) intended for detection of radioxenon via a beta/gamma-coincidence measurement technique. The scintillation layers were optically coupled to a single PMT with an integrating preamplifier. Then, rising pulses from the preamplifier were digitally captured and analyzed. By choosing a sufficient density thickness of $\text{CaF}_2(\text{Eu})$, 324 mg/cm^2 , Ely's phoswich is designed to stop nearly the highest beta-particle energies from radioxenon decay (905 keV from ^{135}Xe). This enhances the beta spectroscopy capability, but increases the Compton scattering probability and introduces some degree of crosstalk from the incident gamma rays in that layer.

Another phoswich detector design was introduced by Hennig et al. (2006) for radioxenon detection through simultaneous beta/gamma detection. This

¹ Bubble Technology Industries, P. O. Box 100, Highway 17, Chalk River, Ont. K0J 1J0, Canada.

phoswich design also consists of two layers, a plastic scintillator BC-404 (decay constant 1.8 ns) and a CsI(Tl) crystal (with two decay constants of 0.68 and 3.34 μsec), optically coupled to a single PMT. The signal output from the PMT was directly connected to a digital pulse processor. Because radiation pulses are not integrated, but are captured directly, the timing profile of pulses represents the timing profile of light produced in each scintillation layer. To reduce the probability of incident gamma-ray interactions with the plastic scintillator in the design of Hennig et al., the density thickness is reduced to 103 mg/cm^2 , stopping $\sim 360 \text{ keV}$ electrons, thus limiting its ability to accommodate high-energy beta particles.

2.4.2 Methods For Pulse Shape Discrimination

With phoswich detectors, pulse shape analysis (PSA) or pulse shape discrimination (PSD) identifies the signals from each scintillator, thus identifying in which scintillator the energy deposition event occurred.

The rise-time measurement is the most popular technique to discriminate among pulses from a phoswich detector. This technique is based upon the integration of the light pulse (e.g. the anode pulse from the PM tube), followed by the determination of the time at which this integral reaches a certain fraction of its maximum (e.g. time interval between 0.1 and 0.9 of the maximum). A typical setup for the rise-time measurement, using traditional laboratory modules, is illustrated in Fig. 2.12.

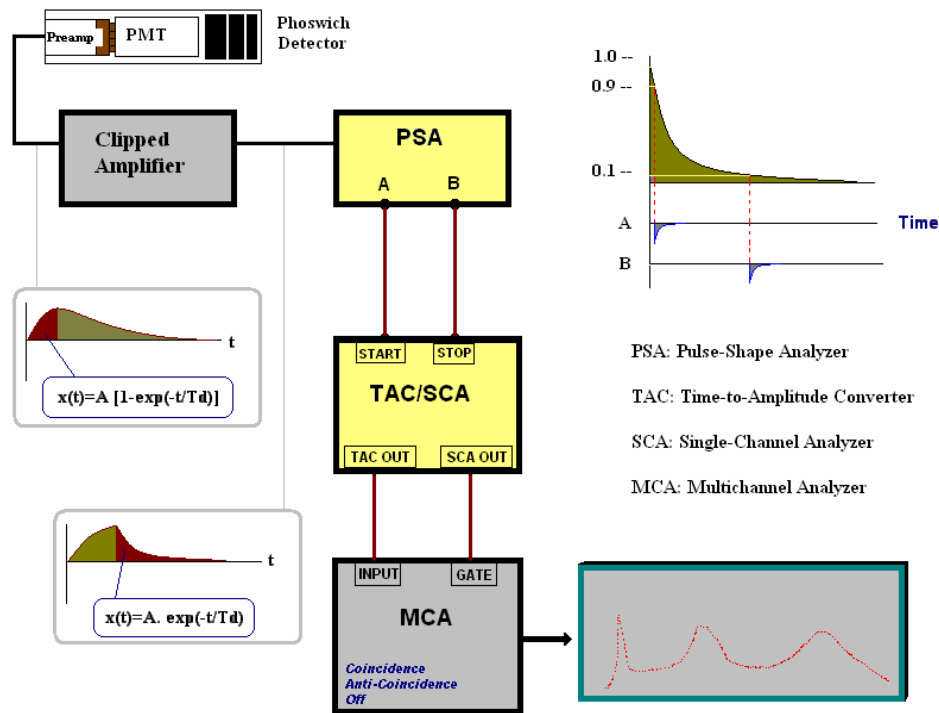


Fig. 2.12: The rise-time measurement using traditional laboratory modules.

Since the anode signal is integrated over an RC network in the preamplifier, the resulting pulse has a shape similar to that shown before the Clipped Amplifier in Fig. 2.12. From Fig. 2.9b, the rise time of this pulse is determined by the decay time of the scintillator in which the radiation energy deposition occurred. Also, the tail of the pulse at the Clipped Amplifier output (Fig. 2.12) decays with the same decay time. A Pulse-Shape Analyzer (PSA) is then used to measure the time interval between 0.1 and 0.9 of the maximum amplitude, which is proportional to the decay time of the scintillator. As illustrated in Fig. 2.12, the PSA generates two sharp signals at its A and B outputs. The Time-to-Amplitude Converter (TAC) then measures this time interval and generates a fixed-length pulse (rectangular pulse)

whose amplitude is proportional to the time interval. At the end, a Multichannel Analyzer (MCA) is used to obtain the rise-time distribution.

This method is only useful when the anode pulse decays with one single component. In some phoswich detectors, where the incident radiation can interact with more than one scintillator, the resulting pulse might have more than one decaying component and therefore this technique can not be applied for pulse shape discrimination.

The majority of PSA/PSD systems operate on analog signal pulses. However, more sophisticated analyses are now possible with the use of digital signal processing (DSP). Recently, with the development of very fast ADCs, digital signal processing methods have gained popularity for analyzing signals from radiation detectors. The use of digital systems offers several advantages over conventional analog units (DeVol et al. 1999), including digital pulse charge integration, reduced dead time, elimination of distorted pulses, noise analysis and minimization, and pulse shape discrimination capabilities.

2.5 Classical and Digital Spectroscopy

The function of a spectrometry system is to convert the electrical-charge pulses originating at the output of the radiation detector into voltage pulses and, afterwards, obtain their amplitude distribution function as accurately as possible (Simoes et al. 1999). For decades, this task has been accomplished using a three stage analog system, schematically represented in Fig. 2.13(a): a preamplifier, a

pulse-shape amplifier, and a multichannel analyzer (MCA) that divides the amplitude space (generally associated to energy) into a number of equally spaced intervals, usually referred to as channels or bins.

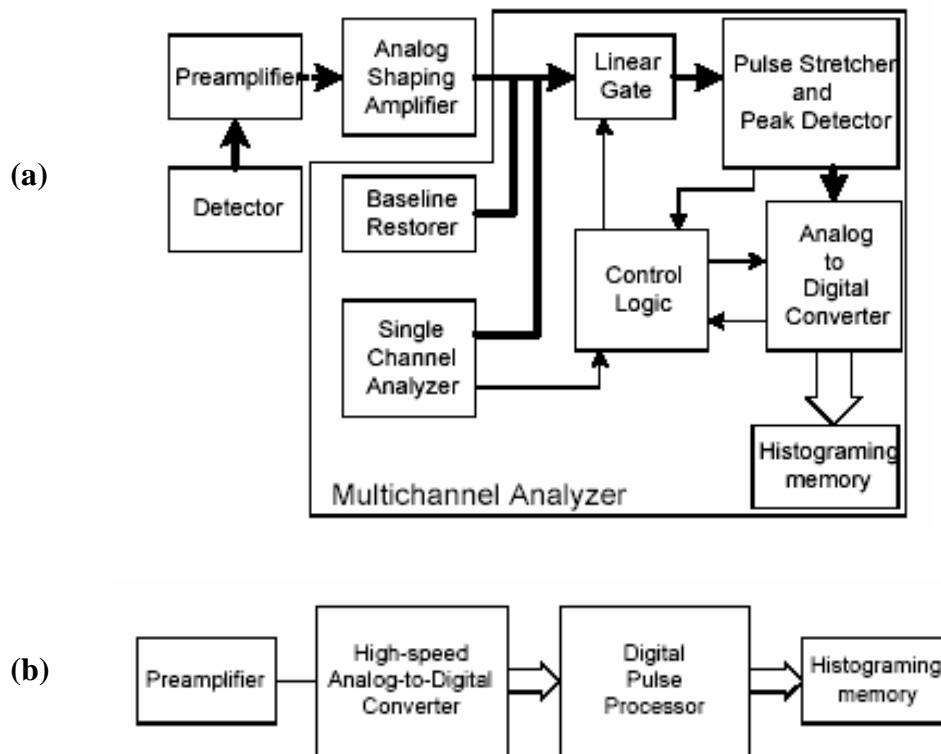


Fig. 2.13: The architecture of (a) classical and (b) digital spectrometers (taken from Simoes et al. 1999).

In the new designs, Fig. 2.13(b), the conventional analog front end is replaced by a digital pulse processor that computes pulse height from the data sampled by a fast, high-resolution ADC. The advantages of this method have been widely recognized (DeVol 1999). For example:

- 1) the pulse processing algorithm is easy to edit, because changes are made through the software;

- 2) the algorithm is stable and reliable, since it is not affected by thermal noise or other fluctuations;
- 3) it is possible to make the detection equipment portable by eliminating most of the bulky analog electronics;
- 4) it is convenient to post-process the pulses;
- 5) it is more cost-effective; and
- 6) effects, such as pile-up (Chrien et al. 1986), ballistic deficit (Georgiev et al. 1993) and charge trapping (Hess et al. 1994) can be corrected for or eliminated at the processing level.

Additionally, signal capture and processing can be based more easily on coincidence criteria between different detectors or different parts of the same detector (Warburton et al. 1999).

3 Material and Methods

3.1 Triple-layer Phoswich Detector

3.1.1 Design and Materials

Based on previous experiments, measurements and MCNP analyses of a prototypic phoswich detector (Farsoni and Hamby 2005), a triple-layer phoswich detector has been modeled, designed and constructed. The phoswich detector, in conjunction with a customized Digital Pulse Processor (DPP), is designed to simultaneously record beta and gamma energy spectra with minimal cross-talk.

Table 3.1: Physical properties for the scintillators used in the phoswich detector.

Scintillator	Density (g/cm ³)	Max. Emission Wavelength (nm)	Light Output (% of NaI)	Index of Refraction	Principle Decay Constant (ns)
BC-400	1.032	423	26	1.58	2.4
CaF ₂ :Eu	3.19	435	50	1.47	900
NaI:Tl	3.67	415	100	1.85	230

To achieve the best performance in the phoswich detector, the following criteria have been considered in its design (Table 3.1):

1. for each radiation type (beta or gamma), unique scintillation layer(s) were assigned;

2. in the scintillation layer(s) assigned for each radiation type, the partial energy deposition by incident radiation was minimized, causing the amplitude of radiation-induced pulses to more accurately represent the energy of the incident radiation;
3. to facilitate pulse shape discrimination, the scintillators were chosen to have sufficiently different decay constants;
4. to maximize the light collection efficiency, the scintillators were chosen to have close “Maximum Emission Wavelength” in their emission spectrum and also possess close “Refractive Index”;
5. to minimize the beta-particle backscattering, the first two layers were chosen from low Z materials (plastic and (CaF₂:Eu)); and
6. to maximize the gamma-ray detection efficiency, the third scintillation layer was chosen to have high Z material (NaI) .

The first two layers of the detector (Figs. 3.1, 3.2 and 3.3) are chosen specifically for beta spectroscopy, with the third layer intended for gamma-ray measurements. The first layer is a very thin plastic scintillator (BC-400) and the second layer is an inorganic crystal (CaF₂:Eu); both are sensitive to beta radiations and their total thickness is enough to stop betas with energies up to about 3.2 MeV. The Phoswich detector is designed such that an incident beta must deposit energy in the first layer or in both the first and second layers for a pulse to be recorded as a beta-induced pulse.

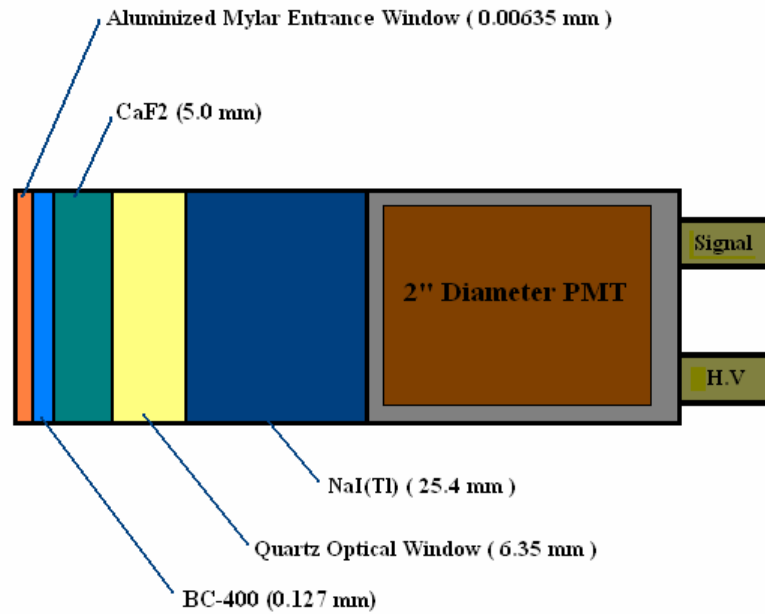


Fig. 3.1: Schematic arrangement of the phoswich detector.

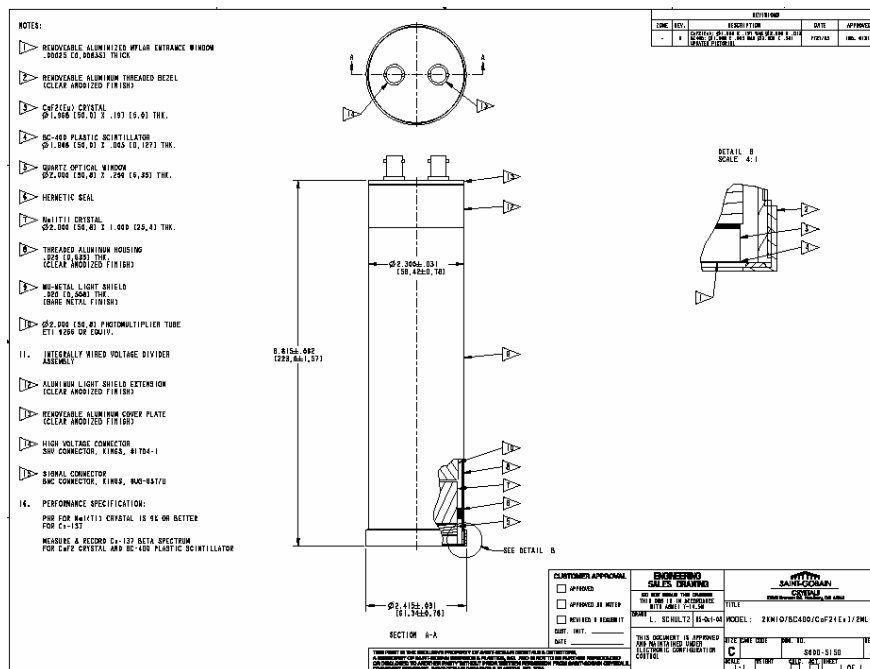


Fig. 3.2: Phoswich detector schematic sketch provided by Saint-Gobain¹.

¹ Saint-Gobain Crystals Inc. 6801 Cochran Road, Solon, Ohio 44139



Fig. 3.3: Triple-Layer phoswich detector constructed by Saint-Gobain.

The third layer (NaI:Tl) is an inorganic scintillator and is intended for gamma-ray measurements. Since plastic scintillators cannot be fully dried and would ultimately hydrate and destroy the performance of the crystal, the NaI:Tl is completely isolated by a thin quartz optical layer. An hermetic seal is made around the quartz, the NaI, and the photomultiplier tube (PMT). The quartz will simply act as a light guide and will only slightly affect the collection of light produced in either the CaF₂:Eu or the plastic. Given the thickness of the first two layers and the quartz, only beta particles of very high energy (> 6.7 MeV) can reach the third layer, so that the light pulses generated in the NaI:Tl represent gamma-ray interactions with no crosstalk from beta particles (from common beta sources).

In the next section, by performing an MCNP analysis and simulation, the probability of all possible scenarios and pulse shapes generated either from incident

gamma rays or beta particles will be studied. This study will provide the criteria to accept and distinguish between gamma-induced pulses and beta interactions.

3.1.2 MCNP Study and Simulations

The MCNP code was used to simulate energy deposition by photons and monoenergetic electrons in each layer of our phoswich detector. It should be noted that, for all probability calculations using MCNP, the energy threshold was assumed to be 10 keV so that events with energies less than this amount were excluded. A sample MCNP input file, for simulating 1000 MeV photons, is given in Appendix A.

A pulse-height histogram was used to study the energy deposition distribution in each scintillation layer for a given set of energy bins. Separate histograms were defined for each scintillation layer to model energy pulses that would be generated in the phoswich detector due to gamma-ray or beta-particle interactions. The simulation utilized full transport calculations for both electrons and photons, also accounting for secondary electrons due to induced bremsstrahlung and characteristic photons. For simplicity, the outer surface of the Mylar layer was defined as a surface source so that photons/electrons would travel through this layer. For all calculations, 10 keV-energy bins were applied.

For electrons with energies less than 1.0 MeV, simulations modeled 300,000 source electrons, whereas for electrons equal to or greater than 1.0 MeV, 500,000

source electrons were necessary to yield relative errors in significant energy bins of 1% or less. For photon (1.0 MeV) modeling, 100,000 source photons were sufficient.

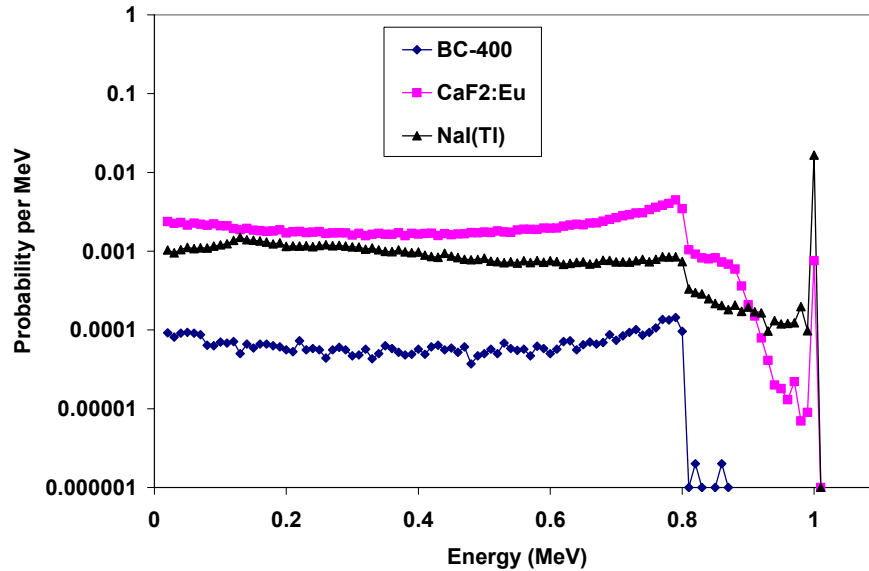


Fig. 3.4: Simulated detector response from 1.0 MeV gamma-rays in all three scintillation layers.

Figure 3.4 shows simulated energy-deposition spectra from 1 MeV gamma-rays in the three scintillation layers. As expected, this figure shows that Compton scatter is the prominent interaction from incident gamma-rays in BC400 and CaF₂(Eu). Since the CaF₂(Eu) layer is thick enough to accommodate electrons up to 3.2 MeV, the unwanted events (mostly Compton scatter) in the beta-side of the detector (CaF₂ (Eu)) are comparable to that of the gamma-side, the NaI(Tl) layer. However, since common beta particles have much shorter mean free paths than

gamma rays in scintillation materials, events in the first layer can be used to identify the beta-induced pulses from beta interactions with $\text{CaF}_2(\text{Eu})$, and so the Compton events can be distinguished quite easily. More details regarding discrimination between photon and electron interactions in the Phoswich detector will be discussed in Chapter 4.

The energy-deposition distributions in Mylar, BC400 and $\text{CaF}_2:\text{Eu}$ from four different monoenergetic electrons have been modeled and are depicted in Fig. 3.5. The energy distribution for Mylar from electrons with energies greater than 50 keV, shows results similar to those of Fig. 3.5(a).

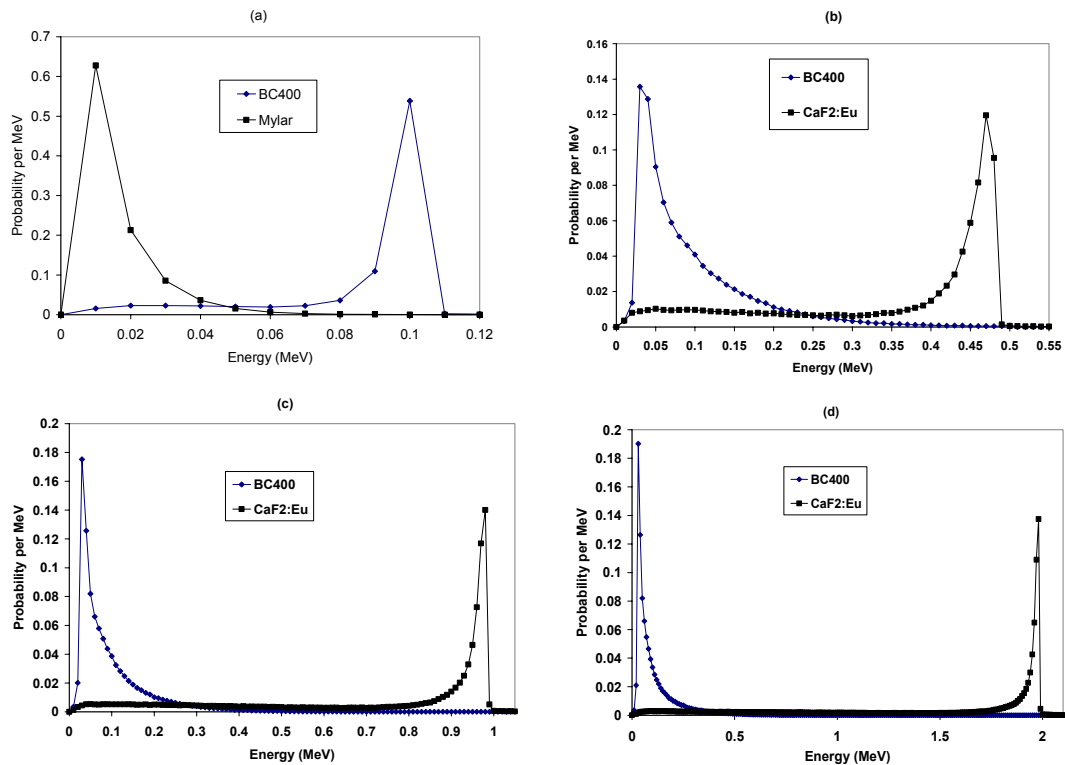


Fig. 3.5: Simulated detector response from (a) 0.1 MeV (b) 0.5 MeV (c) 1.0 MeV and (d) 2.0 MeV monoenergetic electrons in Mylar, BC400 and $\text{CaF}_2:\text{Eu}$ layers.

From Fig. 3.5(a), an energy deposition of about 10 keV is the most probable energy which is deposited in the Mylar. Since the density thickness of the BC400 is enough to stop 100 keV electrons, its probability peak falls around this energy. On increasing the electron energy above 100 keV, the electron begins penetrating into the CaF₂:Eu layer. At 500 keV, electrons most likely deposit energy around 30 keV in the BC400 (Fig. 3.5(b)) and around 490 keV in the CaF₂:Eu. At 1.0 MeV and 2.0 MeV (Figs. 3.5 (c) and (d)), the energy-deposition spectra in CaF₂:Eu have nearly the same shape, but the energy-deposition peak in BC400 shifts to the lower energies, around 20 keV. Fig. 3.6 shows the energy deposition only in BC400 to illustrate how electrons of varying energy interact in the first layer.

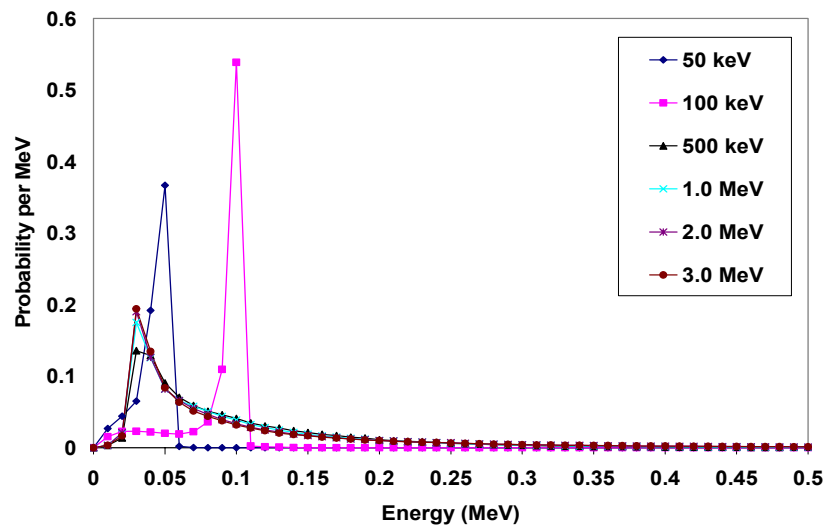


Fig. 3.6: Simulated detector response from different monoenergetic electrons in BC400.

The most important finding, which can be concluded from the electron simulations in Fig. 3.6, is that with increasing electron energy above 100 keV, the most significant component of the spectra shifts toward lower energies. In terms of anode-pulse shape, this means that electrons with energies higher than a threshold, most likely add only a small amount of fast decay component to the generated signal pulse.

By combining three timing components corresponding to the decay constants of three scintillation layers and depending on how a given incident beta or gamma ray releases its energy within each layer, seven possible interaction scenarios for either beta or gamma interactions could occur (Farsoni and Hamby 2005). Corresponding to these scenarios, seven possible pulse shapes could be generated.

The occurrence probabilities for seven possible gamma- and beta-induced pulse types, calculated using the MCNP code, are given in Table 3.2. These results provide the criteria for acceptance of a pulse to be recorded as a beta- or gamma-induced pulse and updating the corresponding energy spectra.

For example, if a pulse is observed with only the fast component (pulse type 1) or both fast and slow components (pulse type 2, Fig. 3.7(a)), the probability that the pulse is gamma-induced is 0.35% or 0.07%, respectively. Whereas, the probability for a beta particle with the same energy producing the same pulse type is 12.30% or 81.70%, respectively. Therefore these types of pulses update the corresponding beta-particle energy histogram. However, if a pulse is observed as having only a decaying component corresponding to energy deposition in the

Table 3.2: Pulse acceptance/rejection criteria calculated using MCNP simulation.

Scenario	Scintillation Layers			Total Probability (%)*		Pulse Recorded as:
	BC-400	CaF2	NaI:Tl	Gamma	Beta	
1	×			0.35	12.32	Beta
2	×	×		0.07	81.70	Beta
3		×		14.40	4.60	Rejected
4	×		×	0.06	0.08	Rejected
5		×	×	2.65	0.03	Rejected
6	×	×	×	0.01	0.57	Rejected
7			×	12.87	0.00	Gamma

* Total probabilities are calculated for 1.0 MeV photon/electron events. Events with energies less than 10 keV were excluded as electronic noise.

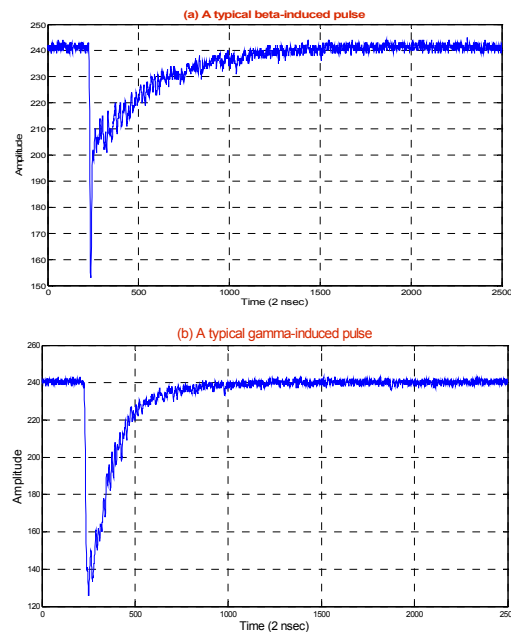


Fig. 3.7: A typical anode pulse from: (a) beta absorption in both BC-400 (fast component) and CaF₂:Eu (slow component), and (b) gamma absorption in NaI(Tl).

Nal(Tl) (pulse type 7, Fig. 3.7(b)), the probability that the pulse is from a 1 MeV gamma-ray or beta particle is 12.87% or 0.00%, respectively. This type of pulse, therefore updates the corresponding gamma-ray energy histogram.

When the radionuclide emits both beta and gamma-rays, gamma/beta coincident pulses can be detected from pulse types 4 and 6. For this study, since the beta- or gamma-only pulses are being considered, pulse types 3, 4, 5 and 6 are not recorded.

3.2 Data Acquisition System

A schematic for the Data acquisition system, including the digital pulse processor, host PC and MATLAB software, is illustrated in Fig. 3.8. The anode output from the PM tube is directly connected to the digital pulse processor. When a valid event occurs, the digitally captured pulse is transferred to the host PC via a high-speed USB (2) interface. A valid event occurs in the DPP if the captured pulse possesses a predefined duration and amplitude. The MATLAB algorithm processes the radiation pulse and if the pulse meets additional predefined criteria, one of the energy spectra, gamma or beta, is updated.

3.2.1 Digital Pulse Processor

After impedance matching in the preamplifier, the radiation signal pulse is routed through a low-pass Nyquist filter. The analog-filtered pulse is then sampled by a 12-bit/100 MHz ADC to provide sufficient time and amplitude resolution.

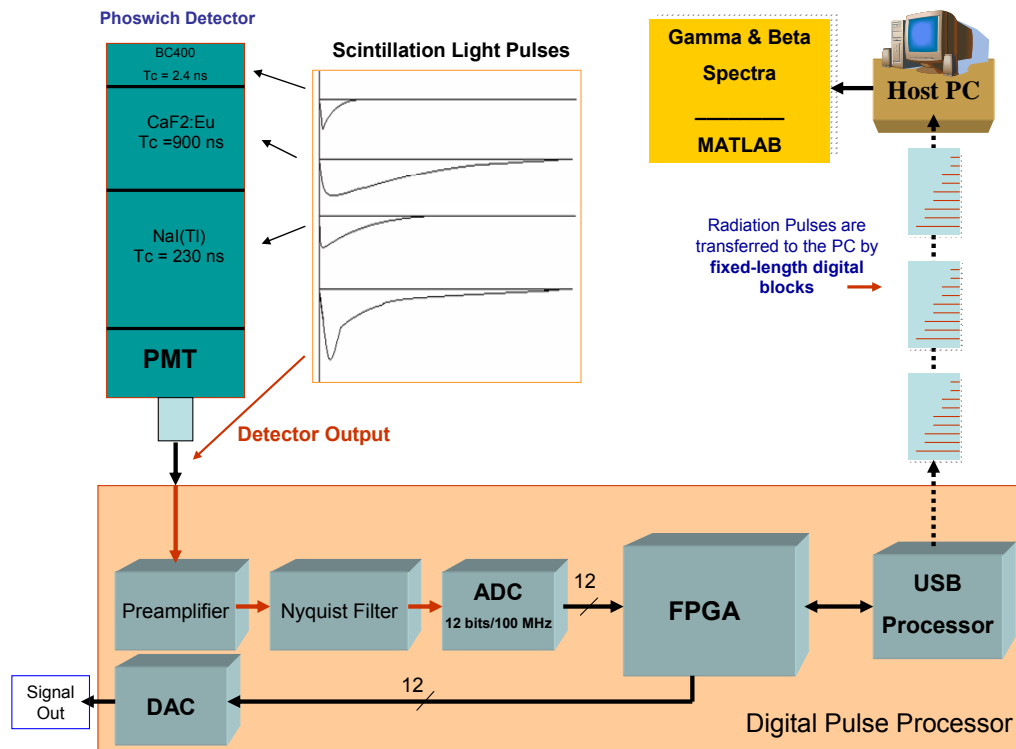


Fig. 3.8: A simplified block diagram of the data acquisition system including the Digital Pulse Processor unit, host PC and the MATLAB software.

The sampled pulse may be reconstructed if, and only if, the ADC sampling rate is greater than or equal to twice the highest frequency component contained in the waveform (Nyquist-Shannon Theorem, Mitra 2001). It is therefore necessary to restrict the signal frequency bandwidth to below half of the sampling rate, e.g. below 50 MHz. A low-pass 3rd-order Bessel filter, with a cutoff frequency of 40 MHz, is designed to perform the Nyquist filtering. The Nyquist filter also has another important task; it stretches the shaped signal so as to be spread out in time (Bardelli et al. 2002). This can eliminate the need for higher sampling rates to capture very fast pulses due to radiation interactions in the BC-400.

The digitized pulses are then passed through a Field Programmable Gate Array (FPGA). The FPGA, which consists of gates, flip flops, distributed and block RAM's, may be described as a "highly parallel configurable digital signal processor" (Bolic et al. 2002). The FPGA allows calculations to be carried out in parallel, thereby significantly increasing the Digital Signal Processing (DSP) speed. It is fully reprogrammable, allowing different application-specific configurations to be used with the same hardware. The control module, host interface and circular buffer are implemented in the FPGA. The control module performs the trigger logic, over-range detection and partial pile-up rejection.

The FPGA configuration is developed using the high-level language VHDL (Very-high-speed integrated circuit Hardware Descriptive Language). An event trigger will be issued if a valid pulse is detected by the control module. The role of the trigger is to recognize that an event has arrived and needs to be processed (i.e., a signal pulse determined to be valid; versus pulse pileup or pulses due to cosmic radiations, which will be rejected). The trigger causes the circular buffer to stop filling its memory with incoming samples and also informs the MATLAB algorithm that a valid radiation pulse in the circular buffer is ready to be read. When the reading is complete, the control module in the FPGA enables the circular buffer to accept the next in a line of radiation events. This repeats until the MATLAB algorithm sets the control module to its idle state.

The DPP board is equipped with a reconstruction DAC which is very useful for troubleshooting purposes. The DAC allows the manipulated waveform to be

easily viewed on an oscilloscope and compared to the original signal directly from the detector.

3.2.2 Analog Circuitry

The complete schematic of the analog circuitry is shown in Fig. 3.9. The analog section includes a gain-adjustable preamplifier, a low-pass Nyquist filter and a single-ended-to-differential converter.

A 50 Ω resistor is used at the preamplifier positive input to match the input impedance of the operational amplifier with the coaxial cable characteristic impedance (50 Ω). The impedance matching is required to prevent signal reflections at the preamplifier input. The preamplifier consists of an operational amplifier (Analog Devices¹ AD8044) in a non-inverting configuration. As a feedback resistor, a 10 K Ω potentiometer is used to provide gain adjustments. For a non-inverting configuration, the voltage gain can be calculated by

$$\text{Gain} = V_{\text{out}}/V_{\text{in}} = 1 + (R_f/R_g) - V_{\text{ref}} \cdot (R_f/R_g) \quad [3.1]$$

Since $V_{\text{ref}} = 0$, $R_f = 0\text{-}10\text{ K}\Omega$ and $R_g = 500\ \Omega$, the gain can be adjusted between 1 to 21.

¹ Analog Devices Inc. One Technology Way, P. O. Box 9106, Norwood, MA 02062-9106

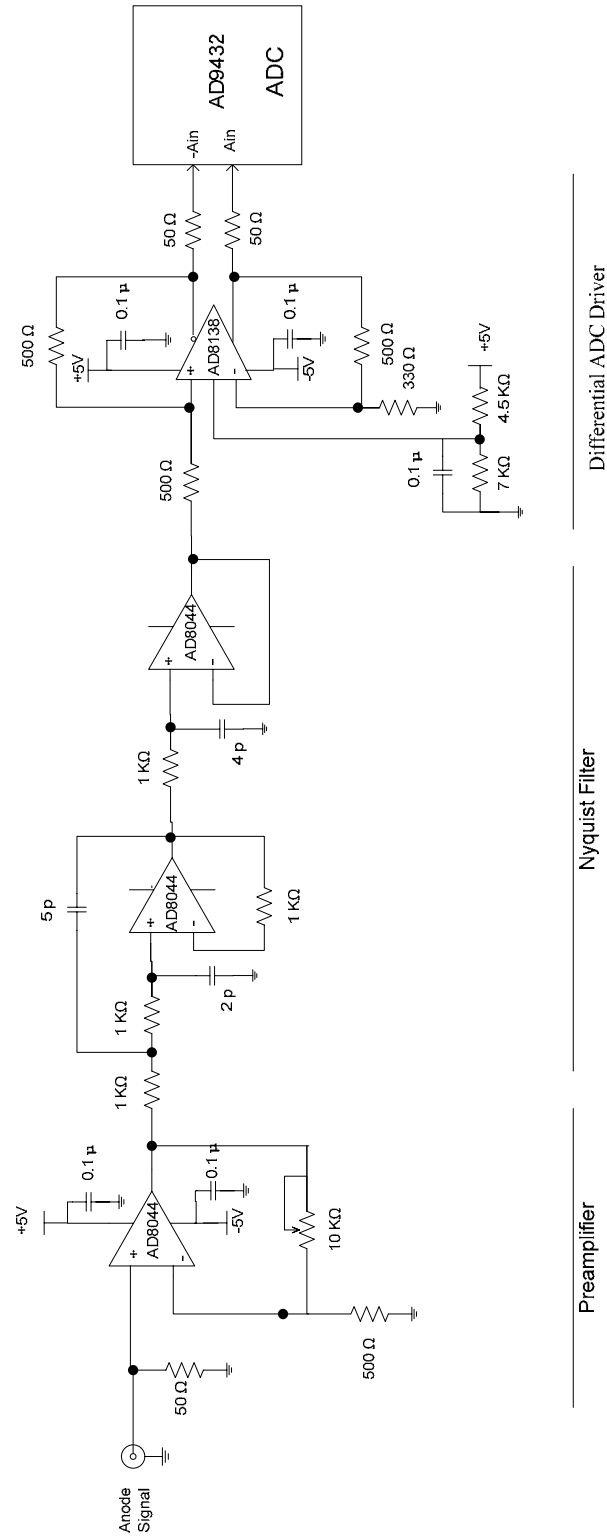


Fig. 3.9: Schematic of the preamplifier, Nyquist filter and differential ADC driver.

A 3rd order Bessel filter with cutoff frequency of 40 MHz is used as the low-pass Nyquist filter. Generally, Bessel filters have better performance (Bardelli et al. 2002) in terms of constant delay (corresponding to smaller signal distortion). The filter design was completed using the realistic models from the Analog Devices Design Center (website www.analog.com).

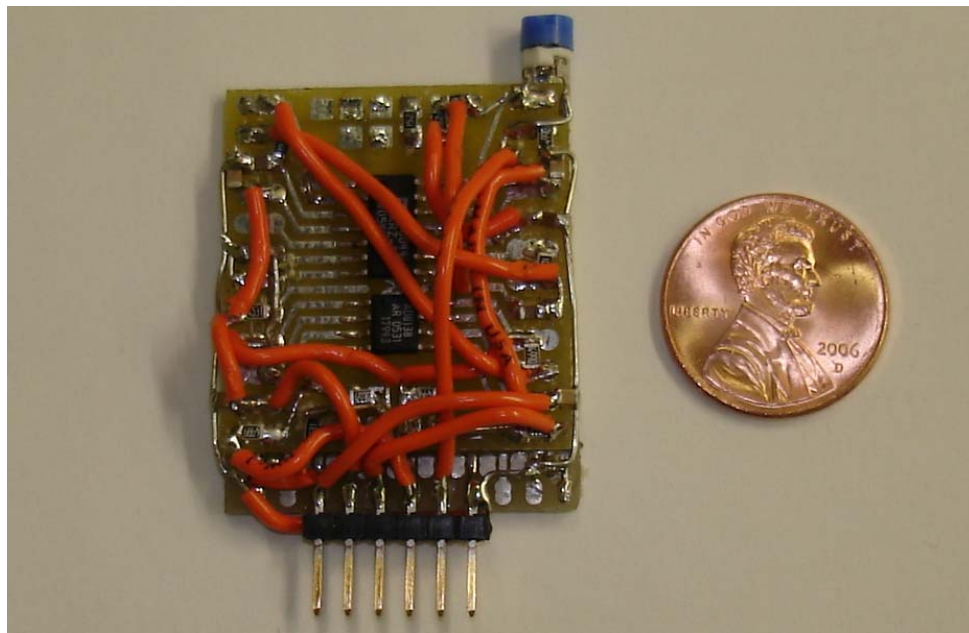


Fig: 3.10: Preamplifier and Nyquist filter assembled on a small daughter board.

The filtered signal must be converted to a differential-ended signal¹. This conversion is performed with a differential output operational amplifier from Analog Devices, the AD8138. The AD8138 was specifically designed for ADC

¹ AD9432 data sheet, Analog Devices Inc.

driver applications. Because the ADC (AD9432) has a differential input with a common-mode voltage of about 3V on both its inputs, a voltage divider (7 K Ω and 4.5 K Ω) was used to provide this potential for the differential driver. To minimize high-frequency pick-up noise (from the digital circuitry), the analog section was assembled on a small and separate prototyping board (Fig. 3.10).

3.2.3 Digital Circuitry

The filtered anode signals from the phoswich detector were examined using a fast digital oscilloscope (TEKTRONIX¹ TDS 1002). These measurements revealed that use of the low-pass Nyquist filter resulted in the fast component, corresponding to radiation interactions in the BC400 layer, being spread over a somewhat larger time interval, approximately 50 nsec. Moreover, the use of three scintillation layers in the phoswich detector with relatively high light output differences (from Table 3.1, max light output ratio is 100/26) expands the dynamic range of the anode output. Therefore, for a higher degree of precise digital measurements, employing an ADC with a low quantization error is necessary. Based on these limitations, the AD9432 ADC with 12-bit resolution and a sampling rate of 100 Msamples/sec was chosen to digitally capture analog radiation signals in a free-running configuration. This sampling rate (with a 10 nsec period) provides at least 5 samples from the

¹ Tektronix Inc. 14200 SW Karl Braun Drive. Beaverton, OR 97077

point where the signal pulse reaches its maximum to its baseline, when a detectable fast component from the BC400 layer appears in the anode pulse. A simplified schematic of the digital circuitry is shown in Fig. 3.11.

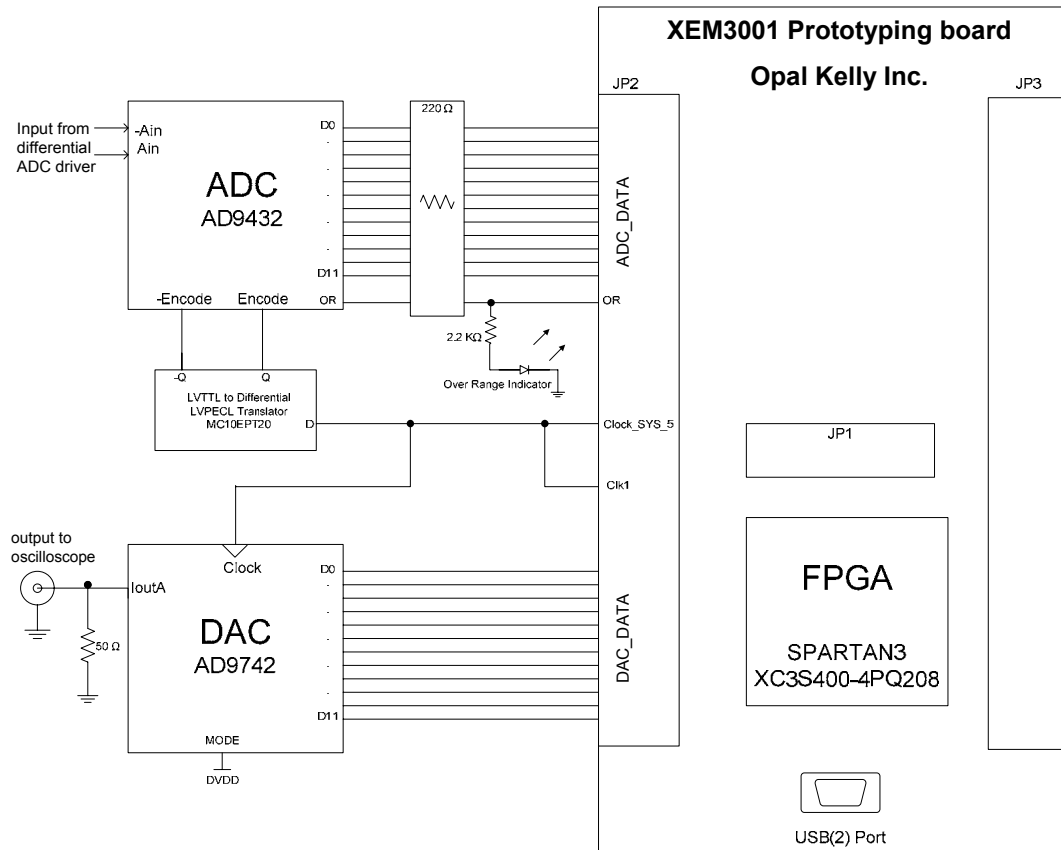


Fig. 3.11: A simplified schematic of the digital circuitry.

The AD9432 ADC has a differential LVPECL input clock. Positive Emitter Coupled Logic, or PECL, is a further development of the emitter coupled logic (ECL) technology and requires a +5V supply instead of a -5V supply. The Low Voltage Positive Emitter Coupled Logic (LVPECL) is an improved version of

PECL to meet today's low-voltage requirements. The PECL is a differential signaling system and is mainly used in high-speed and clock-distribution circuits. An MC10EPT20 translator provides this clock requirement for the ADC. Resistors of $220\ \Omega$ at the ADC outputs limit the current and minimize the high-speed digital noise. The ADC analog inputs, A_{in} and $-A_{in}$, accept 2V peak-to-peak differential signals ranging from -1V to +1V. Beyond these levels, the OR (Over Range) signal goes up (transition from logic level 0 to 1) and stays there until the input signal returns to its range (-1V to +1V). This signal will be used in the Control module (implemented in FPGA) to distinguish valid events from the phoswich detector. Moreover, for prototyping purposes, a red LED is connected to this signal to allow the user to monitor the incoming signals and ensure they are in the acceptable range.

The *CLOCK_SYS_5* pin in Fig 3.11 is the clock source from XEM3001 whereas *clk1* is the input clock to the FPGA. The *Clk1* provides the required clock (100 MHz) for both the controller module and circular buffer. The DAC data inputs are directly connected to the XEM3001 from which there are connections to the I/O pins of the FPGA.

- **DPP Mother Board**

To assemble all parts together, a plain (with two metal layers) board was used as the mother board. Also, to enhance the signal integrity, SMT (Surface Mount Technology) parts (805) were used. For the component assembly and

prototyping purposes, *Solder Mount* boards were used (RDI Wainwright¹). Solder Mounts (Fig. 3.12) are self-adhesive pieces of printed circuit material (epoxy glass) with an etched and tinned pattern of soldering points - each laid out for one or more component types. Components are soldered to a suitable Solder Mount, the paper removed from the adhesive, and the Solder Mount with the component is then placed on a copper clad and tinned ground plane. Usually Solder Mounts are placed on the ground plane before soldering the component.



Fig. 3.12: Solder Mount boards were used to solder and assemble digital and analog parts on the mother board.

¹ RDI Wainwright, 65 Madison Ave, Telford, PA 18969.

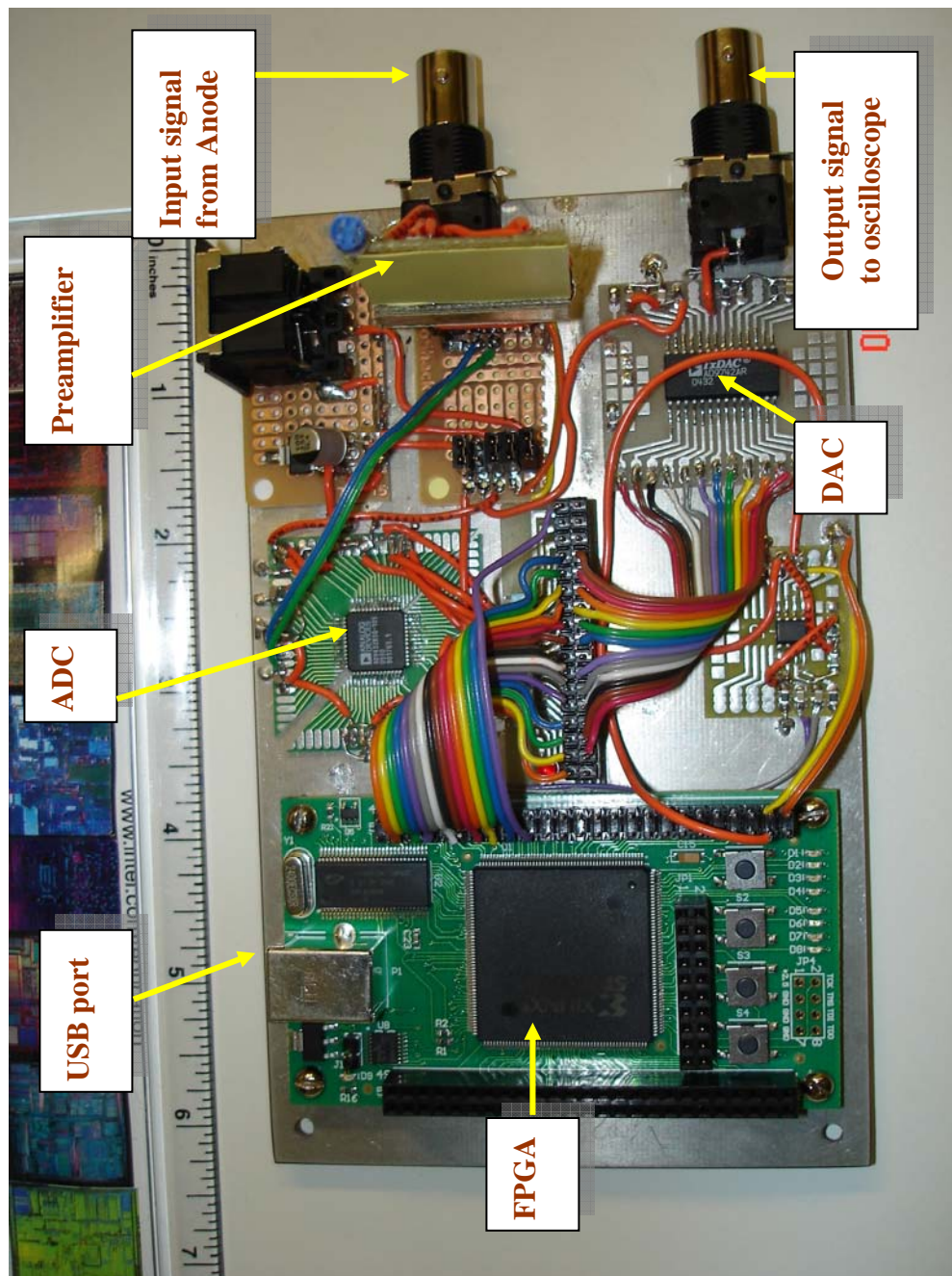


Fig. 3.13: DPP mother board, XEM3001 and preamplifier.

The metal surface of the ground plane serves as ground. The copper-clad ground provides a definite ground potential at every point of the circuit. Stray capacitance to ground is very small, and can be compared to a printed circuit board. Stray fields and wiring inductance is minimized due to the short distance to ground. This makes the Solder Mount system suitable for building high-frequency circuits up to the GHz range.

Step-by-step, before connecting the daughter board (XEM3001), the electronic modules including the preamplifier, Nyquist filter, ADC and DAC were assembled and tested on the mother board (Fig. 3.13).

- **Prototyping XEM3001 Daughter Board**

A prototyping board, XEM3001 (Fig. 3.14), was ordered from Opal Kelly¹. The XEM3001 is an integration module based on a 400,000-gate Xilinx Spartan-3 FPGA (XC3S400-4PQ208C). In addition to a high gate-count device, the XEM3001 utilizes the high transfer rate of USB 2.0 for configuration downloads enabling an almost instant reprogramming of the FPGA. For flexible clocking, a multi-output clock generator can generate clock frequencies from 1 MHz to 150 MHz. After configuration, the USB interface becomes a high-speed bidirectional communications pipe between the PC and our FPGA design, allowing us to transfer

¹ Opal Kelly Inc. 3442 SE Ironwood Ave, Hillsboro, OR 97123

asynchronous and synchronous data using dedicated HDL modules and a MATLAB dynamically-linked library (DLL).

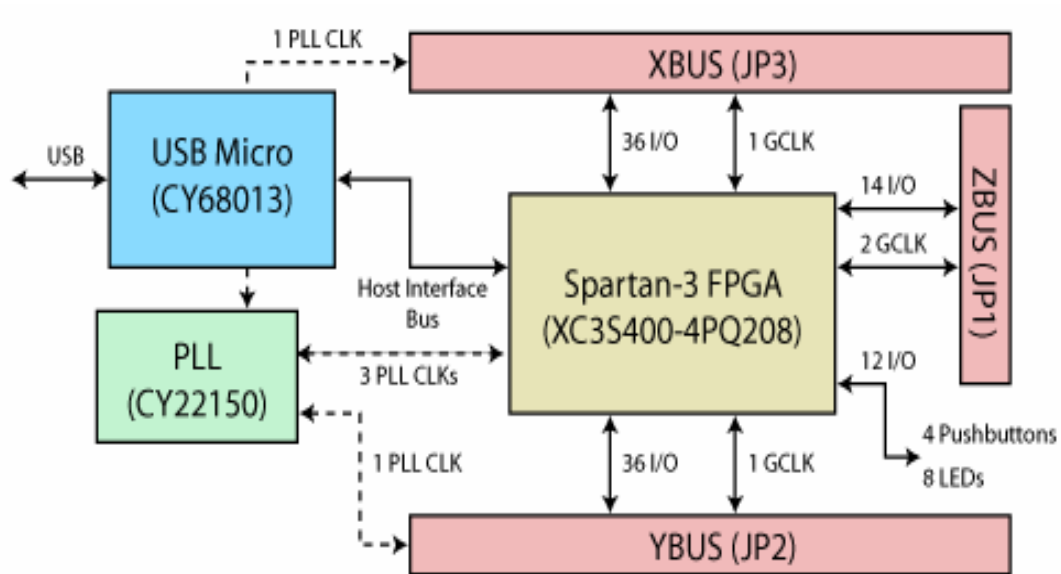


Fig. 3.14: Block diagram of XEM3001.

Utilizing the latest low-cost FPGA from Xilinx, the XEM3001 is well-suited for small-to-medium FPGA designs including signal processing, microprocessor emulation, and general purpose hardware interfaces. The XEM3001 has a 400,000-gate Spartan 3 FPGA with four digital clock multipliers, 16 dedicated 18x18 multipliers, 288-kbits of block RAM, and over 8,000 logic cells. The XEM3001 is fully compatible with Xilinx's free ISE WebPack design tools, including VHDL and Verilog synthesis.

- **Modules Implemented in the FPGA**

To complete the FPGA design, two modules, referred to as “*Top*” and “*Control*” were developed. The Control module performs all control functions including valid pulse detection, trigger logic, baseline delay and over-range pulse rejection. The module together with the Opal Kelly host interface modules, also transfers the pulse data to the MATLAB algorithm. Two clock domains, 100 MHz from the free-running ADC and 48 MHz from the USB processor and host interface, are also involved in the design. Therefore, to cross the clock boundary, the Control module was developed by two separate state machines which are clocked with their corresponding clock signals.

The Top module accommodates the Control, Block RAM, okWireIn, okWireOut, okPipeOut and okHostInterface modules. The MATLAB algorithm determines the start and end of spectra collection via the okWireIn module. However, the MATLAB algorithm is informed by the okWireOut module that a valid pulse in the Block RAM (configured as a circular buffer) is ready to be read. Pulse data is transferred to the PC via the okPipeOut module.

The Block RAM is configured as a circular buffer with 16-bit width and 1024-sample length. Because of the sampling clock of 100 MHz in the ADC, a radiation event with a fixed-duration of 10.240 μ sec can be accommodated in the circular buffer and transferred to the PC.

The incoming samples from the ADC are measured continuously by the Control module. If the value of the sample exceeds the predetermined trigger value, after a

9.0- μ sec delay, the Control module disables the RAM write_enable signal. This stops filling the circular buffer with the next samples. The 9.0- μ sec delay allows the baseline to be measured for 1.24 μ sec before triggering. After uploading the captured data (pulse) to the PC, with one exception, the controller returns to its measuring task to detect the next event. If after reading the RAM content, the value of the next sample exceeds the trigger threshold, the controller does nothing and waits until the sample value falls below the trigger threshold. This eliminates capturing events in which the pulse is riding the tail of a previous pulse. To some extent, this function not only partially rejects some pulse pile-up, but also forces captured pulses to have a reliable baseline before triggering.

Also, to reject events from cosmic radiations, which usually have very large amplitude, during writing the ADC data into the RAM, if the over-range signal goes logic one, the existing pulse will be rejected and the controller returns to its reset state and stays there until the over-range signal returns to logic zero.

- **FPGA Design and Programming**

All the FPGA processes including design, simulation, synthesis, implementation and generation of the FPGA programming file were performed using ISE 8.1i Webpack design software provided by Xilinx Inc. The software is free and can be ordered through the Xilinx website. Fig. 3.15 shows several sections of the software. The simulation process is also shown in Fig. 3.16.

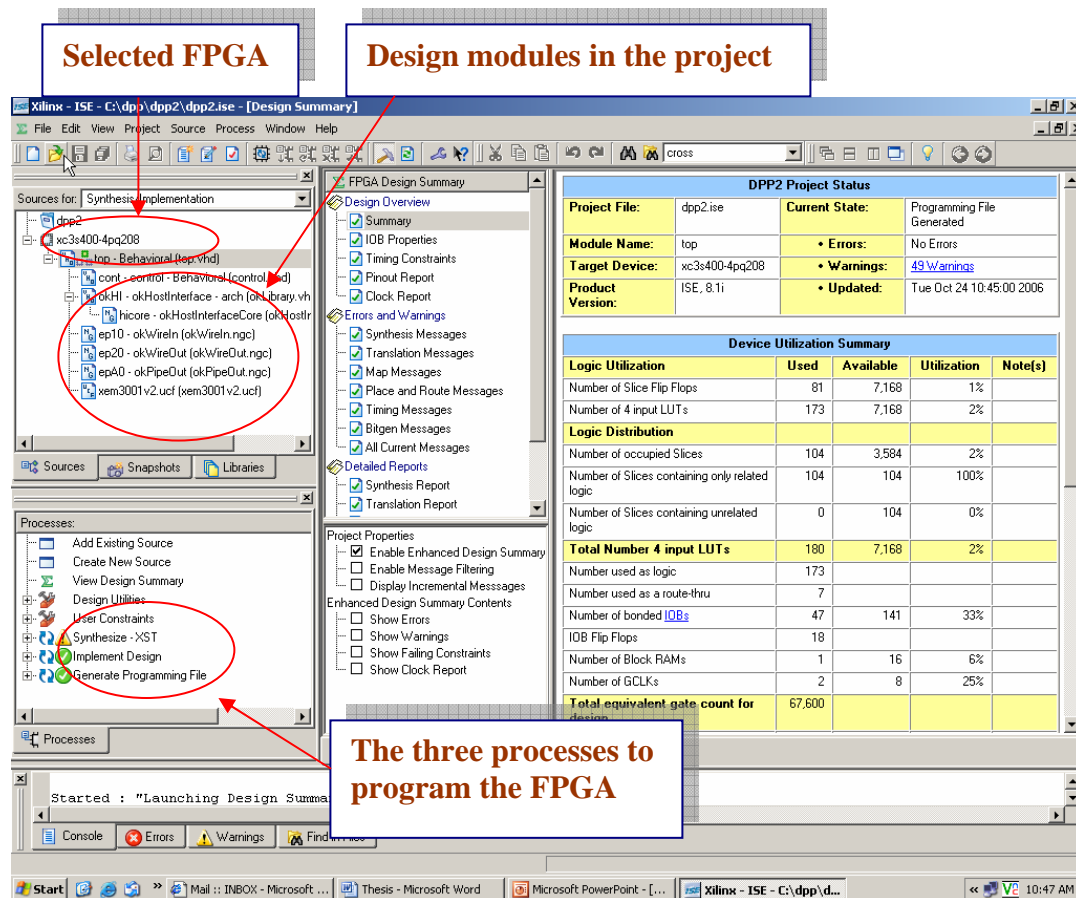


Fig 3.15: ISE 8.1i Webpack for the FPGA design and programming.

Generally, the FPGA design using the Xilinx ISE design tool involves the following steps:

1. *Design Entry and Behavioral Simulation.* The design is created using a Xilinx-supported schematic editor, a hardware description language

(such as VHDL or Verilog) for text-based entry, or both. The design can be simulated using the Xilinx ISE simulator. Using the simulator, before the synthesis and implementation steps, the design can be checked for potential errors or malfunctions;

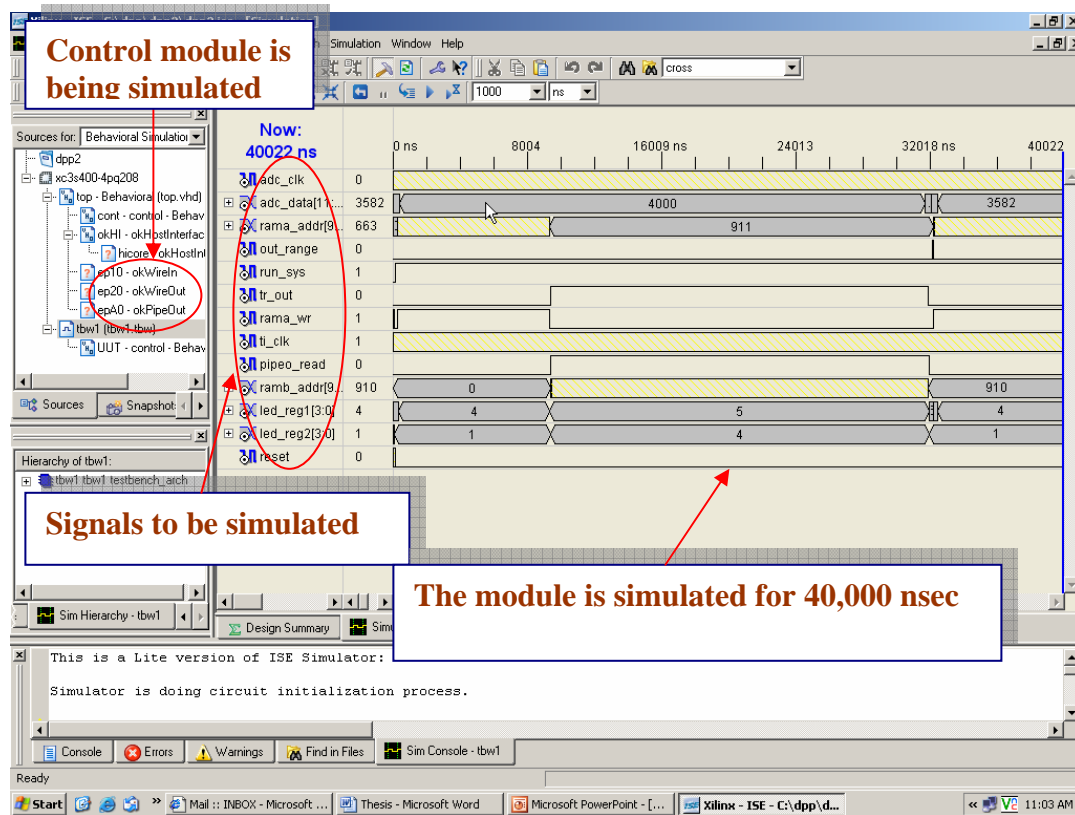


Fig. 3.16: FPGA behavioral simulation using ISE 8.1i Webpack.

2. *Design Implementation.* In this step, the design is implemented to a specific FPGA architecture involving four processes: translation, mapping, placing and routing;

3. *Generating Programming File.* If no error occurs during the synthesis and implementation processes, a programming file is generated to configure the FPGA; and
4. *Design Confirmation.* The design functionality can be checked and confirmed by configuring the FPGA using the generated programming file.

The Xilinx Development System allows quick design iterations through the design flow cycle. Because Xilinx devices permit unlimited reprogramming, the devices do not need to be discarded when debugging circuits.

3.3 MATLAB Algorithm

Based on the MCNP simulation results, an algorithm was developed to digitally process the anode pulses and collect separate beta and gamma energy spectra. For the purpose of pulse-shape discrimination, four parameters (the Baseline, P, M1 and M2) from each pulse are calculated (Fig. 3.17).

For the “Baseline” determination, the average of 100 samples before the trigger point is calculated. The peak of the pulse, P, is the maximum value in all pulse samples. The value of “M1” is an average over the 5 samples just after the fast decay component which is between samples 5 and 9 relative to the peak sample. And, “M2” is the average over the 5 samples between 30 and 34. For purposes of estimating energy deposition, two sums A and B, as depicted in Fig. 3.18, are calculated.

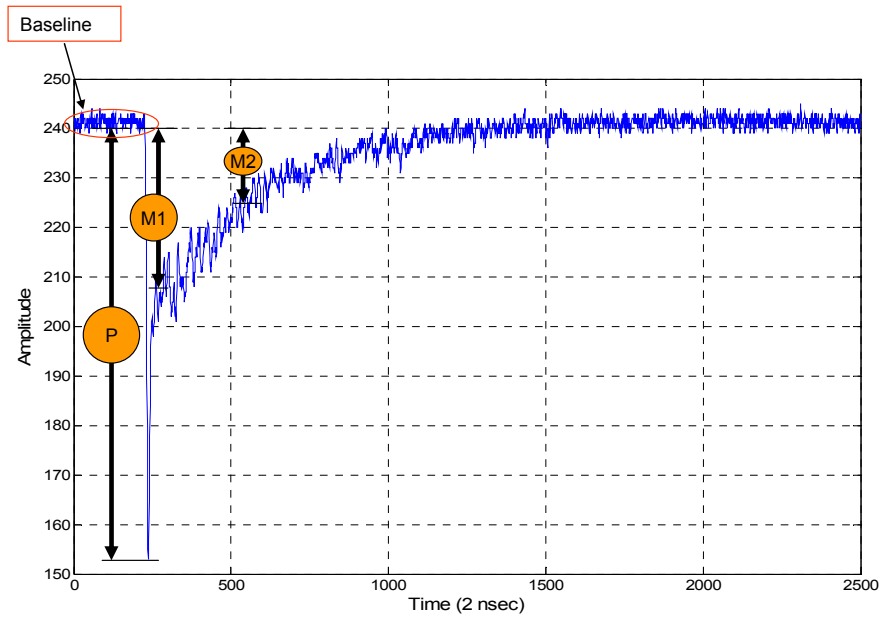


Fig. 3.17: Four parameters, Baseline, P, M1 and M2 are used for analyzing the anode pulses.

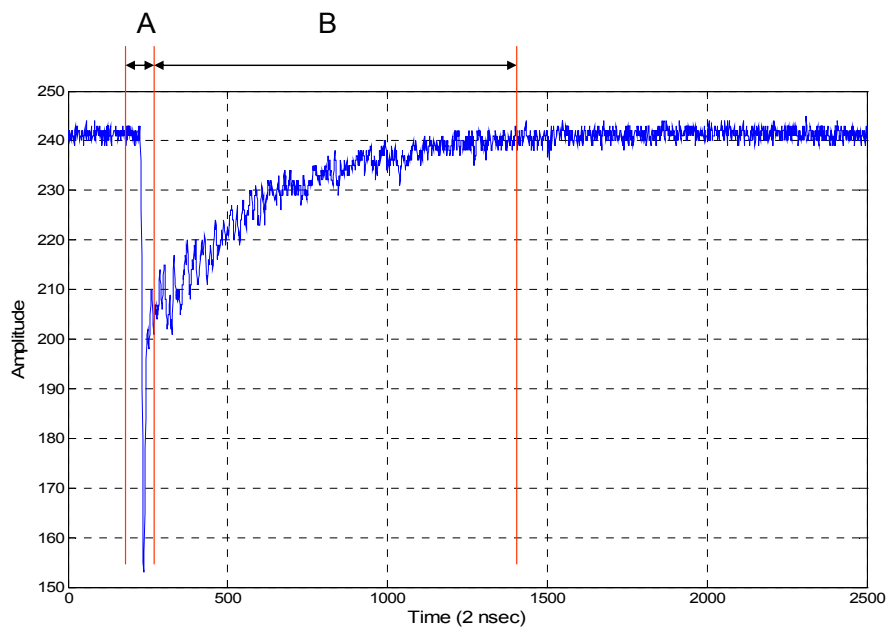


Fig. 3.18: Sums A and B used for calculating the energy absorption in each layer of the phoswich detector.

The sums A and B are proportional to the energy absorption in BC400 and CaF₂:Eu, respectively, if the pulse is determined to be a beta-induced pulse. Also, sum C = A + B is proportional to the gamma-ray energy absorption in NaI(Tl), if the pulse is determined to be a gamma-induced pulse.

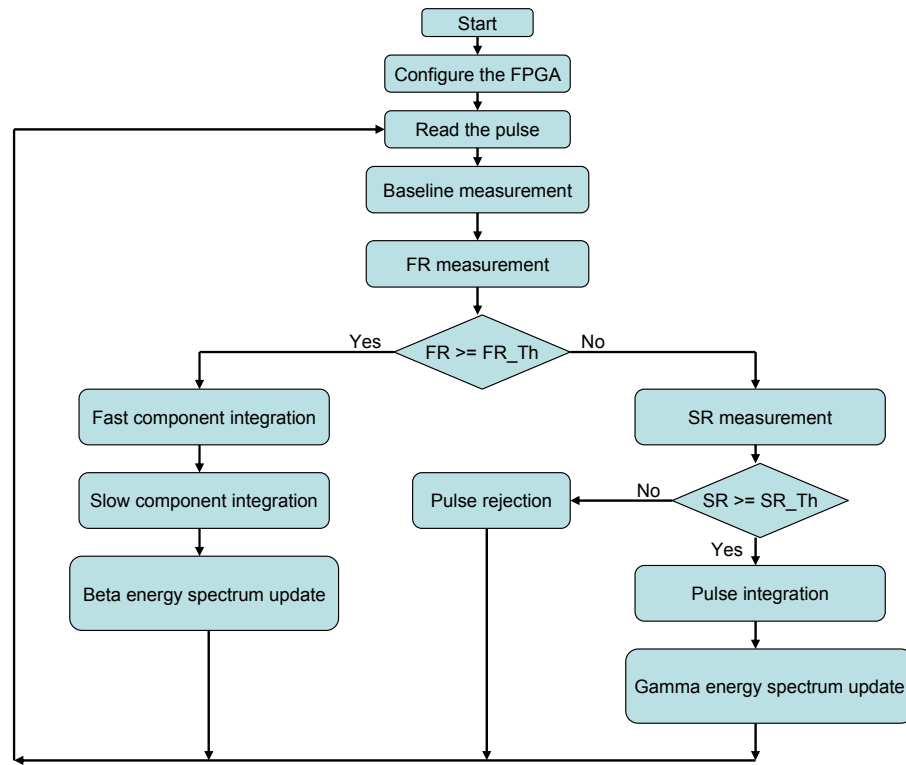


Fig. 3.19: The algorithm developed to collect separate gamma and beta energy-deposition spectra.

A simplified flowchart of the algorithm is shown in Fig. 3.19. After loading the waveform and the baseline measurement, using P and M1, the Fast Ratio (FR) of that pulse is calculated. The FR quantity indicates the presence of a fast component in the pulse and is defined by Eq. 3.2.

$$FR = (P - M1) / P \quad [3.2]$$

Since M1 changes between zero and the value of P, the FR ranges from zero to unity. The FR is then compared to a threshold value, FR_Th. If the pulse passes the inspection, the pulse is considered to be beta-induced; otherwise, it is processed as a gamma-induced pulse candidate.

To be accepted as a gamma-induced pulse, the pulse should pass another inspection. Using a Slow Ratio (SR) measurement, single-component pulses can be discriminated based on whether they originated from the CaF2:Eu or the NaI(Tl) layer. Interactions in the CaF2:Eu layer are most likely due to Compton interactions (see Fig. 3.4) and are rejected. The SR ratio is defined by Eq. 3.3.

$$SR = (M1 - M2) / M1 \quad [3.3]$$

Since M2 varies between zero and M1, the value of SR ranges from zero to unity. At this point, SR is compared to a threshold value, SR_Th. If the pulse passes the inspection, the pulse is considered to be a NaI gamma-induced pulse; otherwise, the pulse is rejected and the next pulse is processed. In both cases, using sums A and B, the absorbed energy in the three scintillation layers is calculated and the corresponding energy histogram or spectrum will be updated. The complete MATLAB code is given in Appendix B.

In the next chapter, the MATLAB algorithm and its experimental parameters such as FR_Th and SR_Th will be discussed in more detail.

4 Results

Measurements with the triple-layer phoswich detector have been performed in two steps. In the first step, the anode pulses were captured using a digital oscilloscope and were transferred to the PC via the serial port (RS232). Generally, these measurements were performed off-line and shape analysis of the radiation pulses was the main goal. In the second step, the anode pulses were captured using our customized Digital Pulse Processor and transferred to the PC via the high-speed USB (2) port. Measurements in this step were performed in real time.

4.1 Measurements Using a Digital Oscilloscope

Using a digital oscilloscope with a 500 MSPS sampling rate and 8-bit resolution, anode pulses were captured directly and then transferred to the PC through the serial (RS-232) port. Radiation events with 2500 samples were transferred during each signal capture. Since the sampling rate of the digital oscilloscope is 500 MSPS, an event duration of 5000 nsec (2500 samples * 2 nsec/sample) was sufficient to accommodate the slowest decay component (decay time of 900 nsec from the CaF₂:Eu, see Table 3.1). Using the serial port, a data block of this size (2500 Bytes) required approximately 1.6 sec for transfer to the PC. For this reason, real-time measurement was not possible. Instead, however, the pulse data from each event were stored one-by-one for processing off-line using a MATLAB algorithm (similar to one introduced in Chapter 3).

The measured Fast Ratio distributions (see chapter 3) from two pure beta emitters, $^{90}\text{Sr}/^{90}\text{Y}$ and ^{36}Cl , and two gamma sources, ^{137}Cs and ^{60}Co are given in Fig. 4.1. In all measurements, the detector was shielded against beta and/or conversion electrons when exposed to gamma sources.

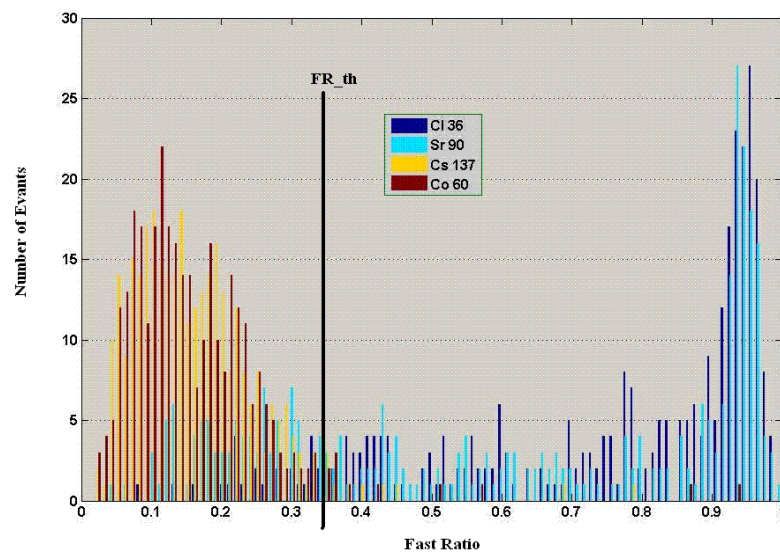


Fig. 4.1: Fast Ratio (FR) distributions from four beta and gamma sources.

The Fast Ratio distribution is determined by the fraction of energy deposited in the BC400 and/or the $\text{CaF}_2:\text{Eu}$ layers. The FR distribution for gamma-ray sources is concentrated at values less than about 0.35. The FR distribution for beta emitters however extends nearly to the entire range, with a significant fraction of beta events located to the right two-thirds of the distribution. The beta events located to the left one-third may correspond to those beta particles which have penetrated into the second layer ($\text{CaF}_2:\text{Eu}$), without depositing any detectable energy in the first layer

(BC400). Pulses with a small FR have only a single slow component and can not be discriminated from a Compton interaction, which may have occurred in the same layer (CaF₂:Eu) from incident gamma-rays.

In measurements using the digital oscilloscope, instead of measuring the Slow Ratio (see Fig. 3.19), the Fall Time of signal pulses was measured. The Fall Time is defined to be the time interval between 80% and 20% of the signal pulse amplitude (peak value). The Fall Time measurement is used for discriminating gamma interactions occurred in the NaI(Tl) layer (with decay constant of 230 nsec) from those of the CaF₂ layer (with decay constant of 900 nsec).

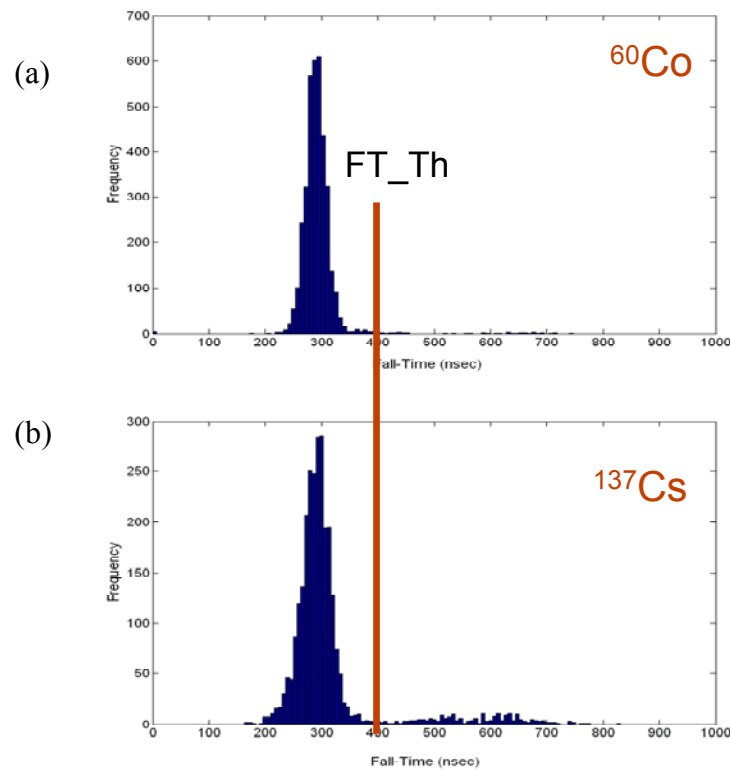


Fig. 4.2: Fall Time (FT) distributions from (a) ⁶⁰Co and (b) ¹³⁷Cs gamma sources.

The measured Fall Time distributions from two gamma sources are given in Fig. 4.2. From the Fall Time distributions, the gamma-induced pulses originated from the NaI(Tl) have Fall Time values less than 400 nsec. In preliminary experiments, the Fast Ratio and Fall Time thresholds were chosen to be 0.35 and 400 nsec, respectively. To evaluate the algorithm's effectiveness at separating gamma and beta events, the phoswich detector was exposed on separate occasions to ^{137}Cs , ^{14}C and $^{90}\text{Sr}/^{90}\text{Y}$ sources. Results are shown in Fig. 4.3.

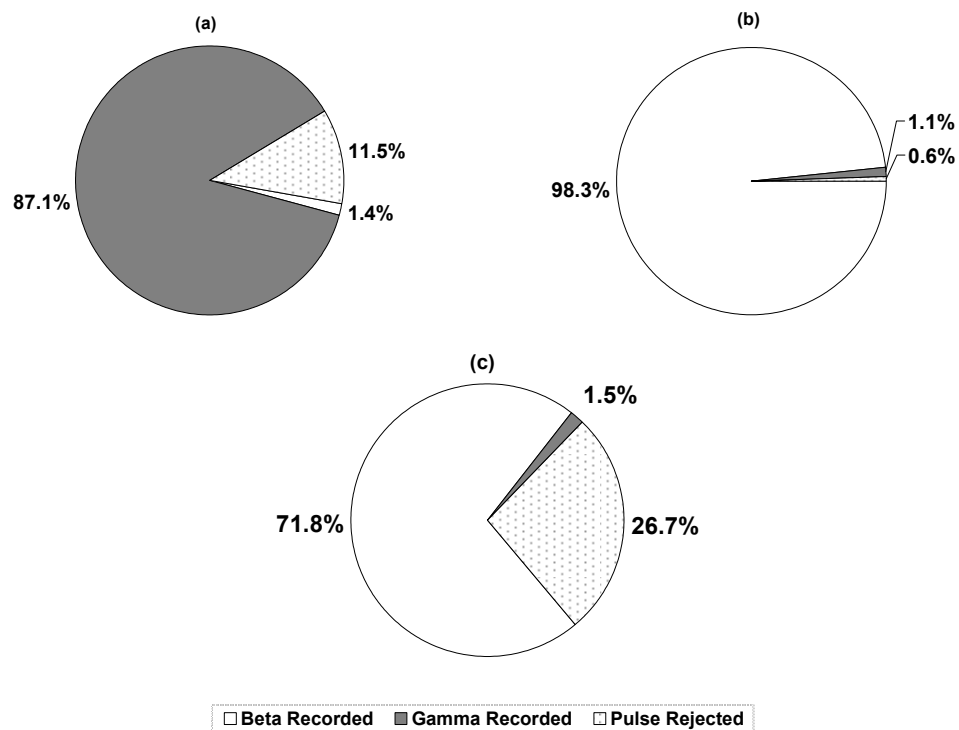


Fig. 4.3: Percentage of events when the detector was exposed separately to (a) shielded gamma ^{137}Cs , (b) pure beta ^{14}C , and (c) $^{90}\text{Sr}/^{90}\text{Y}$ sources.

The large difference in the percentage of rejected pulses in Fig. 4.3(b) and (c) can be explained by considering the MCNP analysis presented in Fig. 3.6. On average, beta particles from $^{90}\text{Sr}/^{90}\text{Y}$ deposit less energy in the BC400 layer than those of ^{14}C . This produces a relatively small fast component in the induced pulses from $^{90}\text{Sr}/^{90}\text{Y}$, resulting in a mischaracterization by the Fast Ratio algorithm. Subsequently, these misclassified pulses (misclassified as gamma) are rejected from any consideration in the Slow Ratio inspection. The rejected gamma events from the gamma source, 11.5%, are likely from Compton scatter in the $\text{CaF}_2(\text{Eu})$, confirmed by the MCNP data. These results indicate that, in all cases, the acceptance of false beta or false gamma pulses occurring less than 2% of the events.

Fig. 4.4 shows the separated beta and gamma spectra when the phoswich detector was exposed to both $^{90}\text{Sr}/^{90}\text{Y}$ and ^{137}Cs sources simultaneously. The simultaneous beta and gamma energy spectra were digitally collected and processed from 15,000 anode pulses. Beta particles and conversion electrons from ^{137}Cs were blocked during spectroscopy. The beta and gamma energy absorption spectra in Fig. 4.4 possess details as expected. For example, in the gamma spectrum, the photopeak has a nearly symmetric shape (FWHM $\sim 8\%$) and the Compton continuum and Compton edge are prominent. The shape of the beta spectrum is similar to that expected from $^{90}\text{Sr}/^{90}\text{Y}$ in that two components can be seen. Some energy degradation is apparent and may result from energy absorption

in air and the Mylar layer, energy absorption in the gap between the BC-400 and $\text{CaF}_2(\text{Eu})$ scintillators, and incomplete energy absorption and electron backscatter in the material interfaces.

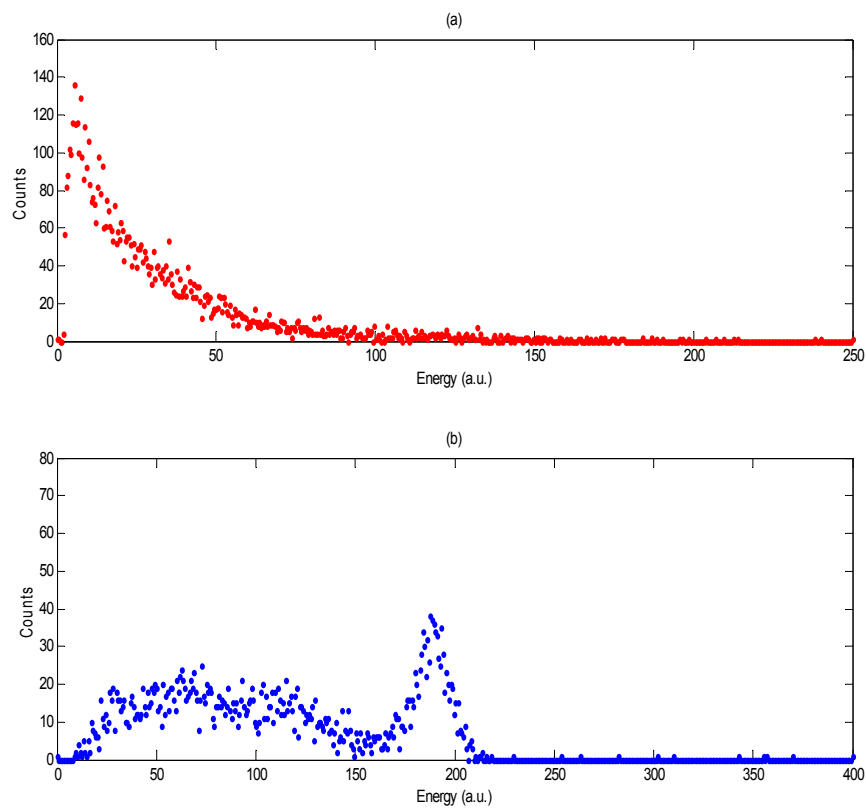


Fig. 4.4: Simultaneous beta (a) and gamma (b) energy spectra (arbitrary units) from 15,000 anode pulses when the detector was exposed to both $^{90}\text{Sr}/^{90}\text{Y}$ and ^{137}Cs sources.

4.2 Measurements Using the Digital Pulse Processor

In this step of the research, anode pulses from the phoswich detector are captured and transferred to the PC using the Digital Pulse Processor (DPP, see section 3.2.1). To estimate the maximum data transfer rate, the ADC data bus was replaced with the output of a 12-bit counter, which was clocked with the *clk1* (100MHz) and implemented in the FPGA. Measurements showed that, in the absence of any digital processing, the system is capable of capturing and transferring 443 radiation pulses to the PC (MATLAB) per second, a significant enhancement of about 709 times the data transfer rate, thus making real-time measurements possible.

4.2.1 Determination of FR_Th and SR_Th

From the algorithm introduced in Chapter 3 (see Fig. 3.17), for discriminating beta events occurring in BC400 and CaF₂:Eu (events 1 and 2 in Table 3.2), the Fast-Ratio measurement must be performed. If the shape of the pulse does not meet the FR requirement, a Slow-Ratio (SR) measurement is performed to ensure that the single-component pulse comes from the NaI(Tl) and not from the CaF₂:Eu layer. To obtain the corresponding optimum thresholds, FR_Th and SR_Th, the FR and SR distributions from gamma and beta sources were recorded. The results from ¹³⁷Cs and ⁶⁰Co shielded gamma-ray sources, and ¹⁴C and ³⁶Cl pure beta particle sources are illustrated in Figures 4.5, 4.6, 4.7 and 4.8, respectively.

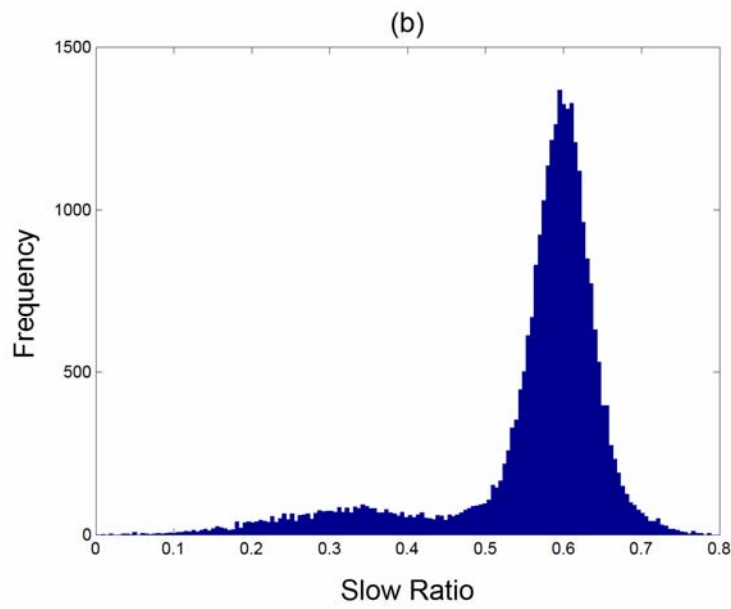
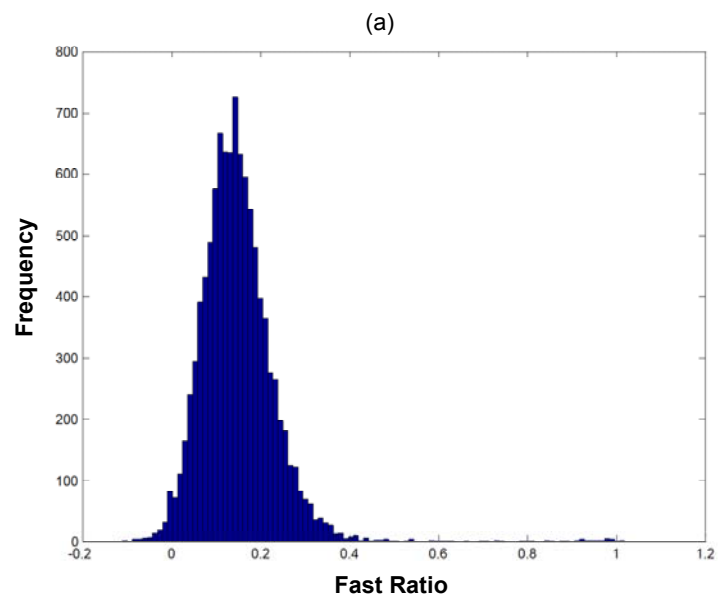


Fig. 4.5: (a) Fast and (b) Slow Ratio distributions from ^{137}Cs shielded gamma-ray source.

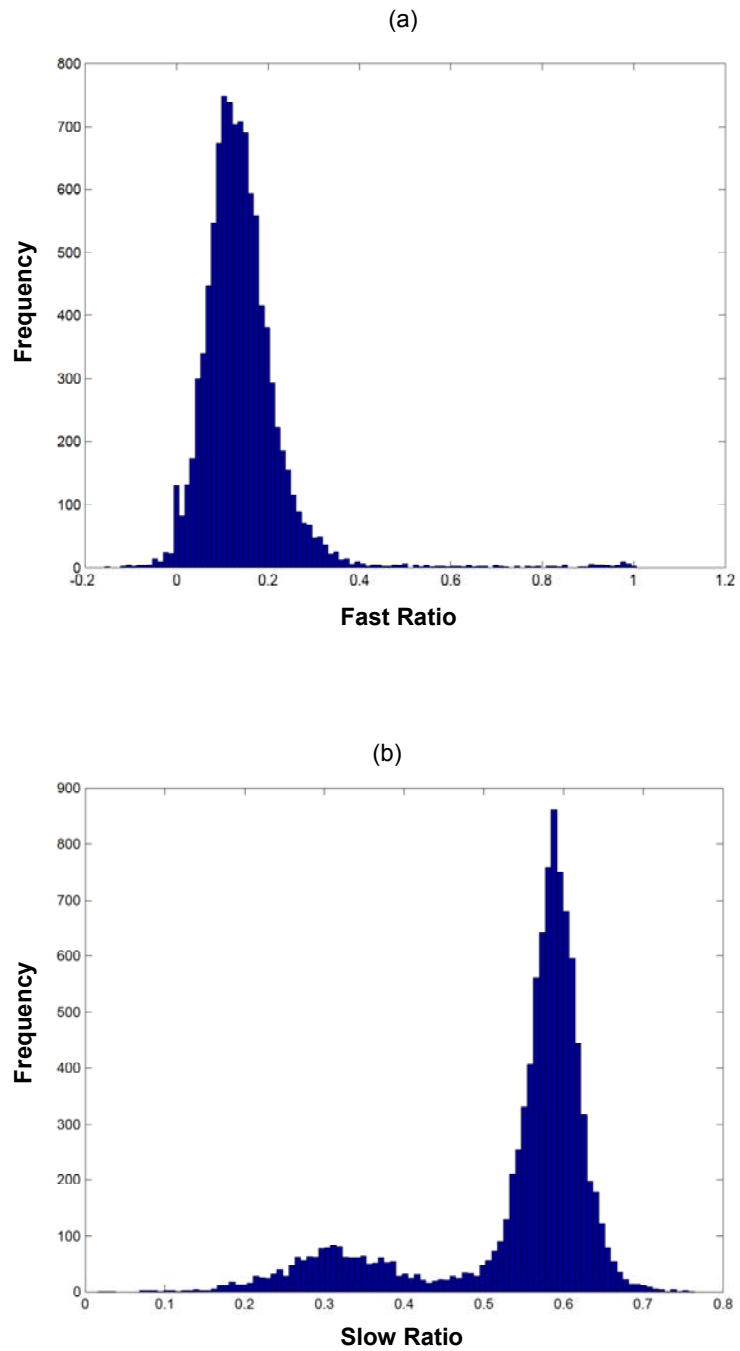


Fig. 4.6: (a) Fast and (b) Slow Ratio distributions from ^{60}Co shielded gamma-ray source.

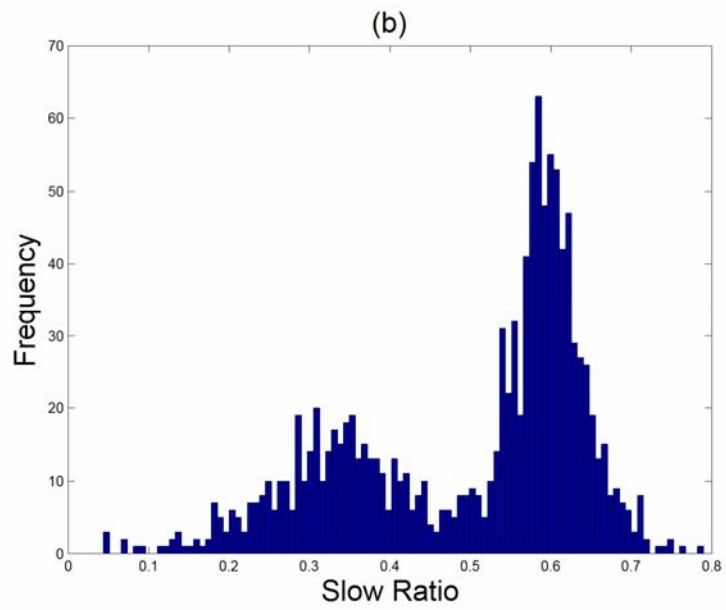
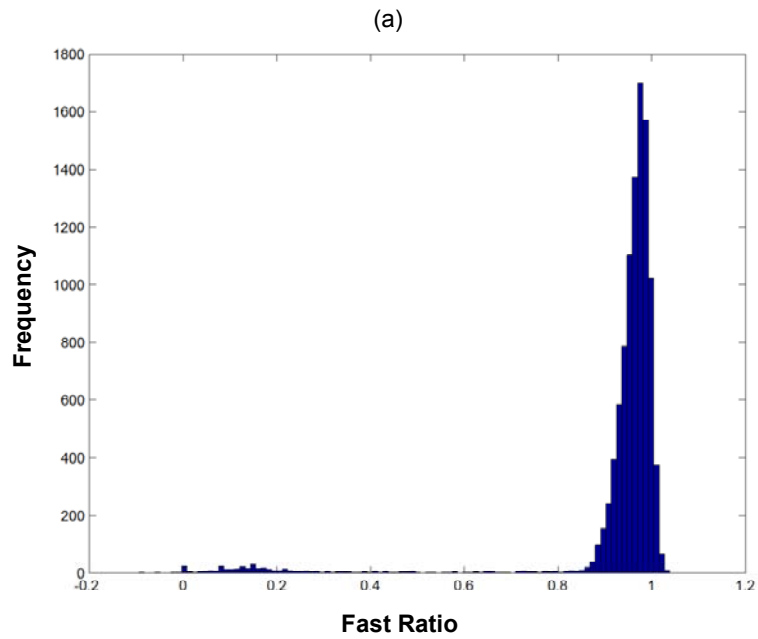


Fig. 4.7: (a) Fast and (b) Slow Ratio distributions from ^{14}C pure beta particle source.

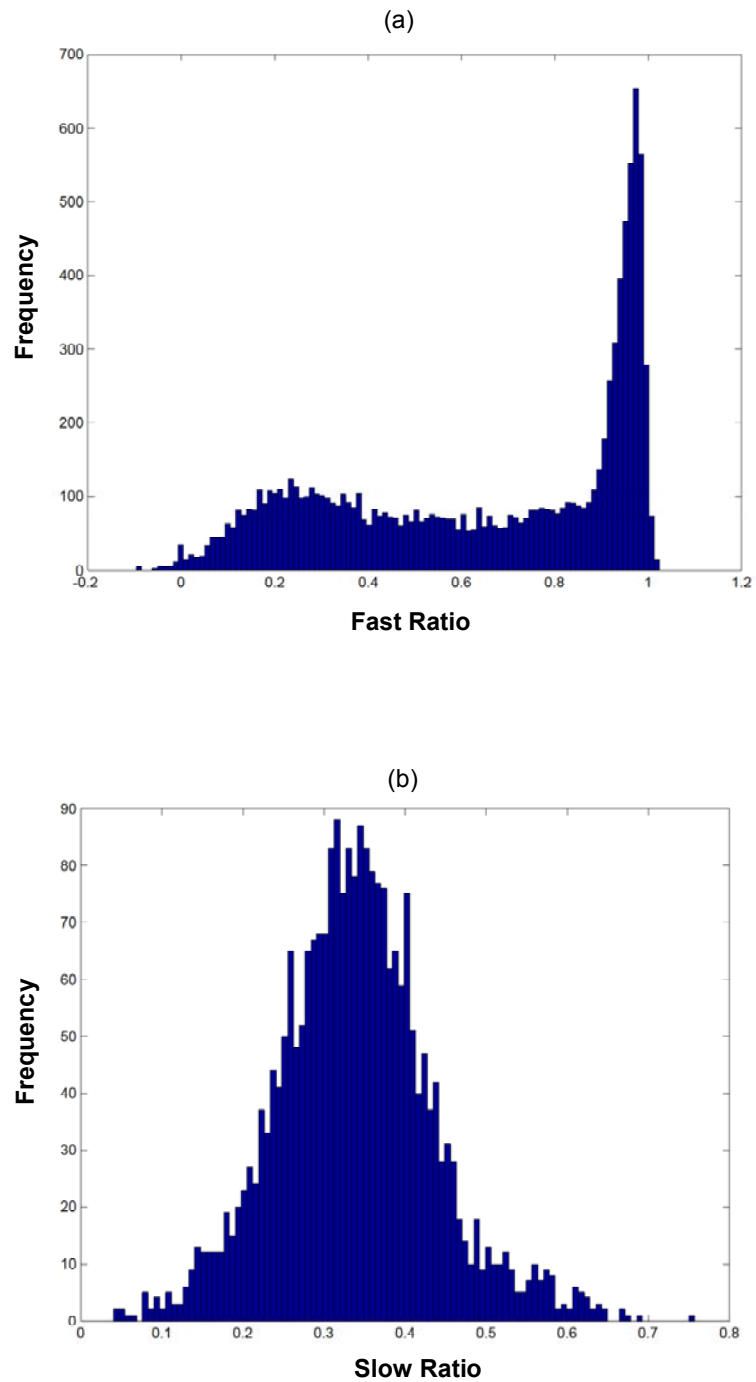


Fig. 4.8: (a) Fast and (b) Slow Ratio distributions from ^{36}Cl pure beta particle source.

The SR distribution measurements, shown above, were performed after FR filtering which follows the MATLAB algorithm of Fig. 3.17.

The FR distributions from the gamma-ray sources (Figs. 4.5 and 4.6) have nearly identical shapes and boundaries. The FR distribution has a very small population at values greater than about 0.4 and, preliminarily, will be selected as the Fast-Ratio threshold, FR_Th. Two peaks can be identified in the FR distributions from the beta emitters (Figs. 4.7 and 4.8). These peaks are attributed to two types of beta-induced pulses; one with a dual-component shape (peak at the left side) which is easily detected using its fast-component signature (events 1 and 2 in Table 3.2), and the other which has one slow component (event 3 from beta particles, 4.6%, in Table 3.2). Pulses with the latter shape, which must be rejected because they are of unknown origin, will be identified in the SR inspection.

Two peaks also can be identified in the SR distributions from gamma-ray sources (Figs. 4.5 and 4.6). The left peak, extending from 0 to about 0.45, is from a single-component and slower pulse (event 3 from gamma-rays, 14.4%, in Table 3.2) and must be rejected for the same reason given above. The right peak (faster) is also a single-component pulse (event 7 from gamma-rays, 12.87%, in Table 3.2) and will be recorded as a gamma pulse.

Based on the evaluation of data in the FR and SR distributions, the FR_Th and SR_Th are set at 0.40 and 0.45, respectively.

4.2.2 Energy Calibration

Prior to any quantitative measurements, the three layers of the phoswich detector must be calibrated for energy deposition from the incident gamma-rays and beta particles. Since two layers of the detector, BC400 and CaF₂:Eu, are intended for beta-particle spectroscopy, these two scintillators must be calibrated separately. For this purpose, the phoswich detector was exposed, on different occasions, to known beta and gamma-ray sources.

The first layer, BC400, was calibrated using two pure beta emitters, ¹⁴C and ⁹⁹Tc (Fig. 4.9). Their energy-spectra end points were used to obtain two points by which a calibration equation can be established. In the following discussion, Y represents the energy deposition in keV and X is the corresponding component summation value (the area under each component of pulse, see Fig. 3.16) in adc units.

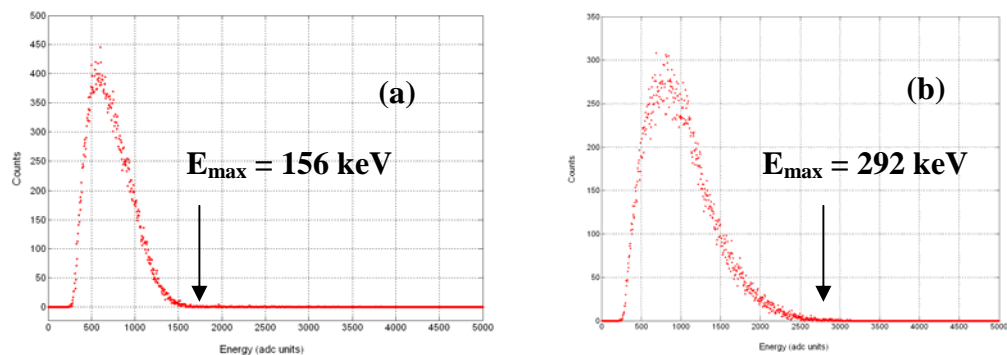


Fig. 4.9: Beta particles (E_{\max}) from (a) ¹⁴C and (b) ⁹⁹Tc were used for BC400 calibration.

During calibration, the FR_Th was set to 0.98 to make sure that the recorded pulses had no slow component. From the spectra in Fig. 4.9, it is determined that,

Y1 = 156 keV, X1 = 1550 adc units and Y2 = 292 keV, X2 = 3000 adc units

Then, assuming linearity between energy deposition and adc units, the calibration equation for BC400 is,

$$E_B \text{ (keV)} = 93.8 * A_B \text{ (adc units/1000)} + 10.6, \quad [4.1]$$

where E_B is the energy deposition in BC400 and A_B is the corresponding pulse area (region A in Fig. 3.16) due to the beta-energy deposition in that layer. The value of A_B can be defined by,

$$A_B = A - (B * Fa), \quad [4.2]$$

where Fa is a correction factor to account for the slow-component contribution in region A of Fig. 3.18. The value of Fa was experimentally measured to be 0.17.

The second layer, CaF₂:Eu, was calibrated using an electron-shielded gamma source, ¹³⁷Cs (Fig. 4.10). The peak-to-Compton ratio is quite small for CaF₂:Eu due to its low Z and relatively small size.

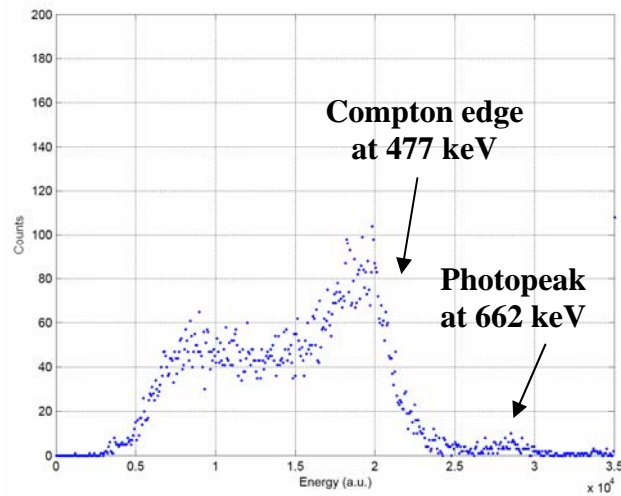


Fig. 4.10: The Compton edge and photopeak of ^{137}Cs were used for $\text{CaF}_2:\text{Eu}$ calibration.

For the energy calibration, both the photopeak and Compton edge were used to obtain the two required data points. During calibration, the FR_Th and SR_Th were set to 0.2 and 0.4 (with condition of $\text{SR} < \text{SR_Th}$), respectively to ensure that the recorded pulses were due to gamma-ray interactions only in the $\text{CaF}_2:\text{Eu}$. From the data in Fig. 4.10:

$Y1 = 477 \text{ keV}$, $X1 = 20500 \text{ adc units}$ and $Y2 = 662 \text{ keV}$, $X2 = 28800 \text{ adc units}$.

Then, the calibration equation for the $\text{CaF}_2:\text{Eu}$ layer is,

$$E_C (\text{keV}) = 22.3 * C_C (\text{adc units}/1000) + 20.0, \quad [4.3]$$

where E_C is the energy deposition in CaF_2 , and C_C is the corresponding pulse area (regions A and B in Fig. 3.18) due to energy deposition in that layer.

The value of C_C can be defined by,

$$C_C = B * F_b, \quad [4.4]$$

where F_b is a correction factor to obtain the whole pulse area from the area in region B. The value of F_b was experimentally measured to be 1.17.

Since the combination of both the BC400 and CaF_2 are intended for beta spectroscopy, the total energy (E_{total}) deposited in these layers is,

$$E_{total} = E_B + E_C. \quad [4.5]$$

The third layer, NaI(Tl) , was calibrated using beta-shielded ^{137}Cs and ^{60}Co gamma-ray sources (Fig. 4.11). For the energy calibration, the 662 keV and 1332 keV photopeaks, respectively from ^{137}Cs and ^{60}Co , were used to obtain the two required points. During calibration, FR_Th and SR_Th were set to 0.35 and 0.45, respectively to make sure that the recorded pulses were due to the gamma-ray interactions only in the NaI(Tl) layer.

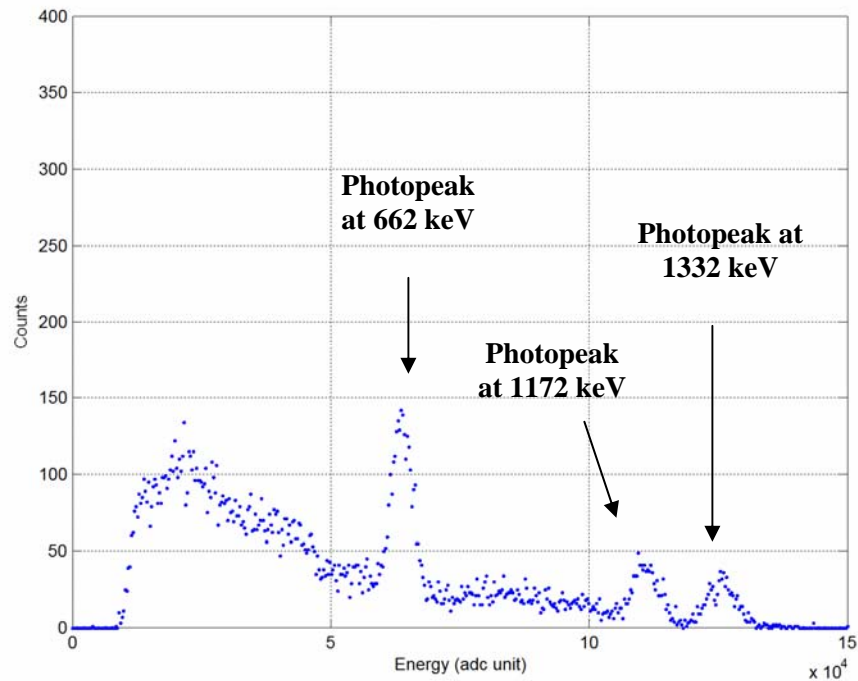


Fig. 4.11: The 662 keV and 1332 keV photopeaks, respectively from ^{137}Cs and ^{60}Co , were used for NaI(Tl) calibration.

From the data in Fig. 4.11,

$Y1 = 662 \text{ keV}$, $X1 = 63,630 \text{ adc units}$ and $Y2 = 1332 \text{ keV}$, $X2 = 125,250 \text{ adc units}$.

Then, the calibration equation for the NaI(Tl) is,

$$E_N (\text{keV}) = 10.87 * C_N (\text{adc units}/1000) - 30.0, \quad [4.6]$$

where E_N is the energy deposition in NaI(Tl) and C_N is the corresponding pulse area (regions A and B in Fig. 3.16) due to energy deposition in that layer. Since the gamma-induced pulses possess only one component, C_N is obtained by,

$$C_N = A + B \quad [4.7]$$

The 1172 keV photopeak of ^{60}Co (the middle peak in Fig. 4.11) was used to evaluate the linearity between energy deposition, E_N , and the pulse area, C_N , given in Eq. 4.6. From the data in Fig. 4.11, $C_N = 110,100$ adc units. And by applying Eq. 4.6, $E_N = 1167$ keV, we can show that a 0.4% deviation from 1172 keV of ^{60}Co exists.

4.2.3 Beta and Gamma-Ray Spectroscopy

To examine the effectiveness of the algorithm at separating beta and gamma events, the detector was exposed to shielded-gamma, pure beta and mixed gamma/beta fields. Using the DPP board (Section 3.2), energy deposition pulses were captured and transferred to the PC. The MATLAB algorithm then processes pulses one-by-one, with a beta and gamma spectral update for every 1000 pulses. During data collection, the percentage of beta and gamma events, and also the percentage of rejected pulses, was recorded.

Figures 4.12 and 4.13 show simultaneous beta and gamma energy spectra, from ^{137}Cs and ^{60}Co (shielded-gamma sources, respectively). Figures 4.14, 4.15 and 4.16 show these spectra, from ^{14}C , ^{99}Tc and $^{90}\text{Sr}/^{90}\text{Y}$ (pure beta emitters, respectively). For comparison, along with the measured spectra, the theoretical energy spectra from the corresponding beta sources are also shown. In Figures 4.17, 4.18 and 4.19, the phoswich detector was exposed, with three configurations, to mixed gamma and beta fields.

For all energy deposition spectra shown, 70,000 - 100,000 radiation pulses were digitally captured and processed. Also during the data collection, the energy histograms contained 1000 energy bins.

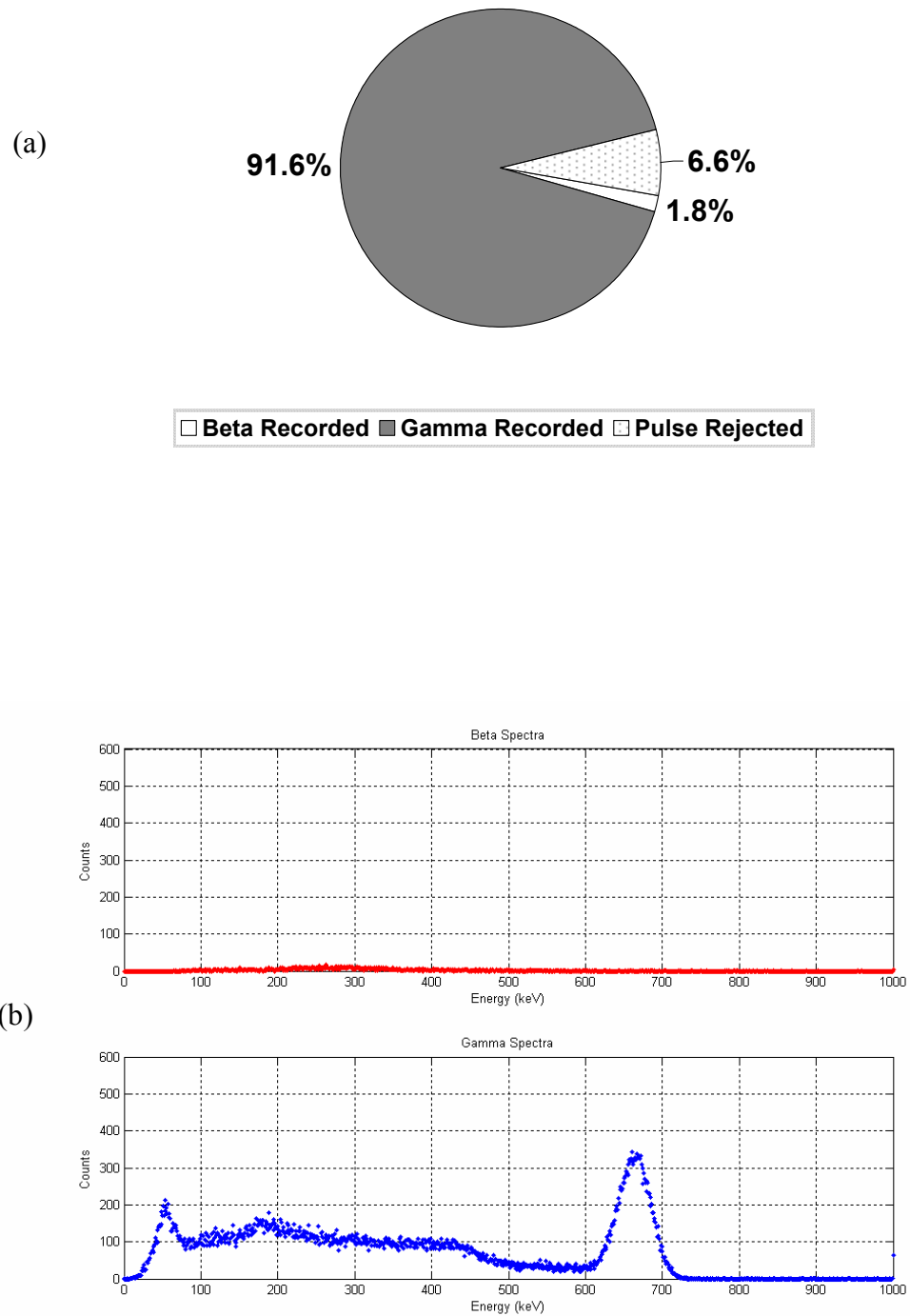


Fig. 4.12: (a) percentage of events and (b) simultaneous beta and gamma-ray energy deposition spectra from shielded ^{137}Cs gamma source.

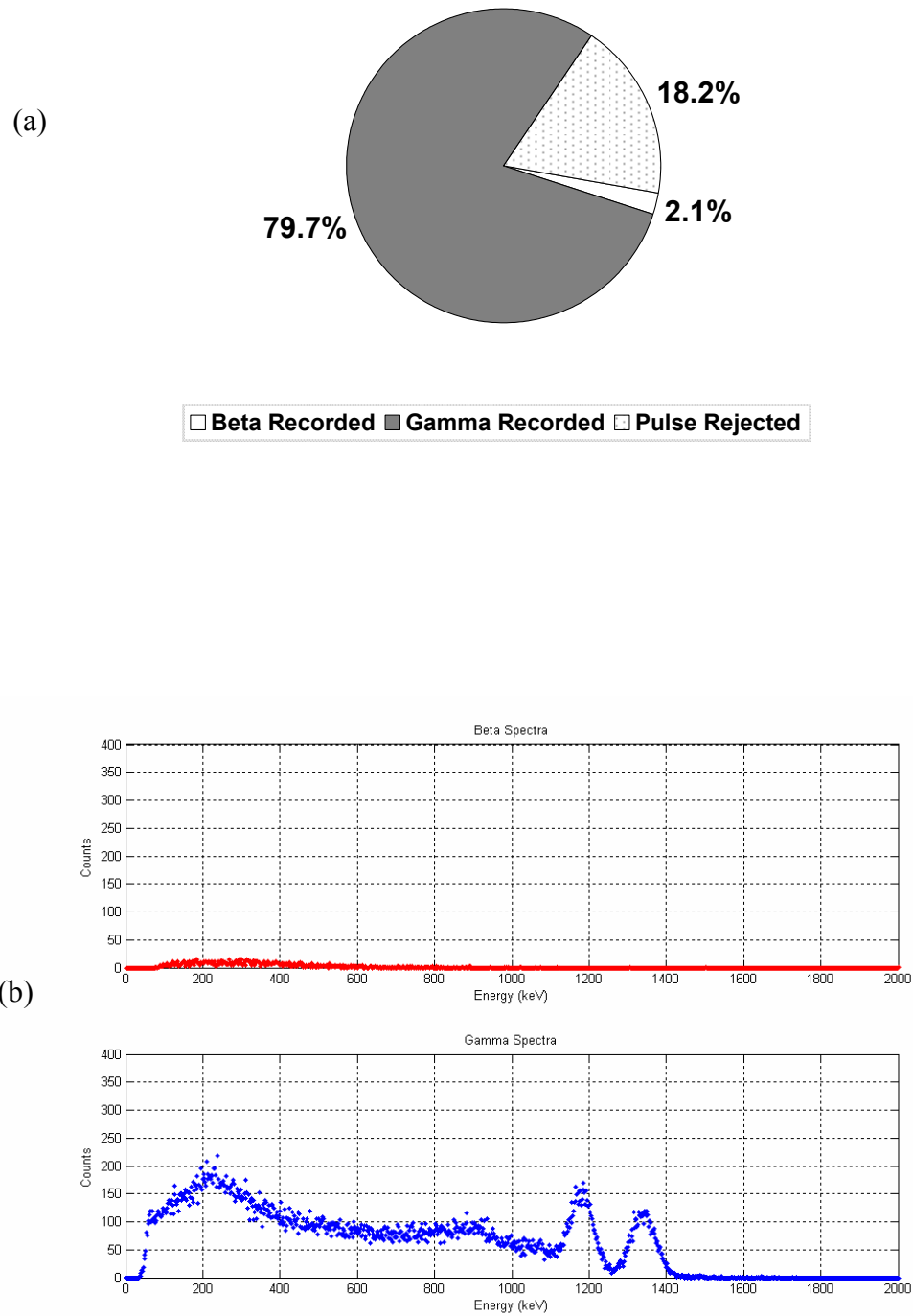


Fig. 4.13: (a) percentage of events and (b) simultaneous beta and gamma-ray energy deposition spectra from shielded ^{60}Co gamma source.

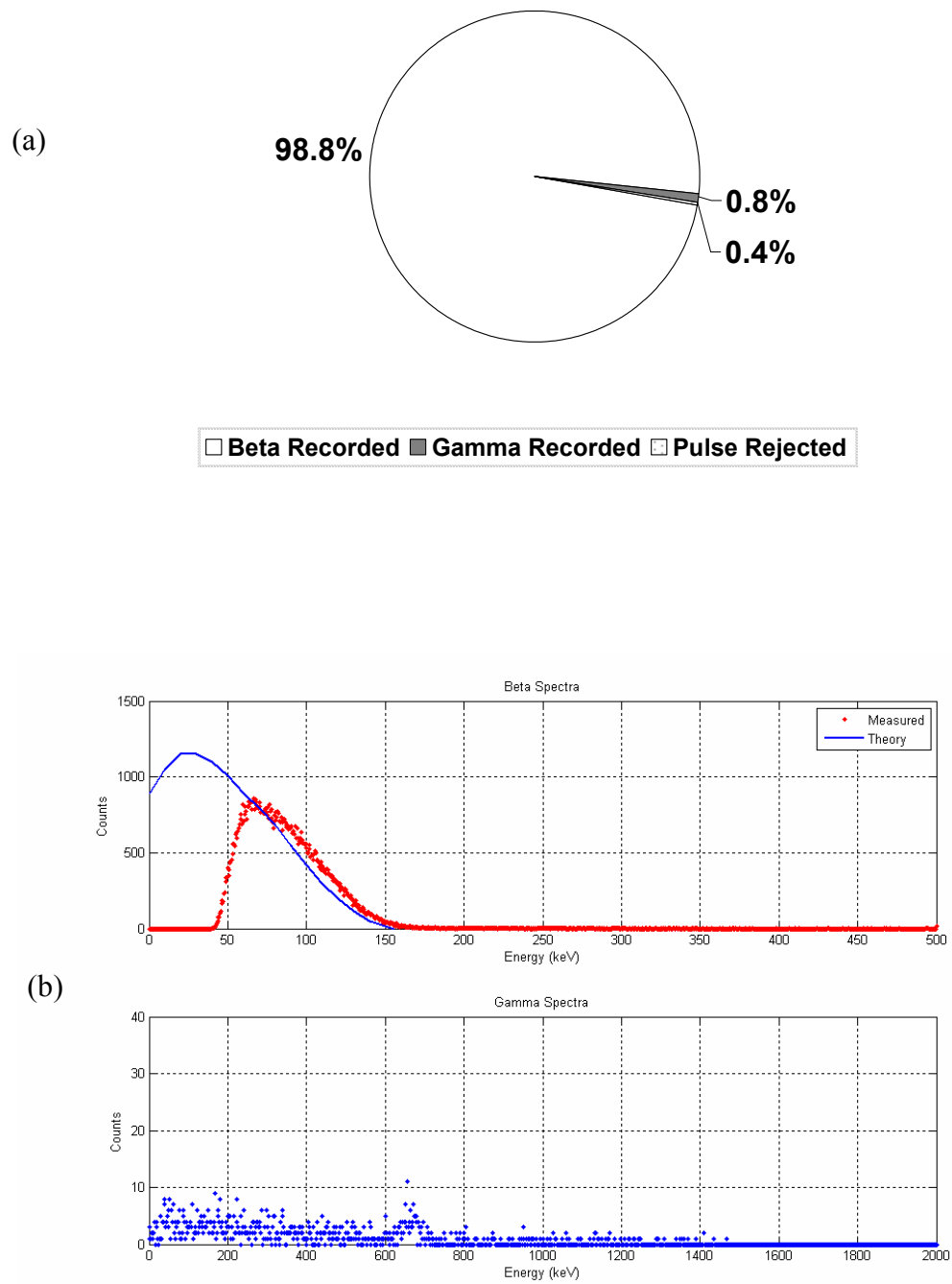


Fig. 4.14: (a) percentage of events and (b) simultaneous beta and gamma-ray energy deposition spectra from ^{14}C , a pure beta emitter.

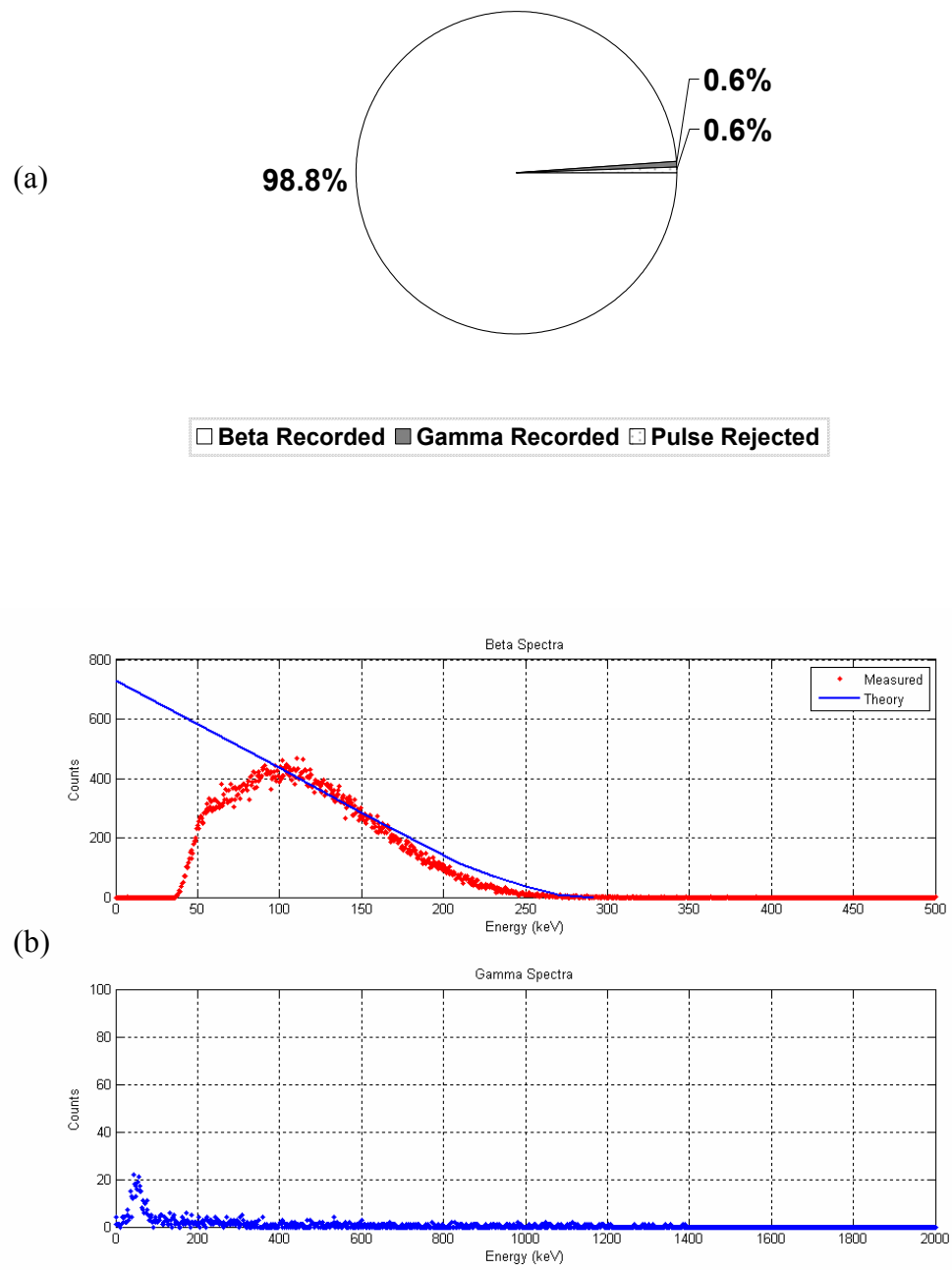


Fig. 4.15: (a) percentage of events and (b) simultaneous beta and gamma-ray energy deposition spectra from ^{99}Tc , a pure beta emitter.

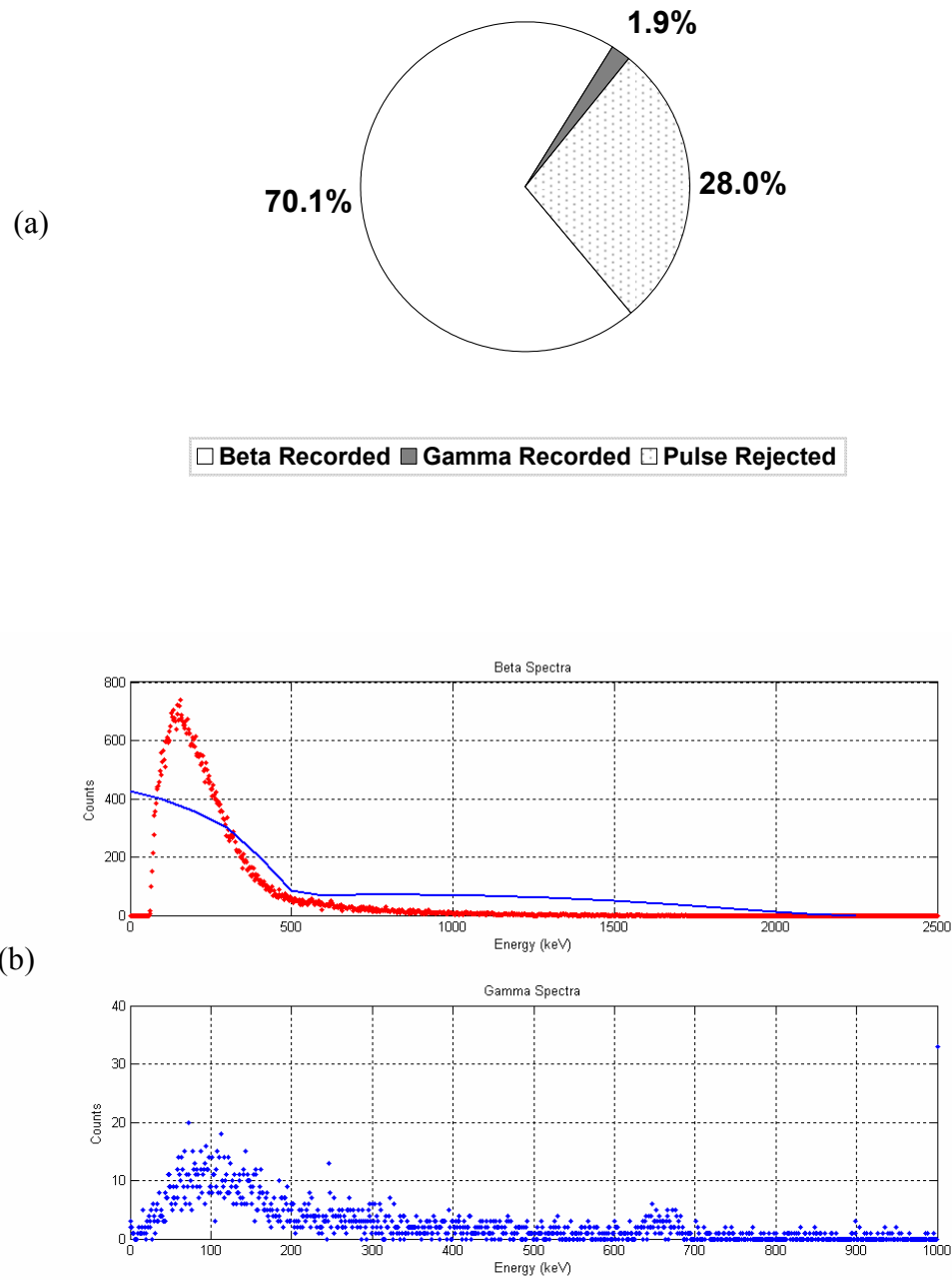


Fig. 4.16: (a) percentage of events and (b) simultaneous beta and gamma-ray energy deposition spectra from $^{90}\text{Sr}/^{90}\text{Y}$, a pure beta emitter.

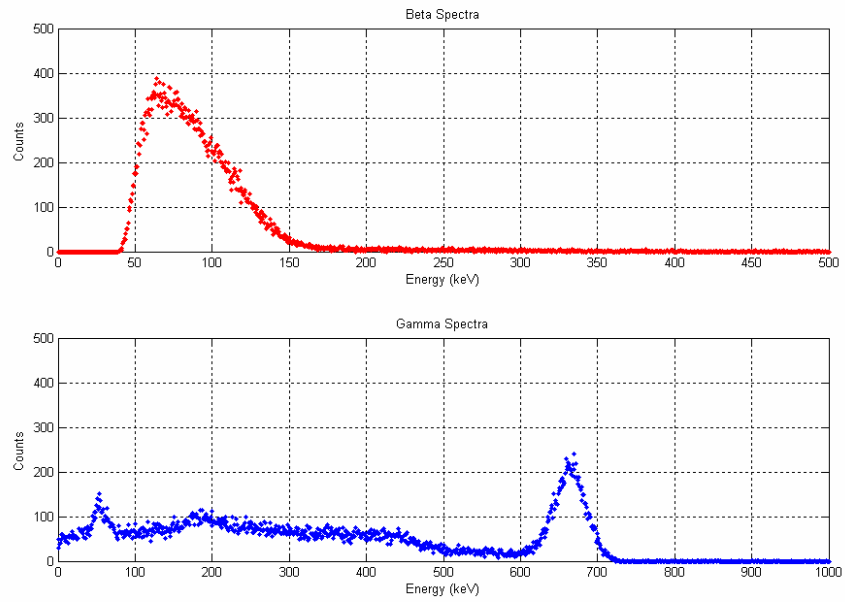


Fig. 4.17: Simultaneous beta and gamma-ray energy deposition spectra from ^{14}C and shielded ^{137}Cs .

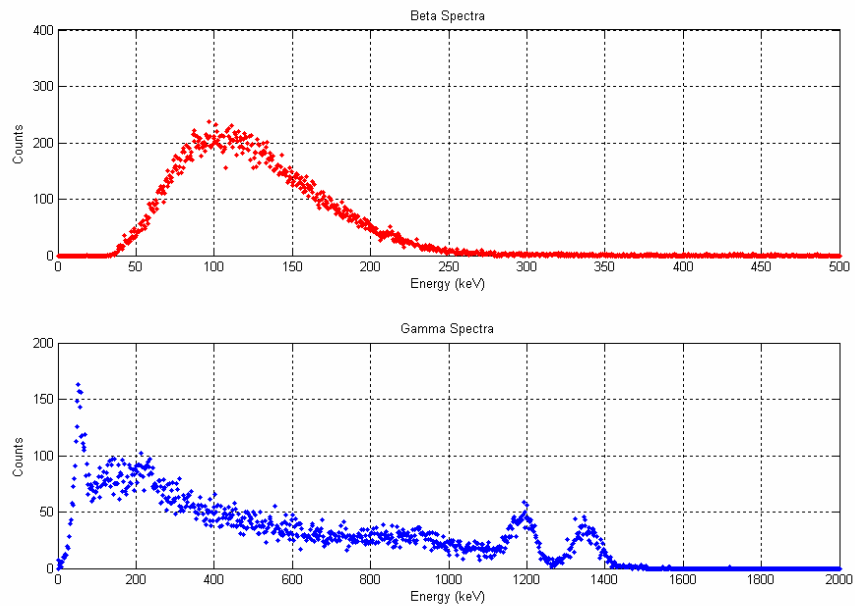


Fig. 4.18: Simultaneous beta and gamma-ray energy deposition spectra from ^{99}Tc and shielded ^{60}Co .

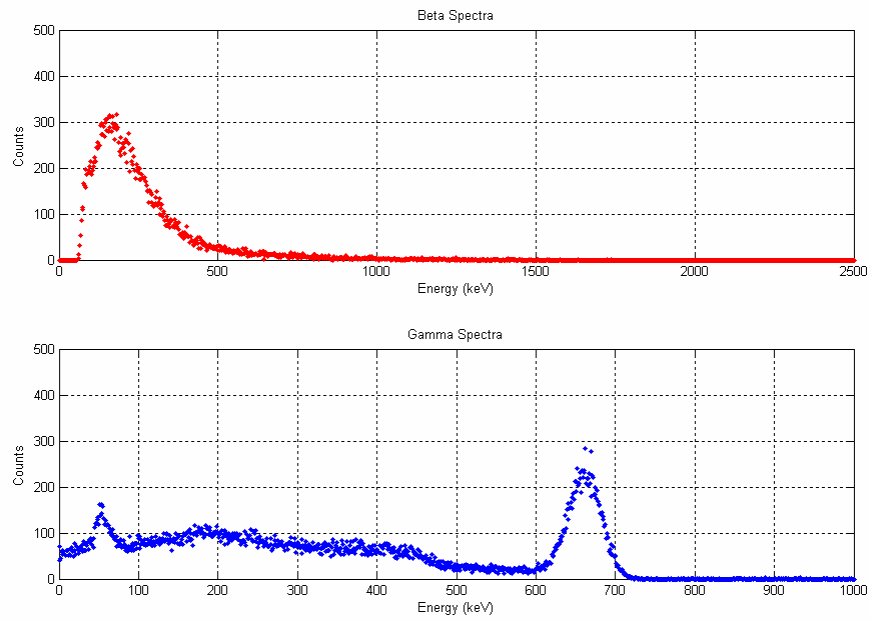


Fig. 4.19: Simultaneous beta and gamma-ray energy deposition spectra from $^{90}\text{Sr}/^{90}\text{Y}$ and shielded ^{137}Cs .

5 Discussion

5.1 Simultaneous Spectroscopy

5.1.1 Gamma Response

All gamma-ray sources were shielded against beta particles or conversion electrons during these measurements. The pie charts of Figs. 4.12 and 4.13 indicate better gamma-ray discrimination from ^{137}Cs than from ^{60}Co . When the detector was exposed to ^{137}Cs , the algorithm identified 91.6% of pulses as gamma interactions and mischaracterized 1.8% of pulses as beta-induced signals. Also, 6.6% of pulses could not be identified and were rejected. As can be seen in the beta spectrum from Fig. 4.12, most of the mischaracterized pulses correspond by energy to Compton events which result in the introduction of pulses in the beta spectrum. This might be due to Compton scattering at the $\text{CaF}_2(\text{Eu})$, but more likely the FR value of those pulses had exceeded the FR threshold (FR_Th) and were identified as beta pulses. The rate of this effect was higher for ^{60}Co (Fig. 4.13), presumably because of many more events at the lower energies (mostly due to backscattering). By comparing Fig. 4.3 with Fig. 4.12, the gamma-ray discrimination capability, using the DPP board, is improved by more than 4%.

Regardless of the beta mischaracterization, the algorithm has been able to efficiently reconstruct the gamma-ray energy spectra from both gamma-ray sources. The Full-Width-at-Half-Maximum (FWHM) for the 662 keV photopeak of

^{137}Cs , shown in Fig. 4.12, was measured to be approximately 6.7%. When the radiation pulses were captured using the digital oscilloscope (Fig. 4.4), the corresponding FWHM was about 8.0%. This enhancement in resolution is due to employing a 12-bit ADC (with 4096 divisions) in the DPP board, while the digital oscilloscope (TEKTRONIX TDS 1002) uses an 8-bit ADC (with 256 divisions).

In both gamma-ray spectra, photopeaks have nearly symmetrical shapes and other spectroscopic features, like the backscattering peak, the Compton continuum and Compton edge, are prominent.

A small peak at the lower energy region of the ^{137}Cs energy spectra was believed to be a characteristic X-ray of the lead shield (~ 70 keV). This was confirmed when the measurement was repeated outside the lead shield. In this measurement, no peak was observed in that energy region. In fact, photoelectric absorption in materials immediately surrounding the detector can lead to the generation of a characteristic X-ray that may reach the detector. For the ^{60}Co spectra, since the lower-level threshold was above this energy, this peak was not recorded.

5.1.2 Beta Response

The quality by which the MATLAB algorithm discriminates beta-induced pulses can be evaluated from Figs. 4.14, 4.15 and 4.16, when the detector is exposed to ^{14}C , ^{99}Tc and $^{90}\text{Sr}/^{90}\text{Y}$ pure beta emitters, respectively. To provide more detail for inspection of the beta energy spectra from ^{14}C and ^{99}Tc , the energy scale

was limited to 500 keV. The algorithm shows better discrimination performance for low-energy beta emitters; ^{14}C ($E_{\text{max}} = 156 \text{ keV}$) and ^{99}Tc ($E_{\text{max}} = 292 \text{ keV}$). For these beta emitters, 98.8% of the pulses were identified as a beta event. Also, the fraction of gamma and rejected pulses were nearly the same. For a high-energy beta emitter such as $^{90}\text{Sr}/^{90}\text{Y}$, however, the percentage of identified beta pulses is lower (70.1%). Referring to Fig. 3.6, the high-energy beta particles most likely deposit less energy in the BC400 and subsequently generate dual-component pulses which have a very small fast component. Therefore, these pulses cannot be detected in the FR inspection, and because of their slow-decaying shape, most of them (in this case 28.0%) are rejected in the SR inspection. In fact, the SR inspection mischaracterizes them as a Compton-induced pulse which may originate from interactions of gamma-rays in the $\text{CaF}_2:\text{Eu}$.

Regarding their end-point energies (E_{max}), the beta spectra show approximately good energy calibration. However, their shapes are not quite matched with the shapes of their theoretical energy emissions. The possible reasons include:

- a) instability in the threshold level due to baseline variations (this mostly effects the low-energy events);
- b) energy deposition in the air between the beta source and detector;
- c) energy deposition in the Mylar;
- d) energy deposition in the gap between BC400 and $\text{CaF}_2:\text{Eu}$; and
- e) partial energy deposition in the scintillation layers.

While reason (a) can be reduced or eliminated by modifying the event logic in the FPGA, degrading of the beta energy-deposition spectra due to other factors, can be reduced by using post-processing methods such as deconvolution. This technique employs radiation transport modeling (e.g. MCNP) to obtain the detector response function for a range of beta energies. Then, using this function, the beta energy spectrum can be deconvolved and enhanced to compensate for energy degradation (Bush-Goddard 2000).

During our measurements, we noticed that the ^{14}C and $^{90}\text{Sr}/^{90}\text{Y}$ beta sources had been contaminated with ^{137}Cs . This was confirmed when these sources were monitored with an HPGe detector. The 662 keV photopeak of ^{137}Cs was dominant in those measurements. In the ^{14}C spectra (Fig. 4.14), although the relative gamma/beta percentage ratio is small ($0.8/98.8 \sim 0.008$), the ^{137}Cs signatures, such as the photopeak (662 keV) and Compton continuum, can be easily identified in the gamma-ray spectra of Fig. 4.14.

5.1.3 Mixed Gamma/Beta Response

To evaluate the system for simultaneous gamma/beta spectroscopy, three gamma/beta source pairs were used to provide mixed gamma/beta radiation fields. The measurement results for pairs $\{^{137}\text{Cs} - ^{14}\text{C}\}$, $\{^{60}\text{Co} - ^{99}\text{Tc}\}$ and $\{^{137}\text{Cs} - ^{90}\text{Sr}/^{90}\text{Y}\}$ are illustrated in Figs. 4.17, 4.18 and 4.19, respectively. Again all gamma-ray sources were shielded against beta particles or conversion electrons

during these measurements. By comparing gamma and beta spectra from the mixed fields with their corresponding spectra from gamma-only and beta-only fields (Figs. 4.12, 4.13, 4.14, 4.15, 4.16 and 4.17), the capability of the signal discrimination process in preserving spectral information from both gamma and beta interactions in our triple-layer phoswich detector is confirmed.

For example, gamma and beta spectra in Fig. 4.17 display the same shapes as when they were collected individually (Figures. 4.12 and 4.14) from ^{137}Cs and ^{14}C .

5.2 Study of Factors Affecting the Results

The factors, which might potentially affect the spectrometer performance, depending on their sources, can be categorized into four main groups. These may originate from the phoswich detector design and configuration, the digital pulse processor, the MATLAB resolving algorithm or from background radiation. Each of the factors will be discussed below.

5.2.1 Phoswich Detector Design and Configuration

In order for the phoswich detector to achieve its best performance during simultaneous reconstruction of separate beta and gamma energy spectra, six main criteria have been considered. These criteria were explained in Chapter 3. Although efforts were taken to reach these criteria, there were still technical and manufacturing issues by which the performance of the system is limited.

One of these issues is that the NaI(Tl) scintillator is required to be completely isolated from other scintillation layers by a thin quartz optical layer (Fig. 3.1). Although the quartz is nearly transparent to light produced in the BC400 and CaF₂(Eu) layers, it has to some extent, a degrading effect on both the energy resolution and the efficiency of the first two scintillation layers. Since the BC400 has a smaller light yield, the performance of this layer is reduced. The coefficients of the energy calibration given in Equations 4.1, 4.3 and 4.6, are inversely proportional to the light yield of the corresponding scintillator. But, because light photons produced in each layer must pass through other materials to reach the photocathode, the relative ratios of these coefficients differ from the inverse ratios of light outputs given in Table 3.1. From Table 3.1 and the energy coefficients in Equations 4.1, 4.3 and 4.6, we have:

$$\frac{\frac{1}{LO_N}}{\frac{1}{LO_C}} = \frac{50}{100} = 0.5 \cong \frac{C_C}{C_N} = \frac{10.87}{22.30} = 0.49 \quad [5.1]$$

$$\frac{\frac{1}{LO_N}}{LO_B} = \frac{26}{100} = 0.26 \neq \frac{C_B}{C_N} = \frac{10.87}{93.8} = 0.12 \quad [5.2]$$

where LO_N , LO_C and LO_B are the relative light output of NaI, $CaF_2(Eu)$ and BC400, respectively, and C_N , C_C and C_B are their corresponding energy coefficients.

For $CaF_2(Eu)$ and NaI(Tl), these ratios are very close, but for BC400 and NaI(Tl), the ratios differ significantly. This shows a significant attenuation for photons produced in BC400 compared with those produced in $CaF_2(Eu)$. It is believed that both the quartz layer and the $CaF_2(Eu)$ are responsible for this attenuation. More measurements and analysis, however, need to be performed to study why the attenuation is different for photons originating in the various layers.

Such a significant light output difference between the scintillation layers employed in the detector extends the dynamic range of the anode pulse. This produces some difficulties to detect pulses from the BC400 since it has the lowest light output per unit energy. This explains why the lower levels of the beta spectra shown in Figs. 4.14, 4.15 and 4.16 are higher than those of the gamma spectra. By adding a firmware control function into the Control module, this may be modified to some extent.

Another issue which is related to the measurement of beta-energy deposition in our phoswich detector is the presence of a very thin gap which exists between the BC400 and $CaF_2(Eu)$ layers. This gap is usually filled with a special optical gel. Although this gel is transparent to the light produced in scintillators, the gel absorbs some of the beta energy without producing any photons. This introduces some error

in estimating the beta energy deposition in the detector for incident beta particles with energies greater than about 100 keV.

5.2.2 Digital Pulse Processor

There are two important sources of error which may originate from the DPP board. One of these sources is the high-frequency noise from the digital circuitry which can easily be picked up by the preamplifier section. For any mixed-signal board, such as our DPP board, to minimize the introduction of high-frequency noise into the analog section, separate power and ground planes are usually assigned for both the analog and digital circuitry. For prototyping purposes, these rules were not considered for building the current DPP board. Instead, to reduce the noise to some extent, the analog section was built on a separate, small daughter board and placed far away from the digital paths and pins. By reducing the noise level in the analog circuitry, more accurate data can be extracted for the low-energy events. This is especially more important for events from the BC400 layer, since it has the smallest light output compared to the other scintillators, and consequently generates pulses with smaller amplitude.

Another potential source of error, which can be reduced in the hardware level, is the pile-up. The fact that pulses from a radiation detector are randomly spaced in time can lead to interfering effects between pulses when count rates are high. This effect is generally called pulse pile-up and involves the superposition of

pulses on the decaying tail from a preceding pulse. For the current DPP board, pile-up is partially rejected by the pulse detection logic in the FPGA Control module. However, pulse pile-up in which the total duration of two or more pulses is less than 10 μ sec may not be identified and therefore mischaracterized as a valid event. These unwanted pulses can be identified and rejected with more sophisticated software inspection tools.

5.2.3 Resolving Algorithm

A resolving algorithm, in the MATLAB environment, has been developed to discriminate gamma- and beta-interaction events in our phoswich detector, and to reconstruct separate gamma and beta energy-deposition spectra in real time (Fig. 3.17). The algorithm performs two inspections to decide whether the captured pulse is a gamma- or beta-induced pulse, or must be rejected because of its unknown conditions (e.g. Compton scattering from incident gamma-rays in the $\text{CaF}_2(\text{Eu})$). These inspections are based on measuring two parameters, the Fast Ratio (FR) and Slow Ratio (SR) of the pulse, by which the general shape of the signal pulse can be determined. Two corresponding thresholds, which have been obtained experimentally, then provide the required criteria for these inspections. Although, optimized threshold levels were chosen (See Figs. 4.5, 4.6, 4.7 and 4.8), some effects can change the FR or SR distributions and increase the radiation mischaracterization percentages.

Consider the experimental results of the FR and SR distributions shown in Figs. 4.5, 4.6, 4.7 and 4.8. Although the anode pulses are generally represented by a simple exponential decay function (Fig. 2.9 and Eq. 2.11), the experimental FR and SR distributions, which are supposed to be proportional to the scintillation decay times, contain relatively wide peaks. This width is increased by increasing the scintillator decay time, and is believed to be due to statistical fluctuations of light pulses over time. For this reason, two overlapping peaks, a relatively thin one and a wider one, appear in the FR distributions from the high-energy (>100 keV) beta events (Fig. 4.8).

Moreover, since the scintillator decay time has a temperature dependency (Knoll 2000), the peaks in the FR and SR distribution consequently may shift or change with temperature. This may degrade the algorithm performance in discriminating beta and gamma events, unless a threshold function is defined to compensate for errors due to temperature change.

Almost all calculations performed in this algorithm are influenced by the performance of the analog circuitry, including the preamplifier and Nyquist filter. The noise level and the frequency bandwidth of these circuits are the most important factors. The radiation discrimination and energy measurement routines are mapped on typical pulse shapes using sample-by-sample calculations. Therefore, any significant changes of the bandwidth may distort or deform the fast component of the anode pulse, resulting in performance reduction when identifying beta-induced pulses and mischaracterizing them as gamma events.

5.2.4 Background Radiation

None of the spectral measurements presented in Chapter 4 was corrected for background radiation. Background correction would involve spectral stripping using a well-characterized background spectrum. This correction must account for live-time differences during which each measurement is performed. Since this function (the live time measurement) was not implemented on the DPP board at the time of measurements, the background correction on the spectral data was not possible.

During measurements, however, our phoswich detector was surrounded by a 2''-thick lead shield to reduce background contributions. Gamma radiation from background had some contribution to the fraction of gamma pulses recorded during pure beta measurements (Figs. 4.14, 4.15 and 4.16).

6 Conclusions

6.1 System Performance

A gamma/beta digital spectrometer has been developed, constructed and tested. The system utilizes a prototype triple-layer phoswich detector, a customized digital pulse processor (DPP) board, and a resolving MATLAB algorithm. The MCNP model was used to simulate the phoswich detector to establish important detector response characteristics to photons and electrons. When exposed to a mixed-gamma/beta field, the detector generates pulses, from which the type of incident radiation and the amount of energy deposited in each layer can be determined.

The measurement results given in Chapter 4 indicate that the spectrometer is capable of separating beta and gamma events with good discrimination. The measurements show that the system has a better discrimination performance for low-energy beta and gamma sources, while for high-energy radiations, relatively more pulses are mischaracterized and rejected. Figures 4.14 and 4.16 demonstrate the power of this system in both separating the gamma/beta events and reconstructing their energy deposition spectra in the phoswich detector. As mentioned in Chapter 4, $^{90}\text{Sr}/^{90}\text{Y}$ and ^{14}C sources, used in our measurements, were contaminated by ^{137}Cs . Even with a very low gamma/beta percentage ratio, 0.8/98.8 \sim 0.008 (see Fig. 4.14), the spectroscopic features of the ^{137}Cs gamma-ray source, such as the photopeak and Compton continuum, are still clearly visible.

The gamma-ray energy resolution at 662 keV of ^{137}Cs was measured to be as low as 6.7%, which shows good agreement with measurements using traditional NaI(Tl) detectors. Measurement of the beta-particle energy resolution, however, was not possible because no suitable conversion electron emitter was available during the measurements. The shapes of beta energy deposition spectra (from common beta-particle emitters), given in this work, were similar to those obtained by Kriss (2004) who used a plastic scintillator and a large-area avalanche photodiode for beta-particle spectroscopy and dosimetry.

The data acquisition system including the DPP board and the MATLAB algorithm, in the absence of any digital processing in MATLAB algorithm, was capable of capturing and transferring 443 signal pulses to the PC (MATLAB) per second. The maximum rate for spectral collection, including data transfer, pulse processing and output display, however, was limited by the MATLAB software and measured to be about 141 signal pulses per second. By using a customized application software, developed using a low-level programming language such as Visual C++, this rate will be increased considerably.

The radiation detection system presented in this work was designed to be a useful general purpose tool for beta/gamma spectroscopy and identification of common radionuclides (beta and gamma-ray sources) in the environment, nuclear sites and laboratories, as well. This requires the detector to accommodate a wide range of beta and gamma-ray energies. For this reason, the design of the phoswich detector was not optimized for any particular radionuclide. It is obvious, however,

that the overall performance of the system can be significantly improved if the detector design is optimized for detecting a specific radionuclide. For example, by decreasing the thickness of the $\text{CaF}_2(\text{Eu})$ layer and increasing the thickness of the BC400 layer, the system performance would be improved if a high-energy beta emitter (e.g. $^{90}\text{Sr}/^{90}\text{Y}$), in the presence of a gamma-ray background, is to be detected. By this optimization, on average, high-energy beta particles release more energy in the BC400 and consequently both the mischaracterizations and pulse rejections due to high-energy beta particles (see Chapter 5) would be decreased significantly.

6.2 Future Work

By identifying and processing events 4 and 6 of Table 3.2, this system can be used as a complete gamma/beta coincidence detection system in which ultra low activities can be detected and measured in the presence of a high-level gamma-ray background. Event 6 of Table 3.2 has three light components. Mathematically, these components can be resolved and quantified using the Least Square Fitting (LSF) method, provided the time-dependent functions of these components are known and stay unchanged during measurement. Although scintillation materials generally possess unique decay times (see Eq. 2.8 and Table 3.1), temperature changes may affect the time profile of the generated light pulses. For example, based on measurements performed using a digital oscilloscope (8-bit, 500 MSPS),

the decay time of $\text{CaF}_2(\text{Eu})$ varied between 680–990 nsec. This issue might be eliminated by using a temperature-weighted function to account for any temperature fluctuations.

As discussed in Section 5.2.2, pulse pile-up can be partially identified and rejected in the existing DPP board. These pulses, however, can be completely identified if they are passed through digital *trapezoidal filters* (Jordanov and Knoll 1994). These digital filters are known as FIR (Finite Impulse Response) filters and can be implemented in the FPGA in real-time. By employing these filters, distortion of beta/gamma energy spectra, due to pulse pile-up at very high-count rates, is significantly reduced.

In the current research, the pulse shape digital processing and reconstruction of beta/gamma energy deposition spectra was performed using a MATLAB algorithm. This algorithm, however, can be translated to a hardware description language (HDL) code. This code can be used to program the FPGA on the DPP board. Once the FPGA is programmed, all digital signal processing calculations would be performed on the DPP board. In this way, the DPP board, with an SRAM memory included, can work in either the waveform or histogram modes.

In the waveform mode, valid radiation pulses would be stored in memory and transferred to the PC as requested. This mode, for purposes of calibration or troubleshooting, can be used to monitor radiation signals.

In the histogram mode, two sections of the memory are assigned for storing the spectra data, one for beta-particles and one for gamma-rays. After signal

processing of valid pulses and determination of energy deposition, one of the energy bins in the corresponding spectra (in memory) is incremented. In this mode, instead of transferring digitized signal pulses, only the histogram data are periodically transferred to the PC, updating the beta/gamma energy spectra on the PC monitor. By adding a Digital Signal Processor (DSP) or a Microcontroller and a small LCD monitor, the DPP board and phoswich detector could be integrated as a stand alone and portable digital beta/gamma spectrometer.

And finally, the prototype demonstrated and presented in this work is hoped to be commercialized in the next few years and, considering its promising measurement results, will find its potential significant applications in areas such as nuclear non-proliferation and medical imaging.

Bibliography

Aleksan, R.; Bouchez, J.; Boussicut, M.; Desanlis, T.; Jourde, D.; Mullie, J.; Pierre, F.; Poinsignon, L.; Praca, R.; Roussel, G.; Thomas, J.F. Pulse shape discrimination with a 100 MHz flash ADC system. *Nuclear Instruments & Methods in Physics Research, Section A: Accelerators, Spectrometers, Detectors and Associated Equipment*. A273: 303-309; 1988.

Al-Haddad, M.N.; Lin, C.; Miller, W.H. Berliner R.R. Development and testing of a flash analog-to-digital based system for pulse shape discrimination of nuclear radiation pulses. *IEEE Transactions on Nuclear Science*. 41(5):1765-1769; 1994.

Aspacher, B.; Rester, A.C. Compton continuum suppression by digital pulse shape analysis. *Nuclear Instruments & Methods in Physics Research, Section A: Accelerators, Spectrometers, Detectors and Associated Equipment*. A338: 516-521; 1994.

Bardelli, L.; Bini, M.; Poggi, G.; Taccetti, N. Application of digital sampling techniques to particle identification in scintillation detectors. *Nuclear Instruments & Methods in Physics Research, Section A: Accelerators, Spectrometers, Detectors and Associated Equipment*. A491: 244-257; 2002.

Bolic, M.; Drndarevic, V. Digital gamma-ray spectroscopy based on FPGA technology. *Nuclear Instruments & Methods in Physics Research, Section A: Accelerators, Spectrometers, Detectors and Associated Equipment*. A482: 761-766; 2002.

Bush-Goddard SP. 2000. Beta spectroscopy using deconvolution and spectral stripping techniques with a triple layer phoswich detector [dissertation]. Ann Arbor (MI): University of Michigan.

Cao, Z.; Miller, L.F. Evaluation of pulse shape discrimination performance of scintillation materials and PSD methods by using statistical models. *Nuclear Instruments & Methods in Physics Research, Section A: Accelerators, Spectrometers, Detectors and Associated Equipment*. A416: 32-44; 1998.

Chandrikamohan, P.; DeVol, T.A. Comparison of pulse shape discrimination methods for phoswich and CsI:Tl detectors. *Proceedings of the Forty-ninth Annual Meeting of the Health Physics Society*. Washington, DC. 2004.

Childress, N.L.; Miller, W.H. MCNP analysis and optimization of a triple crystal phoswich detector. *Nuclear Instruments & Methods in Physics Research, Section A: Accelerators, Spectrometers, Detectors and Associated Equipment*. A490: 263-270; 2002.

Chrien, R.E.; Sutter, R. Noise and pileup suppression by digital signal processing. *Nuclear Instruments & Methods in Physics Research, Section A: Accelerators, Spectrometers, Detectors and Associated Equipment*. 249A: 421-425; 1986.

Cross, W.G.; Freedman, N.O.; Wong, P.Y. Beta ray dose distributions from skin contamination. *Radiation Protection Dosimetry*; Vol. 40, No. 3, 149-168; 1992.

DeVol, T. A.; Tan, H.; Fjeld, R. A. Dual parameter analysis of CsI:TIJPMPT with a digital oscilloscope. *Nuclear Instruments & Methods in Physics Research, Section A: Accelerators, Spectrometers, Detectors and Associated Equipment*. 435A: 433-436; 1999.

Drndarevic, V.; Ryge, P.; Gozani, T. Digital signal processing for high rate gamma-ray spectroscopy. *Nuclear Instruments & Methods in Physics Research, Section A: Accelerators, Spectrometers, Detectors and Associated Equipment*. A277: 532-536; 1989.

Ely, J.H.; Aalseth, C.E.; McIntyre, J.I. Novel beta-gamma coincidence measurements using phoswich detectors. *J. Radioanal. Nucl. Chem.*, 263(1), 245-250; 2005.

Erkkila, B.H.; Wolf, M.A.; Eisen, V.; Unruh, W.P.; Brake, R.J. A beta-gamma discriminator circuit. *IEEE Transactions on Nuclear Science*. 32(1): 969-971; 1985.

Evans, R.D. *The Atomic Nucleus*. New York; McGraw-Hill, 1955.

Farsoni, A.T.; Hamby, D.M. MCNP analysis of a multilayer phoswich detector for beta-particle dosimetry and spectroscopy. *Nuclear Instruments & Methods in Physics Research, Section A: Accelerators, Spectrometers, Detectors and Associated Equipment*. A555: 225-230; 2005.

Fazzi, A.; Varoli, V.A. digital spectrometer for 'optimum' pulse processing. *IEEE Transactions on Nuclear Science*. 45(3): 843-848; 1998.

Frontera, F.; Fiume, D.; Poulsen, J. M.; Taiocchi, G. F.; Basili, A.; Silvestri, S. Pulse shape analyzer for the multiple phoswich detector on the LAPEX experiment.

Nuclear Instruments & Methods in Physics Research, Section A: Accelerators, Spectrometers, Detectors and Associated Equipment. 324A(3):589-597; 1993.

Georgiev, A.; Gast, W.; Lieder, R.M. An analog-to-digital conversion based on a moving window deconvolution. *IEEE Transactions on Nuclear Science.* 41(4): 1116-1124; 1994.

Georgiev, A.; Gast, W. Digital pulse processing in high resolution, high throughput gamma-ray spectroscopy. *IEEE Transactions on Nuclear Science.* 40(4): 770; 1993.

Grzywacz, R. Application of digital pulse processing in nuclear spectroscopy. *Nuclear Instruments & Methods in Physics Research, Section B.* B204: 649-659; 2003.

Hajnal, F.; Measurement of beta spectra and dose in mixed beta-photon field. *Radiation Protection Dosimetry.* Vol. 14 No. 2: 175-178 ;1986.

Hennig, W.; Tan, H.; Warburton, W.K.; McIntyre, J.I. Single channel beta-gamma coincidence detection of radioactive xenon using digital pulse shape analysis of phoswich detector signals. *IEEE Transactions on Nuclear Science.* 53(2): p620; 2006.

Hess, R.; De Antonis, P.; Morton, E. J.; Gilboy, W. B. *Nuclear Instruments & Methods in Physics Research, Section A: Accelerators, Spectrometers, Detectors and Associated Equipment.* 353A: 76-?; 1994.

Hubbard-Nelson, B.; Momayezi, M.; Warburton, W.K. A module for energy and pulse shape data acquisition. *Nuclear Instruments & Methods in Physics Research, Section A: Accelerators, Spectrometers, Detectors and Associated Equipment.* A422: 411-416; 1999.

Hsu, H.H.; Chen, J.; Ing, H.; Clifford, E.T.H.; McLean, T. Skin dose measurement with microspec-2. *Nuclear Instruments & Methods in Physics Research, Section A: Accelerators, Spectrometers, Detectors and Associated Equipment.* A412: 155-160; 1998.

ICRU Report 56. Dosimetry of External Beta Rays for Radiation Protection; 1997.

Jordanov, V.T. Real time digital pulse shaper with variable weighting function. *Nuclear Instruments & Methods in Physics Research, Section A: Accelerators, Spectrometers, Detectors and Associated Equipment.* A505:347-351; 2003.

Jordanov, V.T.; Knoll, G.F. Digital pulse-shape analyzer based on fast sampling of an integrated charge pulse. *IEEE Transactions on Nuclear Science*. 42(4): 683-687; 1995.

Jordanov, V.T.; Knoll, G.F. Digital Synthesis of pulse in real time for high resolution radiation spectroscopy. *Nuclear Instruments & Methods in Physics Research, Section A: Accelerators, Spectrometers, Detectors and Associated Equipment*. A345:337-345; 1994.

Jordanov, V.T.; Knoll, G.F., Huber, A.C.; Pantazis J.A. Digital techniques for real-time pulse shaping in radiation measurements. *Nuclear Instruments & Methods in Physics Research, Section A: Accelerators, Spectrometers, Detectors and Associated Equipment*. A353: 261-264; 1994.

Jordanov, V.T.; Knoll, G.F. Digital pulse processor using a moving average technique. *IEEE Transactions on Nuclear Science*. 40(4): 764-769; 1993.

Knoll, G.F. Radiation Detection and Measurement. 3rd Edition. John Wiley and Sons, Inc. New York. 2000.

Kurahashi, T.; Takahashi, H.; Nakazawa, M. Radiation digital signal processing using smoothing spline. *Nuclear Instruments & Methods in Physics Research, Section A: Accelerators, Spectrometers, Detectors and Associated Equipment*. A422:385-387; 1999.

Langenbrunner, J.L.; Morris, C.L.; Whitton, R.M. CsI-phoswich detector for charged-particle identification. *Nuclear Instruments & Methods in Physics Research, Section A: Accelerators, Spectrometers, Detectors and Associated Equipment*. A316: 450-451; 1992.

Lautridou, P.; Eudes, P.; Germain, M.; Guilbault, F.; Laville, J.L.; Rahmani, A.; Reposeur, T.; Roy, D. Extended pulse shape discrimination capabilities using a CsI-BGO phoswich. *Nuclear Instruments & Methods in Physics Research, Section A: Accelerators, Spectrometers, Detectors and Associated Equipment*. 373(1):135-138; 1996.

Mangun Panitra, M.; Uritani, A.; Kawarabayashi, J.; Iguchi, T.; Sakai, H. Pulse shape analysis on mixed beta particle and gamma-ray source measured by CDZnTe semiconductor detector by means of digital-analog hybrid signal processing method. *J. of Nuclear Science and Technology*, Vol. 38, No. 5: 306-311; 2001.

Mangun Panitra, M.; Uritani, A.; Kawarabayashi, J.; Iguchi, T.; Sakai, H. Improvement of energy spectrum characteristics of CDZnTe semiconductor

detector with a digital-analog fusion method. *Nuclear Instruments & Methods in Physics Research, Section A: Accelerators, Spectrometers, Detectors and Associated Equipment*. A441:483-488; 2000.

Martin, J.E. *Physics for Radiation Protection*. John Wiley and Sons, Inc. New York. 2000.

Martz, D.E.; Rich, B.L.; Johnson, L.O. A portable beta spectrometer for tissue dose measurement. *Radiation Protection Dosimetry*. Vol. 14, No. 2: 183-186; 1986.

Mitra, S.K. *Digital Signal Processing*. 2nd Edition, McGraw-Hill Series in Electrical and Computer Engineering, 2001.

Odell, D.; Bushart, B.S.; Harpring, L.J.; Moore, F.S.; Riley, T.N. Zero dead time spectroscopy without full charge collection. *Nuclear Instruments & Methods in Physics Research, Section A: Accelerators, Spectrometers, Detectors and Associated Equipment*. A422: 363-367; 1999.

Pullia, A. Design-chart aided optimization of digital spectrometers. *IEEE Transactions on Nuclear Science*. 49(4): 1791-1797; 2002.

Ranucci, G. An analytical approach to the evaluation of the pulse shape discrimination properties of scintillators. *Nuclear Instruments & Methods in Physics Research, Section A: Accelerators, Spectrometers, Detectors and Associated Equipment*. A354:389-399; 1995.

Ranucci, G. Time statistics of photoelectron emission process in scintillation counters. *Nuclear Instruments & Methods in Physics Research, Section A: Accelerators, Spectrometers, Detectors and Associated Equipment*. A335:121-128; 1993.

Simoës, J.B.; Correia, C.M.B.A. Pulse processing architectures. *Nuclear Instruments & Methods in Physics Research, Section A: Accelerators, Spectrometers, Detectors and Associated Equipment*. A422:405-410; 1999.

Simoës, J. B.; Simoës, P.C.P.S.; Correia, C.M.B.A. Nuclear spectroscopy pulse height analysis based on digital signal processing techniques. *IEEE Transactions on Nuclear Science*. 42(4): 700-704; 1995.

Simons, G.; Higginbotham, J. Beta-particle spectroscopy with active gamma-ray discrimination. *Nuclear Instruments & Methods in Physics Research, Section A: Accelerators, Spectrometers, Detectors and Associated Equipment*. A293: 551-554; 1990.

Skulski, W.; Momayezi, M. Particle identification in CsI(Tl) using digital pulse shape analysis. *Nuclear Instruments & Methods in Physics Research, Section A: Accelerators, Spectrometers, Detectors and Associated Equipment*. A458:759-771; 2001.

Takada, M.; Shibata, T.; Uwamino, Y.; Nakamura, T. A performance study on a phoswich detector consisting of an inner NE213 scintillator and an outer CaF₂:Eu crystal wall. *Nuclear Instruments & Methods in Physics Research, Section A: Accelerators, Spectrometers, Detectors and Associated Equipment*. A379:293-306; 1996.

Takahashi, H.; Kodama, S.; Kawarabayashi J. A new pulse height analysis based on fast ADC digitizing technique. *IEEE Transactions on Nuclear Science*. 40(4): 626-629; 1993.

Tan, H.; DeVol, T.A.; Fjeld, R.A. Digital alpha/beta pulse shape discrimination of Cs:Tl for on-line measurement of aqueous radioactivity. *IEEE Transactions on Nuclear Science*. 47(4): 1516-1521; 2000.

Usuda, S.; Abe, H. Flow monitor for actinide solutions by simultaneous alpha and beta (gamma) counting using a CsI(Tl) scintillator. *Nuclear Instruments & Methods in Physics Research, Section A: Accelerators, Spectrometers, Detectors and Associated Equipment*. A321:242-246; 1992a.

Usuda, S. Development of ZnS(Ag)/NE102A and ZnS(Ag)/stilbene phoswich detectors for simultaneous alpha and beta (gamma) counting. *Journal of Nuclear Science and Technology*. 29(9):927-929; 1992b.

Usuda, S.; Abe, H.; Mihara, A. Simultaneous counting of alpha , beta and gamma rays with phoswich detectors. *Journal of Alloys and Compounds*. 213:437-439; 1994a.

Usuda, S.; Abe, H.; Mihara, A. Phoswich detectors combining doubly or triply ZnS(Ag), NE102A, BGO and/or NaI(Tl) scintillators for simultaneous counting of alpha, beta and gamma rays. *Nuclear Instruments & Methods in Physics Research, Section A: Accelerators, Spectrometers, Detectors and Associated Equipment* 340A: 540-545; 1994b.

Usuda, S.; Sakurai, S.; Yasuda, K. Phoswich detectors for simultaneous counting of alpha -, beta (gamma)-rays and neutrons. *Nuclear Instruments and Methods in Physics Research, Section A: Accelerators, Spectrometers, Detectors and Associated Equipment*. 388(1-2):193-198; 1997.

Vasil'ev, I.O.; Volodin, A.V. Use of a scintillation spectrometer-dosimeter for separately determining doses under conditions with mixed beta and gamma radiation. *Measurement Techniques*, Vol. 39, No. 7: 778-781; 1996.

Warburton, W. K.; Momayezi, M.; Hubbard-Nelson, B.; Skulski, W. Digital pulse processing: new possibilities in nuclear spectroscopy. Conference on Industrial Radiation and Radioisotope Measurement Applications; IRRMA-1999.

White, T.L.; Miller, W.H. A triple-crystal phoswich detector with digital pulse shape discrimination for alpha/beta/gamma spectroscopy. *Nuclear Instruments & Methods in Physics Research, Section A: Accelerators, Spectrometers, Detectors and Associated Equipment*. A422: 144-147; 1999.

Wissink, L.; Hoefman, M.; Seip, M.; Wilschut, H.W. Particle identification in phoswich detectors by signal width measurement. *Nuclear Instruments & Methods in Physics Research, Section A: Accelerators, Spectrometers, Detectors and Associated Equipment*. 397(2-3): 472-474; 1997.

Zecher, P.D.; Galonsky, A.; Carter, D.E.; Zoltan, S. Neutron/gamma-ray pulse-shape discriminator. *Nuclear Instruments & Methods in Physics Research, Section A: Accelerators, Spectrometers, Detectors and Associated Equipment*. A508: 434-439; 2003.

APPENDICES

APPENDIX A: MCNP INPUT FILE FOR MODELING PHOTO TRANSPORTS

```

1-  C TPL/G1000 KeV
2-  100 1 -2.7 -10 20 40 -72 $Al
3-  200 2 -1.39 -20 40 -50 $ mylar
4-  300 3 -1.032 -20 50 -60 $ L1
5-  400 4 -3.18 -20 60 -70 $ L2
6-  500 5 -2.62 -20 70 -71 $ Quartz
7-  600 6 -3.67 -20 71 -72 $ L3
8-  700 0 10:-40:72 $ Universe
9-
10-  10 cy 2.59    $ Al out
11-  20 cy 2.54    $ Al in
12-  40 py -6.35e-4 $S.M
13-  50 py 0       $ M.L1
14-  60 py 0.0136  $ L1.L2
15-  70 py 0.466   $ L2.Quartz
16-  71 py 2.0904  $ Quartz.L3
17-  72 py 4.6304  $ L3.PMT
18-
19-  Mode p
20-  imp:p 1 1 1 1 1 0
21-  m1 13000 1 $ Al
22-  m2 6000 .4 1000 .4 8000 .2    $ Mylar
23-  m3 6000 0.4754 1000 0.5246    $ BC-400
24-  m4 9000 -0.49 20000 -0.51    $ CaF2
25-  m5 14000 -.4674 8000 -.5326    $ Quartz
26-  m6 11000 0.5 53000 0.5        $ NaI(Tl)
27-  sdef erg=1.0 par=2 pos=0 -6.35e-4 0 sur=40 rad=d1
    dir=d2 vec 0 1 0
28-  si1 2.54
29-  si2 0 1
30-  sp2 -21 0
31-  C Mylar *****
32-  *f18:p 200
33-  f28:p 200
34-  e28 0 0.01 318I 3.2

```

35- C CaF2:Eu *****
36- *f38:p 300
37- f48:p 300
38- e48 0 0.01 318I 3.2
39- C BC-400 *****
40- *f58:p 400
41- f68:p 400
42- e68 0 0.01 318I 3.2
43- C Quartz *****
44- *f78:p 500
45- f88:p 500
46- e88 0 0.01 318I 3.2
47- C NaI(Tl) *****
48- *f98:p 600
49- f108:p 600
50- e108 0 0.01 318I 3.2
51- nps 1000000

APPENDIX B: MATLAB ALGORITHM

```

% MATLAB Algorithm %
% %
% This algorithm controls the DPP1 and collects %
% simultaneous beta and gamma-ray energy spectra. %

clear all
xem = okusbxem3001v2();
xem=openbyserial(xem,"");
configurefpga(xem,'top_2.bit')
setwireinvalue(xem,16,1,1);
updatewireins(xem);
m=100000;
maxg=2000; % energy in keV
maxb=500; % energy in keV
gbin=0:maxg/1000:maxg;
bbin=0:maxb/1000:maxb;
gspec=zeros(1,length(gbin));
bspec=zeros(1,length(bbin));
bc=0;
gc=0;
gbc =0;
bbc=0;
not_valid=0;
subplot(2,1,1)
plot(bbin,bspec,'.r'),xlabel('Energy (keV)'),ylabel('Counts')
title('Beta Spectra')
axis([0 maxb 0 100])
grid on
subplot(2,1,2)
plot(gbin,gspec,'.b'),xlabel('Energy (kev)'),ylabel('Counts')
title('Gamma Spectra')
axis([0 maxg 0 100])
grid on
pause(1)
for n=1:m
    con=mod(n,1000);
    if con==0
        dis=1;
    else
        dis=0;
    end
    end
    updatewireouts(xem);

```

```

while getwireoutvalue(xem,32)==0
    updatewireouts(xem);
end
if(m==n)
    setwireinvalue(xem,16,0,1);
    updatewireins(xem);
end
buf = readfrompipeout(xem,160,2048);
for k=1:1024
    j=k*2;
    data(k)=uint16(buf(j))*256 + uint16(buf(j-1));
end
data=double(data);
base=mean(data(1:90));
[mn,i]=min(data);
if i < 200 & i>90 & (mn > 1)
    fast_ratio(n) = (mean(data(i+5:i+9)) - mean(data(i:i+2)))/(base-mean(data(i:i+2)));
    if fast_ratio(n) > 0.4
        bc =bc+1;
        sum_A=(base*11)-sum(data(i-5:i+5));
        sum_B=(base * 395)-sum(data(i+6:i+400));
        if sum_B >0
            slow_area =sum_B * 1.16;
            fast_area =sum_A - (sum_B * 0.16);
        else
            slow_area=0;
            fast_area= sum_A;
        end
        eb_fast= (93.8*fast_area/1000)+10.6;
        eb_slow= (22.3*slow_area/1000)+20;
        ebc = eb_fast + eb_slow;
        bspec = hist(ebc,bbin) + bspec;
    else
        gbc=gbc+1;
        slow_ratio(gbc)=(mean(data(i+30:i+35))-mean(data(i+5:i+10)))/(base-
mean(data(i+5:i+10)));
        if slow_ratio(gbc) > 0.45
            gc=gc+1;
            eg=(base*411) - sum(data(i-10:i+400));
            egc=(10.87*eg/1000)-30.0;
            gspec = hist(egc,gbin) + gspec;
        else
            bbc =bbc+1;
        end
    end
end
if dis==1
    max_g_spec=max(gspec);
end

```

```

max_b_spec=max(bspec);
if max_g_spec <= 100
    g_y= 100;
else if max_g_spec > 100 & max_g_spec < 500
    g_y =500;
    else if max_g_spec > 500 & max_g_spec < 1000
        g_y =1000;
        else if max_g_spec > 1000 & max_g_spec < 2000
            g_y =2000;
            else if max_g_spec > 2000
                g_y =10000;
            end
        end
    end
end
end
end
if max_b_spec <= 100
    b_y= 100;
else if max_b_spec > 100 & max_b_spec < 500
    b_y =500;
    else if max_b_spec > 500 & max_b_spec < 1000
        b_y =1000;
        else if max_b_spec > 1000 & max_b_spec < 2000
            b_y =2000;
            else if max_b_spec > 2000
                b_y =10000;
            end
        end
    end
end
end
end
subplot(2,1,1)
plot(bbin,bspec,'r'),xlabel('Energy (keV)'),ylabel('Counts')
title('Beta Spectra')
axis([0 maxb 0 b_y])
grid on
subplot(2,1,2)
plot(gbin,gspec,'b'),xlabel('Energy (keV)'),ylabel('Counts')
title('Gamma Spectra')
axis([0 maxg 0 g_y])
grid on
valid=n-not_valid;
fprintf('Pulse Counts: %3.0f\n',n)
fprintf('Valid Pulses: %3.0f,valid),fprintf(' -> %%%4.1f\n',100*valid/n)
fprintf('Beta Counts: %4.0f,bc),fprintf(' -> %%%4.1f\n',100*bc/valid)
fprintf('Gamma Counts: %3.0f,gc),fprintf(' -> %%%4.1f\n',100*gc/valid)
fprintf('Pulse Rej: %3.0f,bbc),fprintf(' -> %%%4.1f\n',100*(bbc)/valid)

```

```
        pause(0.1)
    end
else
    not_valid= not_valid+1;
end
end
```